



Friedrich-Schiller-Universität Jena  
seit 1558



WAGENINGEN UNIVERSITY  
WAGENINGEN UR



Max-Planck-Institut  
für Meteorologie



LSCE



Met Office



Centre de Recherche Public  
Gabriel Lippmann



GAMMA REMOTE SENSING

## Land Cover CCI

# CLIMATE ASSESSMENT REPORT

## 1.0

DOCUMENT REF:	CCI-LC-CARv0
DELIVERABLE REF:	D5.1
VERSION:	1.0
CREATION DATE:	2015-03-02
LAST MODIFIED:	2015-07-13

***This page is intentionally blank.***

	Ref	LC CCI Climate Assessment Report v1		
	Issue	Page	Date	
	1.0	3	13.07.2015	

#### Document Signature Table

	NAME	FUNCTION	COMPANY	SIGNATURE	DATE
PREPARED	Natasha MacBean		LSCE		
PREPARED	Andrew Hartley		MOHC		
PREPARED	Goran Georgievski		MPI-M		
PREPARED	Philippe Peylin		LSCE		
PREPARED	Stefan Hagenman		MPI-M		
PREPARED	Catherine Ottlé		LSCE		
VERIFIED	Pierre Defourny		UCL		
APPROVED					

#### Document Change Record

VERSION	DATE	DESCRIPTION	APPROVED
0.1	2015-03-15	First draft version of the CAR, for PM3	
1.0	2015-07-10	First version of the CAR, for Annual Review	

From version 1.0 to version 1.1

RID	SECTION	COMMENTS

#### Document Diffusion List

ORGANISATION	NAME	QUANTITY
ESA	O. Arino, F. Ramoino	

	Ref	LC CCI Climate Assessment Report v1		
	Issue	Page	Date	
	1.0	4	13.07.2015	

## SYMBOLS AND ACRONYMS

AMIP	: Atmospheric Model Inter-comparison Project
AOD	: Aerosol Optical Depth
ATBD	: Algorithm Theoretical Basis Document
BC	: Brockmann Consult
CCI	: Climate Change Initiative
ECV	: Essential Climate Variables
EOS	: End Of the Season
ESA	: European Space Agency
ESM	: Earth System Model
ET	: Evapotranspiration
fAPAR	: fraction of Absorbed Photosynthetically Active Radiation
GLWD	: Global lake and wetland database
GPP	: Gross Primary Production
HM	: Hydrology Model
K-G	: Köppen-Geiger
ISLSCP	: International Satellite Land Surface Climatology Project
LAI	: Leaf Area Index
LC	: Land Cover
LC_CCI	: Land Cover Climate Change Initiative
LCCS	: Land Cover Classification Scheme
LCU	: Land cover classification uncertainty
LSCE	: Laboratoire des Sciences du Climat et de l'Environnement
LSM	: Land Surface Model
LSP2	: Land surface parameter 2
MAAT	: Wetland ecosystem map
Met UM	: Met Office Unified Model
MISR	: Multi-angle Imaging Spectro-radiometre
MODIS	: Moderate-Resolution Imaging Spectroradiometer
MOHC	: Met Office Hadley Center
MPI-M	: Max Planck Institute for Meteorology

	Ref	LC CCI Climate Assessment Report v1		
	Issue	Page	Date	
	1.0	5	13.07.2015	

MSC	: Mean Seasonal Cycle
NDVI	: Normalized Difference Vegetation Index
NIR	: Near Infrared
NWP	: Numerical Weather Prediction
PFT	: Plant Functional Types
SIND	: Satellite derived inundation
SOS	: Start Of the Season
TBM	: Terrestrial Biosphere Model
UN	: United Nations
WEED	: Wetland Extent Dynamics
WFDEI	: WATCH Forcing Data methodology applied to ERA-Interim data
WB	: Water Body

	Ref	LC CCI Climate Assessment Report v1		
	Issue	Page	Date	
	1.0	6	13.07.2015	

## REFERENCE DOCUMENTS

### *Applicable documents*

ID	TITLE	ISSUE	DATE
AD.1	Statement of Work for ESA Climate Change Initiative Phase II - CCI-PRGM-EOPS-SW-12-0012	1.2	07.06.2013
AD.2	ESA Climate Change Initiative Phase 2 - Land Cover ECV Technical baseline for the project (update of the technical proposal with clarification and negotiation items)	1.0	13.03.2014
AD.3	CCI-LC URD Phase II. Land Cover Climate Change Initiative - User Requirements Document	1.0	28.07.2014
AD.4	CCI-LC PSD Phase II. Land Cover Climate Change Initiative - Product Specification Document	1.0	01.08.2014
AD.5	CCI-LC ATBD Phase II. Land Cover Climate Change Initiative - Algorithm Specification Document	1.0	05.09.2014
AD.6	CCI-LC ATBD Phase I. Land Cover Climate Change Initiative - Climate Assessment Report	1.1	04.07.2014
AD.7	CCI-LC ATBD Phase I. Land Cover Climate Change Initiative - Algorithm Theoretical Basis Document	2.3	28.11.2013

### *Reference documents*

ID	TITLE
RD.1	Bontemps, S., Herold, M., Kooistra, L., van Groenestijn, A., Hartley, A., Arino, O., ... Defourny, P. (2012). Revisiting land cover observation to address the needs of the climate modeling community. <i>Biogeosciences</i> , 9(6), 2145–2157. doi:10.5194/bg-9-2145-2012
RD.2	Brohan, P., Kennedy, J. J., Harris, I., Tett, S. F. B., & Jones, P. D. (2006). Uncertainty estimates in regional and global observed temperature changes: A new data set from 1850. <i>Journal of Geophysical Research: Atmospheres</i> , 111(December 2005), 1–21. doi:10.1029/2005JD006548
RD.3	Clark, D. B., Mercado, L. M., Sitch, S., Jones, C. D., Gedney, N., Best, M. J., ... Cox, P. M. (2011). The Joint UK Land Environment Simulator (JULES), model description – Part 2: Carbon fluxes and vegetation dynamics. <i>Geoscientific Model Development</i> , 4(3), 701–722. doi:10.5194/gmd-4-701-2011
RD.4	Evan, A. T., Flamant, C., Fiedler, S., & Doherty, O. (2014). An analysis of aeolian dust in climate models. <i>Geophysical Research Letters</i> , 41, 5996–6001. doi:10.1002/2014GL060545

	Ref	LC CCI Climate Assessment Report v1		
	Issue	Page	Date	
	1.0	7	13.07.2015	

RD.5	Hewitt, H. T., Copsey, D., Culverwell, I. D., Harris, C. M., Hill, R. S. R., Keen, A. B., ... Hunke, E. C. (2011). Design and implementation of the infrastructure of HadGEM3: the next-generation Met Office climate modelling system. <i>Geoscientific Model Development</i> , 4(2), 223–253. doi:10.5194/gmd-4-223-2011
RD.6	Hicke, J. A. (2005). NCEP and GISS solar radiation data sets available for ecosystem modeling: Description, differences, and impacts on net primary production. <i>Global Biogeochemical Cycles</i> , 19(2), n/a–n/a. doi:10.1029/2004GB002391
RD.7	Le Quéré, C., Raupach, M. R., Canadell, J. G., Marland et al., G., Le Quéré et al., C., Marland, G., ... Woodward, F. I. (2009). Trends in the sources and sinks of carbon dioxide. <i>Nature Geoscience</i> , 2(12), 831–836. doi:10.1038/ngeo689
RD.8	Levy, R. C. (2003). Evaluation of the Moderate-Resolution Imaging Spectroradiometer (MODIS) retrievals of dust aerosol over the ocean during PRIDE. <i>Journal of Geophysical Research</i> , 108(D19), 8594. doi:10.1029/2002JD002460
RD.9	Loveland, T. R., & Belward, A. S. (1997). The IGBP-DIS global 1km land cover data set, DISCover: First results. <i>International Journal of Remote Sensing</i> , 18(15), 3289–3295. doi:10.1080/014311697217099
RD.10	Mahowald, N. M., Kloster, S., Engelstaedter, S., Moore, J. K., Mukhopadhyay, S., McConnell, J. R., ... Zender, C. S. (2010). Observed 20th century desert dust variability: Impact on climate and biogeochemistry. <i>Atmospheric Chemistry and Physics</i> , 10, 10875–10893. doi:10.5194/acp-10-10875-2010
RD.11	Poulter, B., Frank, D. C., Hodson, E. L., & Zimmermann, N. E. (2011). Impacts of land cover and climate data selection on understanding terrestrial carbon dynamics and the CO <sub>2</sub> airborne fraction. <i>Biogeosciences</i> , 8(8), 2027–2036. doi:10.5194/bg-8-2027-2011
RD.12	Poulter, B., MacBean, N., Hartley, A., Khlystova, I., Arino, O., Betts, R., ... Peylin, P. (2015). Plant functional type classification for Earth System Models: results from the European Space Agency's Land Cover Climate Change Initiative. <i>Geoscientific Model Development Discussions</i> , 8(1), 429–462. doi:10.5194/gmdd-8-429-2015
RD.13	Quaife, T., Quegan, S., Disney, M., Lewis, P., Lomas, M., & Woodward, F. I. (2008). Impact of land cover uncertainties on estimates of biospheric carbon fluxes. <i>Global Biogeochemical Cycles</i> , 22(4), n/a–n/a. doi:10.1029/2007GB003097
RD.14	Remer, L. A., Kaufman, Y. J., Tanré, D., Mattoo, S., Chu, D. A., Martins, J. V., ... Holben, B. N. (2005). The MODIS Aerosol Algorithm, Products, and Validation. <i>Journal of the Atmospheric Sciences</i> , 62(4), 947–973. doi:10.1175/JAS3385.1
RD.15	Sitch, S., Huntingford, C., Gedney, N., Levy, P. E., Lomas, M., Piao, S. L., ... Woodward, F. I. (2008). Evaluation of the terrestrial carbon cycle, future plant geography and climate-carbon cycle feedbacks using five Dynamic Global Vegetation Models (DGVMs). <i>Global Change Biology</i> , 14(9), 2015–2039. doi:10.1111/j.1365-2486.2008.01626.x
RD.16	Williams, K. D., Harris, C. M., Bodas-Salcedo, A., Camp, J., Comer, R. E., Copsey, D., ... Xavier, P. K. (2015). The Met Office Global Coupled model 2.0 (GC2) configuration. <i>Geoscientific Model Development Discussions</i> , 8(1), 521–565. doi:10.5194/gmdd-8-521-2015

	Ref	LC CCI Climate Assessment Report v1		
	Issue	Page	Date	
	1.0	8	13.07.2015	

RD.17	Yu, H., Kaufman, Y. J., Chin, M., Feingold, G., Remer, L. A., Anderson, T. L., ... Zhou, M. (2006). A review of measurement-based assessments of the aerosol direct radiative effect and forcing. <i>Atmospheric Chemistry and Physics</i> , 6(3), 613–666. doi:10.5194/acp-6-613-2006
RD.18	Zaehle, S., Sitch, S., Smith, B., & Hatterman, F. (2005). Effects of parameter uncertainties on the modeling of terrestrial biosphere dynamics. <i>Global Biogeochemical Cycles</i> , 19(3), n/a–n/a. doi:10.1029/2004GB002395
RD.19	Jung, M., Reichstein, M., Margolis, H. A., Cescatti, A., Richardson, A. D., Arain, M. A., Arneth, A. LU., Bernhofer, C., Bonal, D., Chen, J. et al. (2011). Global patterns of land-atmosphere fluxes of carbon dioxide, latent heat, and sensible heat derived from eddy covariance, satellite, and meteorological observations, <i>Journal of Geophysical Research - Biogeosciences</i> , 116, G00J07 Available on: <a href="https://lup.lub.lu.se/search/publication/2186879">https://lup.lub.lu.se/search/publication/2186879</a>
RD.20	Hagemann, S.: An improved land surface parameter dataset for global and regional climate models, MPI-Report 336, Max Planck Institute for Meteorology, Hamburg, Germany, 2002
RD.21	Hagemann, S., & Stacke, T. (2014) Impact of the soil hydrology scheme on simulated soil moisture memory. <i>Climate Dynamics</i> , available online. doi:10.1007/s00382-014-2221-6
RD.22	Lehner, B. and Döll, P.: Development and validation of a global database of lakes, reservoirs and wetlands, <i>J. Hydrol.</i> , 296, 1–22, doi:10.1016/j.jhydrol.2004.03.028, 2004.
RD.23	Matthews, E. and Fung, I.: Methane emission from natural wetlands: Global distribution, area, and environmental characteristics of sources, <i>Global Biogeochem. Cy.</i> , 1, 61–86, doi:10.1029/GB001i001p00061, 1987.
RD.24	Peel, M. C., Finlayson, B. L., and McMahon, T. A.: Updated world map of the Köppen-Geiger climate classification, <i>Hydrol. Earth Syst. Sci.</i> , 11, 1633-1644, doi:10.5194/hess-11-1633-2007, 2007.
RD.25	Prigent, C., Matthews, E., Aires, F., and Rossow, W.: Remote sensing of global wetland dynamics with multiple satellite data sets, <i>Geophys. Res. Lett.</i> , 28, 4631–4634, doi:10.1029/2001GL013263 , 2001.
RD.26	Prigent, C., Papa, F., Aires, F., Rossow, W., and Matthews, E.: Global inundation dynamics inferred from multiple satellite observations, 1993–2000, <i>J. Geophys. Res-Atmos.</i> , 112, D12107, doi:10.1029/2006JD007847, 2007
RD.27	Roeckner, E., G. Bäuml, L. Bonaventura, R. Brokopf, M. Esch, M. Giorgetta, S. Hagemann, I. Kirchner, L. Kornblueh, E. Manzini, A. Rhodin, U. Schlese, U. Schulzweida, A. Tompkins (2003): The atmospheric general circulation model ECHAM 5. PART I: Model description. MPI-Report No. 349
RD.28	Stacke, T. and Hagemann, S.: Development and evaluation of a global dynamical wetlands extent scheme, <i>Hydrol. Earth Syst. Sci.</i> , 16, 2915-2933, doi:10.5194/hess-16-2915-2012, 2012.
RD.29	Still, C.J., J.A. Berry, G.J. Collatz, and R.S. DeFries. 2009. ISLSCP II C4 Vegetation Percentage. In Hall, Forrest G., G. Collatz, B. Meeson, S. Los, E. Brown de Colstoun, and D. Landis (eds.). ISLSCP Initiative II Collection. Data set. Available on-line [ <a href="http://daac.ornl.gov/">http://daac.ornl.gov/</a> ] from Oak Ridge National Laboratory Distributed Active Archive Center, Oak Ridge, Tennessee, U.S.A. doi:10.3334/ORNLDAAC/932
RD.30	Weedon, G. P., S. Gomes, P. Viterbo, H. Österle, J. C. Adam, N. Bellouin, O. Boucher, and M. Best, (2010), <i>The WATCH Forcing Data 1958–2001: A meteorological forcing dataset for land surface- and hydrological-models</i> , WATCH Tech. Rep. 22, 41 pp. [Available at <a href="http://www.eu-watch.org/">http://www.eu-watch.org/</a> ]

	Ref	LC CCI Climate Assessment Report v1		
	Issue	Page	Date	
	1.0	9	13.07.2015	

RD.31	Weedon, G. P., G. Balsamo, N. Bellouin, S. Gomes, M. J. Best, and P. Viterbo (2014), The WFDEI meteorological forcing data set: WATCH Forcing Data methodology applied to ERA-Interim reanalysis data, <i>Water Resour. Res.</i> , 50, 7505–7514, doi:10.1002/2014WR015638.
RD.32	Baldocchi, D.D. and K.B. Wilson (2001) Modeling CO <sub>2</sub> and water vapour exchange of a temperate broadleaved forest across hourly to decadal time scales, <i>Ecological Modelling</i> , 142, 155-184.
RD.33	Kucharik, C.J., C.C. Barford, M. El Maayar, S.C. Wofsy, R.K. Monson and D.D. Baldocchi (2006), A multiyear evaluation of a Dynamic Global Vegetation Model at three AmeriFlux forest sites: Vegetation structure, phenology, soil temperature, and CO <sub>2</sub> and H <sub>2</sub> O vapor exchange, <i>Ecological Modelling</i> , 196, 1-31.
RD.34	Lafont, S., Y. Zhao, J.-C. Calvet, P. Peylin, P. Ciais, F. Maignan and M. Weiss (2012) Modelling LAI, surface water and carbon fluxes at high resolution over France: comparison of ISBA-A-gs and ORCHIDEE, <i>Biogeosciences</i> , 9, 439-456.
RD.35	Levis, S. and G.B. Bonan (2004), Simulating Springtime Temperature Patterns in the Community Atmosphere Model Coupled to the Community Land Model Using Prognostic Leaf Area, <i>Journal of Climate</i> , 17, 4531-4540.
RD.36	MacBean, N., F. Maignan, P. Peylin, C. Bacour, F-M. Bréon and P. Ciais (2015) Using satellite data to improve the leaf phenology of a global Terrestrial Biosphere model : impacts on the regional carbon balance. Submitted.
RD.37	Murray-Tortarolo, G., A. Anav, P. Friedlingstein, S. Sitch, S. Piao, Z. Zhu, B. Poulter, S. Zaehle, A. Ahlstrom, M. Lomas, S. Levis, N. Viovy and N. Zeng (2013) Evaluation of Land Surface Models in Reproducing Satellite-Derived LAI over the High-Latitude Northern Hemisphere. Part I: Uncoupled DGVMs, <i>Remote Sensing</i> , 5, 4819-4838.
RD.38	Richardson, A.D., R.S. Anderson, M. Altaf Arain, A.G. Barr, G. Bohrer, G. Chen, J.M. Chen, P. Ciais, K.J. Davis, A. Desai, M.C. Dietze, D. Dragoni, S.R. Garrity, C.M. Gough, R. Grant, D.Y. Hollinger, H.A. Margolis, H. McCaughey, M. Migliavacca, R.K. Monson, W. Munger, B. Poulter, B.M. Raczka, D.M. Ricciuto, A.K. Sahoo, K. Schaefer, H. Tian, R. Vargas, H. Verbeeck, J. Xiao and Y. Xue (2012) Terrestrial biosphere models need better representation of vegetation phenology: results from the North American Carbon Program Site Synthesis, <i>Global Change Biology</i> , doi: 10.1111/j.1365-2486.2011.02562.x
RD.39	Ciais, P., Sabine, C., Bala, G., Bopp, L., Brovkin, V., Canadell, J., Chhabra, A., DeFries, R., Galloway, J., Heimann, M., Jones, C., Le Quéré, C., Myneni, R.B., Piao, S. and Thornton, P.: Carbon and Other Biogeochemical Cycles. In: <i>Climate Change 2013: The Physical Science Basis. Contribution of Working Group I to the Fifth Assessment Report of the Intergovernmental Panel on Climate Change</i> . Cambridge University Press, Cambridge, United Kingdom and New York, NY, USA, 2013.
RD.40	FAO – Food and Agriculture Organization of the United Nations: <i>Global Forest Resources Assessment 2010</i> , FAO, 2010.
RD.41	Hansen, M. C., Potapov, P. V, Moore, R., Hancher, M., Turubanova, S. a, Tyukavina, a, Thau, D., Stehman, S. V, Goetz, S. J., Loveland, T. R., Kommareddy, a, Egorov, a, Chini, L., Justice, C. O. and Townshend, J. R. G.: High-resolution global maps of 21st-century forest cover change, <i>Science</i> , 342(6160), 850–3, doi:10.1126/science.1244693, 2013.

	Ref	LC CCI Climate Assessment Report v1		
	Issue	Page	Date	
	1.0	10	13.07.2015	

RD.42	Li, W., P. Ciais, N. MacBean, S. Peng, P. Defourney, S. Bontemps, Major forest changes and land cover transitions based on plant functional types derived from the ESA CCI Land Cover product, submitted to International Journal of Applied Earth Observation and Geoinformation.
RD.43	Compton, E., & Best, M. J. (2011). Impact of spatial and temporal resolution on modelled terrestrial hydrological cycle components. WATCH Technical Report no.44
RD.44	Kottek, M., J. Grieser, C. Beck, B. Rudolf, and F. Rubel (2006) World Map of the Köppen-Geiger climate classification updated, Meteorologische Zeitschrift, 15, 259-263.
RD.45	Still, C. J., Berry, J. A., Collatz, G. J., and DeFries, R. (2003) Global distribution of C3 and C4 vegetation: Carbon cycle implications, Global Biogeochemical Cycles, 17, doi:10.1029/2001GB001807.
RD.46	Jung, M., Vetter, M., Herold, M., Churkina, G., Reichstein, M., Zaehle, S., Ciais, P., Viovy, N., Bondeau, A., Chen, Y., Trusilova, ., Feser, F. and Heimann, M. (2007). Uncertainties of modeling gross primary productivity over Europe: A systematic study on the effects of using different drivers and terrestrial biosphere models, Global Biogeochemical cycles, vol. 21, GB4021, doi:10.1029/2006GB002915
RD.47	Di Gregorio, A., & Jansen, L. J. M. (2000). Land Cover Classification System (LCCS). Classification Concepts and User Manual. Rome, Italy
RD.48	Giorgi, F. (2006). Climate change hot-spots, Geophysical Research Letters, vol. 33, L08707, doi:10.1029/2006GL025734
RD.49	Ustin, S.L. and Gaman, J.A. (2010). Remote sensing of plant functional types, New Phytologist, vol. 186, 795–816, doi: 10.1111/j.1469-8137.2010.03284.x

	Ref	LC CCI Climate Assessment Report v1		
	Issue	Page	Date	
	1.0	11	13.07.2015	

## TABLE OF CONTENTS

<b>SYMBOLS AND ACRONYMS</b> .....	<b>4</b>
<b>REFERENCE DOCUMENTS</b> .....	<b>6</b>
<b>TABLE OF CONTENTS</b> .....	<b>11</b>
<b>LIST OF FIGURES</b> .....	<b>13</b>
<b>LIST OF TABLES</b> .....	<b>17</b>
<b>1 USING THE LAND COVER CCI PRODUCTS IN MET OFFICE UNIFIED MODEL (MOHC)</b> .....	<b>18</b>
<b>1.1 Introduction</b> .....	<b>18</b>
<b>1.2 Methodology</b> .....	<b>19</b>
<b>1.3 Analysis of Results</b> .....	<b>19</b>
1.3.1 High Resolution NWP hindcast case studies.....	19
1.5m Air Temperature.....	19
Relative humidity .....	24
1.3.2 HadGEM3-AO Results.....	27
Atmospheric Dust .....	32
<b>1.4 Summary</b> .....	<b>38</b>
Global NWP Case Studies .....	38
Global Climate Simulations: HadGEM3-AO.....	38
<b>2 EVALUATING THE LAND COVER AND WATER BODY PRODUCTS IN THE CONTEXT OF CLIMATE MODELING (MPI-M)</b> .....	<b>40</b>
<b>2.1 Summary</b> .....	<b>40</b>
<b>2.2 JSBACH land surface model</b> .....	<b>40</b>
<b>2.3 Water Body evaluation</b> .....	<b>41</b>
2.3.1 Simulations and observations .....	41
2.3.2 Wetland extend comparison .....	42
2.3.3 Conclusions and outlook .....	47
<b>2.4 Revision and update of the cross-walking procedure for JSBACH</b> .....	<b>47</b>
2.4.1 ESA LC_CCI product and lc-user-tool.....	48
2.4.2 JSBACH offline simulations .....	55
2.4.3 Results .....	55
2.4.4 Conclusions and outlook .....	59
<b>2.5 Diversification of albedo into vegetation and soil fraction</b> .....	<b>60</b>
<b>3 USING THE LAND COVER CCI PRODUCTS TO ASSESS PHENOLOGY AND LAND COVER TRANSITIONS (LSCE)</b> .....	<b>61</b>
<b>3.1 Using the NDVI seasonality product to evaluate phenology in the Orchidee Land Surface Model</b> ... 61	
3.1.1 Introduction .....	61
3.1.2 Methods .....	62
3.1.3 Results .....	63

	Ref	LC CCI Climate Assessment Report v1		
	Issue	Page	Date	
	1.0	12	13.07.2015	

Evaluating the optimized phenology in ORCHIDEE.....	63
Evaluating the global distribution of SOS and EOS dates per PFT and per biome.....	65
3.1.4 Discussion and Conclusion.....	68
<b>3.2 Assessing land cover transitions.....</b>	<b>68</b>
3.2.1 Introduction .....	68
3.2.2 Methods .....	69
3.2.3 Results .....	69
3.2.4 Discussion and perspectives .....	71
<b>4 EVALUATION OF THE LC-PFT MAPPING UNCERTAINTY .....</b>	<b>72</b>
<b>4.1 Introduction.....</b>	<b>72</b>
<b>4.2 Methodology .....</b>	<b>73</b>
4.2.1 Land Cover class uncertainty.....	73
4.2.2 Cross-walking uncertainty .....	75
4.2.3 PFT aggregation .....	82
<b>4.3 Results .....</b>	<b>82</b>
4.3.1 PFT maps.....	82
4.3.2 PFT Uncertainty by Giorgi Region.....	85
4.3.3 Latitudinal uncertainty.....	89
<b>4.4 Discussion and Conclusions.....</b>	<b>90</b>
<b>5 APPENDIX – DRAFT PAPER ON UNCERTAINTY ANALYSIS .....</b>	<b>92</b>

	Ref	LC CCI Climate Assessment Report v1		
	Issue	Page	Date	
	1.0	13	13.07.2015	

## LIST OF FIGURES

*Figure 1-1. Summary of the change in the mean error and RMS error of summer time temperature (K) forecasts for northern hemisphere land points (90N to 20N) between 10/06/2011 and 23/08/2012. Red lines denote results from the control simulation using IGBP land cover, and blue lines denote simulations using LC\_CCI 2010 epoch. On all 4 plots, x-axis shows forecast range time, and y-axis shows mean absolute error in comparison to observations (top left), change in mean error (top right), RMS error (bottom left), and change in RMS error (bottom right). Error bars show standard error at 68% confidence level. .... 20*

*Figure 1-2. As above, but for 1.5m air temperature over tropical land (20N to 20S) during northern hemisphere summer..... 21*

*Figure 1-3. Spatial changes in Root Mean Squared (RMS) error for 1.5m air temperature during the northern hemisphere summer (2011-2012) at a forecast lead-time of 48 hours ..... 22*

*Figure 1-4. As above, but for surface air temperature over tropical land areas during the northern hemisphere winter (2010 to 2012) ..... 23*

*Figure 1-5. Change in RMS error of 1.5m air temperature during northern hemisphere winter at a forecast lead time of 48 hours..... 24*

*Figure 1-6. Summary of the change in the mean error and RMS error of northern hemisphere summer time relative humidity (%) forecasts for North America land points (90N to 20N) between 10/06/2011 and 23/08/2012. Red lines denote results from the control simulation using IGBP land cover, and blue lines denote simulations using LC\_CCI 2010 epoch. On all 4 plots, x-axis shows forecast range time, and y-axis shows mean absolute error in comparison to observations (top left), change in mean error (top right), RMS error (bottom left), and change in RMS error (bottom right). Error bars show standard error at 68% confidence level. .... 25*

*Figure 1-7. As above, but for tropical land points only..... 26*

*Figure 1-8. Absolute differences in surface (1000hPa) relative humidity (%) for northern hemisphere summer, at a forecast lead time of 48 hours ..... 27*

*Figure 1-9. Change in March-April-May mean 1.5m air temperature in HadGEM3-AO simulations with LC\_CCI compared to IGBP land cover. Model simulations are compared to HadCRUT3 surface temperature observations for 1979-1998. Panels show (a) spatial distribution of temperature (Kelvin), (b) temperature difference between the two simulations (positive numbers show increases in LC\_CCI w.r.t. IGBP), (c) temperature anomaly for IGBP simulations compared to HadCRUT3, and (d) temperature anomaly for LC\_CCI simulations compared to HadCRUT3. .... 28*

*Figure 1-10. As above, but for temperature at the height of 850mb air pressure compared to ERA-Interim for the period 1989-2008 ..... 29*

*Figure 1-11. Change in simulated monthly Gross Primary Production (GPP) in relation to monthly GPP estimates by [RD.19] for the period 1982-2011. Panels show mean annual GPP estimates from [RD.19] (top left), absolute difference between the IGBP and LC\_CCI simulations (top right), change in root mean square error (RMSE), and fractional change in RMSE (bottom right). .... 30*

	Ref	LC CCI Climate Assessment Report v1		
	Issue	Page	Date	
	1.0	14	13.07.2015	

Figure 1-12. Change in simulated monthly latent heat flux ( $Wm^2$ ) in relation to monthly estimates by [RD.19] for the period 1982-2011. Panels show mean annual latent heat flux estimates from [RD.19] (top left), absolute difference between the IGBP and LC\_CCI simulations (top right), change in root mean square error (RMSE), and fractional change in RMSE (bottom right). ..... 31

Figure 1-13. Change in simulated monthly sensible heat flux ( $Wm^2$ ) in relation to monthly estimates by [RD.19] for the period 1982-2011. Panels show mean annual sensible heat flux estimates from [RD.19] (top left), absolute difference between the IGBP and LC\_CCI simulations (top right), change in root mean square error (RMSE), and fractional change in RMSE (bottom right). ..... 32

Figure 1-14. Bare soil fraction derived from LC\_CCI (top left) and IGBP (top right) land cover maps. Absolute difference ( $IGBP - LC\_CCI$ ) is shown in the bottom left, and fractional difference ( $(IGBP - LC\_CCI)/IGBP$ ) in the bottom right. .... 33

Figure 1-15. Total dust emissions ( $mg/m^2/yr$ ) derived from each land grid cell for simulations using IGBP (antica; top left) and LC\_CCI (dloib; top right). Absolute difference is shown in the bottom left ( $LC\_CCI - IGBP$ ), and fractional difference ( $(IGBP - LC\_CCI)/IGBP$ ) in the bottom right. .... 34

Figure 1-16. Total dust load ( $mg/m^2$ ) in the atmosphere for simulations using IGBP (antica; top left) and LC\_CCI (dloib; top right). Absolute difference is shown in the bottom left ( $LC\_CCI - IGBP$ ), and fractional difference ( $(IGBP - LC\_CCI)/IGBP$ ) in the bottom right. .... 35

Figure 1-17. Comparison of aerosol optical depth (AOD) at 550 nm wavelength derived from MODIS (top left) and MISR (top right) to AOD from IGBP simulations (2<sup>nd</sup> row left) and LC\_CCI simulations (2<sup>nd</sup> row right). Differences between both simulations and MODIS (3<sup>rd</sup> row), and MISR (4<sup>th</sup> row) are also shown. The absence of stippling denotes areas where the total simulated AOD is comprised of more than 50% dust. .... 37

Figure 2-1. Maximum wetlands extend according to various observations and model simulations. .... 43

Figure 2-2. Zonal extend of wetlands from various datasets. .... 44

Figure 2-3. From top to bottom surface temperature, evapotranspiration and runoff. In the middle are absolute values for the reference simulation (REF) without wetlands, and on the left hand side difference WEED-REF, and on the right hand side ESA-REF. .... 45

Figure 2-4. Pond evaporation and pond depth for ESA simulation (top) and difference WEED-ESA (bottom). .... 46

Figure 2-5. Seasonal cycle of evaporation (top) and total runoff compared with GRDC river discharge (bottom), for river basins of Amazon, Niger and Nile. Note that there must be a delay between total runoff and discharge as the former does not include the lateral transport through the river network. .... 46

Figure 2-6. Total area of JSBACH PFTs for various epochs. E2000, E2005 and E2010 are for PFT maps derived from the various ESA-CCI-LC epochs. The others are JSBACH reference maps representing various years in time. .... 52

Figure 2-7. PFT fractions of ESA-CCI-LC map for the 2010 epoch. .... 53

Figure 2-8. PFT fraction differences between ESA-CCI-LC and JSBACH reference map. .... 54

Figure 2-9. Spatial differences between ESA (PFT distributions derived from ESA-CCI-LC) and MPI (default JSBACH PFT distributions) simulations: broadband albedo, surface temperature, evapotranspiration and GPP. 56

	Ref	LC CCI Climate Assessment Report v1		
	Issue	Page	Date	
	1.0	15	13.07.2015	

Figure 2-10. Relative annual mean biases for the major river basins of the world: evapotranspiration (top) and runoff (bottom)..... 57

Figure 2-11. Annual cycle of evapotranspiration for Danube (top) and Congo (bottom) river basins..... 58

Figure 2-12. Albedo seasonal cycle..... 59

Figure 3-1. Plots showing the mean seasonal cycle for the modelled fAPAR (prior = blue; posterior = red) and LC CCI NDVI (grey) for 4 regions (boreal, temperate and tropical northern hemisphere (NH) and the tropical region in the southern hemisphere (SH)). ..... 63

Figure 3-2. Global maps showing the modelled prior and posterior SOS dates (a, b) and their difference (c) compared to those derived from the LC CCI product (d)..... 64

Figure 3-3. Global maps showing the modelled prior and posterior EOS dates (a, b) and their difference (c) compared to those derived from the LC CCI product (d)..... 65

Figure 3-4. Box and whisker plots showing the distributions of SOS (a) and EOS (b) dates per PFT (top panel) and by climate type (bottom panel) for Tropical regions. PFT 2, 3 and 11 are defined as tropical PFTs in the ORCHIDEE TBM. .... 66

Figure 3-5. Box and whisker plots showing the distributions of SOS (a) and EOS (b) dates per PFT (top panel) and by climate type (bottom panel) for Temperate regions. PFT 4 – 6 are defined as temperate forest PFTs in the ORCHIDEE TBM, and PFT 10 is natural C3 grass which is found in temperate and boreal regions. The bottom panel shows the distribution for both temperate warm and cold regions as defined by the K-G classification and following [RD.11]. ..... 67

Figure 3-6. Box and whisker plots showing the distributions of SOS (a) and EOS (b) dates per PFT (top panel) and by climate type (bottom panel) for Boreal regions. PFT 7 – 9 are defined as boreal forest PFTs in the ORCHIDEE TBM, and PFT 10 is natural C3 grass which is found in temperate and boreal regions. The bottom panel shows the distribution for both boreal warm and cold regions as defined by the K-G classification and following Poulter et al. (2011). ..... 67

Figure 3-7. The net forest loss from 2000 to 2010 in the estimates of ESA (left) and the net forest loss from 2000 to 2012 in the estimates of Hansen et al. (2013) (right)..... 70

Figure 3-8. The global transition matrix (left), the global composition patterns of all transitions (middle), and the global composition patterns of crop gain (right) during 2000-2005 and during 2005-2010. In the matrix, the row names represent the sources of transitions, and the column names represent the gains. The colour represents the global area of each transition..... 70

Figure 4-1. Maps showing a) the fraction of vegetation for the Trees (1<sup>st</sup> row), Shrubs (2<sup>nd</sup> row), Natural and Managed Grasses (3<sup>rd</sup> row) and Bare soil (4<sup>th</sup> row), and b) the difference between each case and the reference for each of the uncertainty simulations. The reference case is shown in the middle column (refLC refCW), the minimum biomass vegetation distribution maps are shown to the left of the reference case, first with minimum LC maps and the reference cross-walking table (minLC refCW – 2<sup>nd</sup> column) and with both the minimum biomass LC maps and minimum cross-walking table (minLC minCW – 1<sup>st</sup> column). To the right of the reference map are the equivalent maximum biomass vegetation distributions (maxLC refCW – 4<sup>th</sup> column, maxLC maxCW – 5<sup>th</sup> column). ..... 83

	Ref	LC CCI Climate Assessment Report v1		
	Issue	Page	Date	
	1.0	16	13.07.2015	

*Figure 4-2. Giorgi Regions used for summarising vegetation fractions, overlaid onto tree fractional cover from the reference land cover map. Red boundaries indicate the continent boundaries used in Figure 4-3 and the surrounding grey histograms show longitudinal (top), and latitudinal (right) mean fractions..... 85*

*Figure 4-3. Mean fractional cover for each Giorgi Region, separated by continent. Values shown by the coloured bars represent the spatial mean for each cover type in the reference land cover map. Error bars show the minimum and maximum values for each bar from the uncertainty estimates..... 87*

*Figure 4-4. Impact of uncertainty on the balance between different vegetation types at the continental (and global) scale. Each point shows the average fraction of one cover type compared to another, over a given continent (or the whole world) for a given type of uncertainty. Labels at the top of each scatterplot indicate the cover types shown in the x axis (first label), and the y axis (second label). ..... 88*

*Figure 4-5. Zonal distribution of area covered by the bare soil and major vegetation types (tree, shrub and grass) according to 5 different combinations of LC maps and cross-walking procedure ..... 90*

	Ref	LC CCI Climate Assessment Report v1		
	Issue	Page	Date	
	1.0	17	13.07.2015	

## LIST OF TABLES

<i>Table 2-1. Status of the development and implementation of WEED scheme into JSBACH .....</i>	<i>42</i>
<i>Table 2-2. Cross walking table for converting ESA-CCI-LC classes into JSBACH PFTs.....</i>	<i>50</i>
<i>Table 2-3. PFT types used in JSBACH. Tile column indicates types used in this study and their distribution, while ID column indicate so far implemented types into JSBACH. ....</i>	<i>51</i>
<i>Table 4-1. Each land cover class within the Land Cover CCI legend is assigned a class within a biomass hierarchy for use in assessing classification uncertainty. The highest biomass is tree, followed by shrub, grass, moss and lichen and then bare .....</i>	<i>74</i>
<i>Table 4-2. Perturbations of the cross walking table from [RD.12].....</i>	<i>77</i>
<i>Table 4-3. Aggregation of PFTs for analysis .....</i>	<i>82</i>
<i>Table 4-4. Description of Giorgi regions as shown in Figure 4-2.....</i>	<i>86</i>
<i>Table 5-1. Each land cover class within the Land Cover CCI legend is assigned a class within a biomass hierarchy for use in assessing classification uncertainty. The highest biomass is tree, followed by shrub, grass, moss and lichen and then bare .....</i>	<i>98</i>
<i>Table 5-2. Perturbations of the cross walking table from Poulter et al (2015).....</i>	<i>100</i>
<i>Table 5-3. Aggregation of PFTs for analysis .....</i>	<i>105</i>

	Ref	LC CCI Climate Assessment Report v1		
	Issue	Page	Date	
	1.0	18	13.07.2015	

# 1 USING THE LAND COVER CCI PRODUCTS IN MET OFFICE UNIFIED MODEL (*MOHC*)

## 1.1 Introduction

In the Earth system, vegetation plays an important role in the exchange of carbon, heat, moisture and momentum between the land surface and the atmosphere. In land surface models (LSMs), that form part of larger Earth System Models (ESMs), the vegetated land surface is simplified into plant functional types (PFTs), which describe how groups of plants with similar physiology interact with the atmospheric boundary layer and soil. The distribution of these PFTs is defined using land cover maps that are spatially aggregated, and thematically translated into fractions of PFTs according to a cross-walking table approach [RD.12]. The interaction between a PFT and the atmosphere is simulated by a series of equations that describe how plants exchange carbon, heat, moisture and momentum with the atmosphere. Exchanges of CO<sub>2</sub> between the PFT and the atmosphere, are controlled for example via equations for photosynthesis and autotrophic respiration (e.g. [RD.7]), which are limited according to availability of light and rubisco, and rate of transport of photosynthetic products (C3 photosynthesis), or PEPCarboxylase (C4 photosynthesis). Exchanges of heat, moisture and momentum between the land surface and the atmosphere are also affected by PFT, according to the rate of photosynthesis, the leaf level stomatal conductance of moisture, the amount of radiation intercepted by the vegetation canopy, and the roughness of the surface.

Assessment of the uncertainties in simulating these interactions has so far been focused on land surface model structural uncertainty [RD.15], parameter based uncertainty [RD.8], and uncertainty in meteorological driving data for the land surface models [RD.6, RD.11]. Despite the increasing diversity of land cover maps, little work has been published on how to improve the predictive skill of weather or climate models by reducing the uncertainty in global land cover maps. [RD.13] showed that over the UK, uncertainty in global land cover maps affects land carbon fluxes in land surface models. In comparison to a land surface model driven by a high spatial resolution (25m) land cover dataset, differences in Gross Primary Production (GPP) of between -15.8% to 8.8% were found when different global land cover maps were used. Furthermore, [RD.11] show that the error due to land cover and meteorological driving data is 3.1 PgC yr<sup>-1</sup>, which is larger than the 1.5±0.7 PgC yr<sup>-1</sup> net emissions from land use change for the period 1990-2005 reported by [RD.7].

The Met Office Unified Model (Met UM) is a scale-able model that can be formulated to run over a range of different spatial and temporal scales. It can be used at short time scales and high spatial resolutions for Numerical Weather Prediction (NWP), medium range time scales for seasonal forecasting, and over much longer time scales for climate change projections. To date, the Met UM has used land cover information from the IGBP DISCover dataset [RD.9] for global and regional scale forecasts and climate projections. Land cover information is converted via a cross-walking matrix to a fractional coverage of 9 land surface tiles. Of these tiles, 5 represent the spatial coverage

	Ref	LC CCI Climate Assessment Report v1		
	Issue	Page	Date	
	1.0	19	13.07.2015	

of plant functional types: Broadleaf tree, needleleaf tree, shrub, C3 grass and C4 grass. These 5 vegetation tiles determine how the vegetated land surface interacts with the boundary layer of the atmosphere.

This report presents results from further tests by the Met Office Hadley Centre on the impact of using the Land Cover CCI (LC\_CCI) products in the Met UM. These simulations are standardised tests that are part of the procedure for assessing improvements to the MetUM at both NWP time scales and Climate time scales. The LC\_CCI datasets have been shown to precisely describe land cover classes [RD.1], thus allowing for a more precise cross-walking conversion from land cover to PFTs [RD.12]. However, before the LC\_CCI data can be adopted in Met Office operational models, these tests need to be conducted to show that the changes have improved model performance. This report presents the results of some of those tests for the following experiments:

1. Global NWP forecast model at n768 resolution
2. Global climate simulations at n96 resolution (HadGEM3-AO)

## 1.2 Methodology

Here, we use an Atmospheric Model Inter-comparison Project (AMIP) setup of the Hadley Centre model HadGEM3-A [RD.5] and a high resolution global forecast model to demonstrate the impacts of the LC\_CCI revised land cover ontology in a coupled atmosphere-ocean model. Both model setups involved using observed sea surface temperatures and observed climate forcings (greenhouse gas concentrations, aerosols and sea ice) were used to simulate the historical climate.

For HadGEM3-AO, simulations were run for a 20-year period from 1990 to 2009 at a spatial resolution of 1.875 x 2.5 degrees (n96 resolution). A control simulation was run with the default model setup, including PFTs derived from the IGBP DISCover land cover map for 1992-1993 [RD.9]. The LC\_CCI epoch 2010 was used to represent the distribution of plant functional types, as previously discussed in the Land Cover CCI Phase 1 Climate Assessment Report [AD.6]. The LC\_CCI classes were converted to PFT distributions [RD.12], and used instead of IGBP DISCover in a separate simulation to investigate the impact of improvements in land cover.

For the high resolution global forecast model [RD.16], observed climate forcings were assimilated into operational NWP global hindcasts to run case study examples for the Northern Hemisphere winter of 2010 and 2012, and summer of 2011 and 2012.

## 1.3 Analysis of Results

### 1.3.1 High Resolution NWP hindcast case studies

#### *1.5m Air Temperature*

For 1.5m air temperature, small reductions in mean bias were found for northern hemisphere land temperature of 0.1 degrees kelvin, relative to observations (Figure 1-1), averaged over the whole land

area. This was the case for forecast lead times of 24 to 132 hours. The plots in Figure 1-1 show an improvement in both the mean error (top row) and RMS error (bottom row) at a range of forecast lead times. Using the LC\_CCI to define fractional cover types resulted in a reduction of mean bias in northern hemisphere surface air temperature of between 0.05 and 0.1 Kelvin, compared to observations, for forecast lead times of 72 to 132 hours.

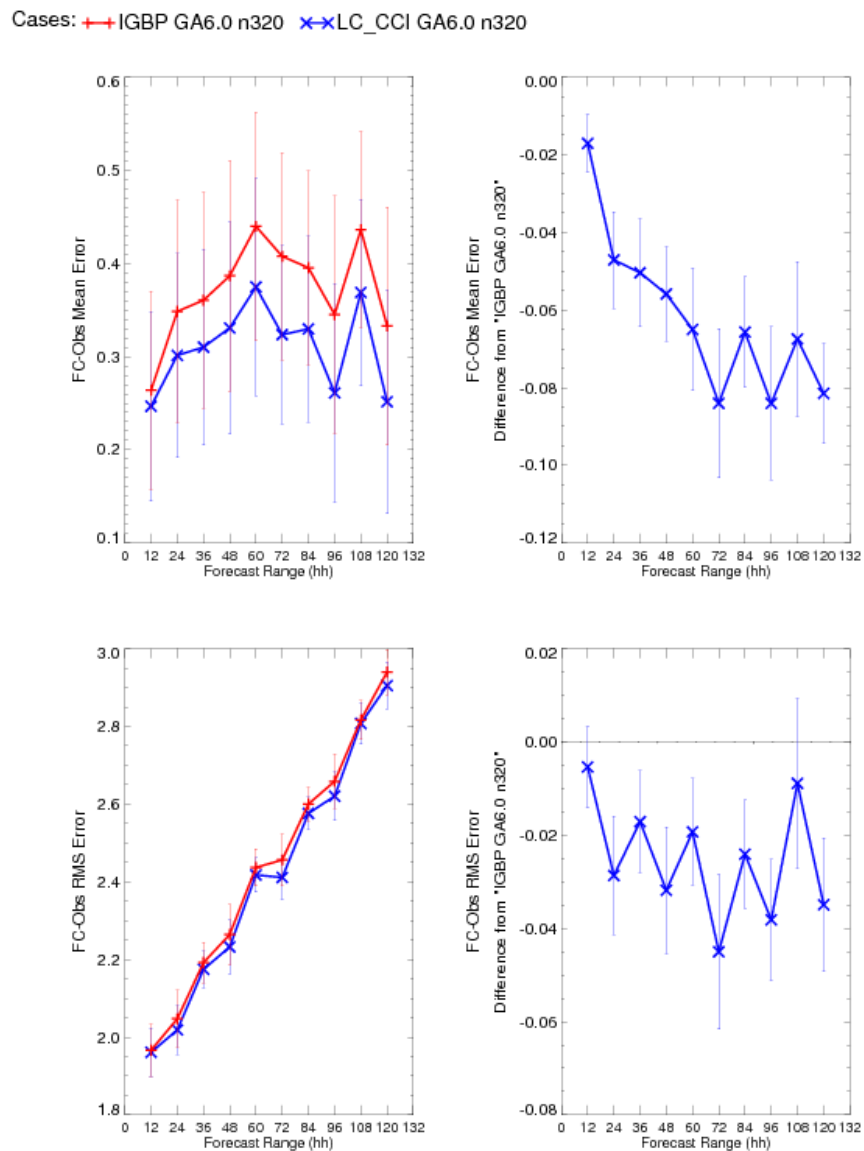


Figure 1-1. Summary of the change in the mean error and RMS error of summer time temperature (K) forecasts for northern hemisphere land points (90N to 20N) between 10/06/2011 and 23/08/2012. Red lines denote results from the control simulation using IGBP land cover, and blue lines denote simulations using LC\_CCI 2010 epoch. On all 4 plots, x-axis shows forecast range time, and y-axis shows mean absolute error in comparison to observations (top left), change in mean error (top right), RMS error (bottom left), and change in RMS error (bottom right). Error bars show standard error at 68% confidence level.

Larger improvements were found for tropical land areas (20S to 20N) during the northern hemisphere summer (Figure 1-2). Here, reductions in mean bias of 0.12 to 0.18 Kelvin were found at forecast lead times ranging from 24 to 132 hours.

Cases: + IGBP GA6.0 n320 x LC\_CCI GA6.0 n320

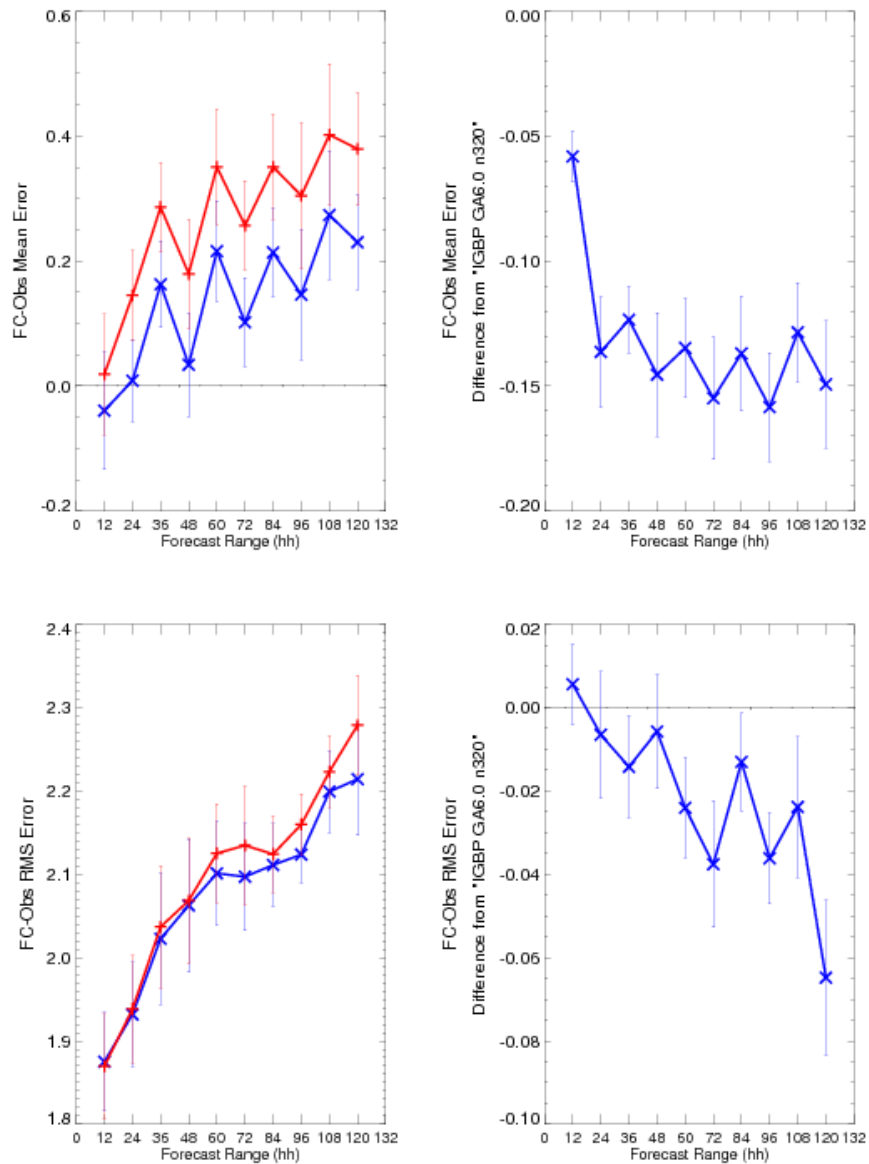


Figure 1-2. As above, but for 1.5m air temperature over tropical land (20N to 20S) during northern hemisphere summer

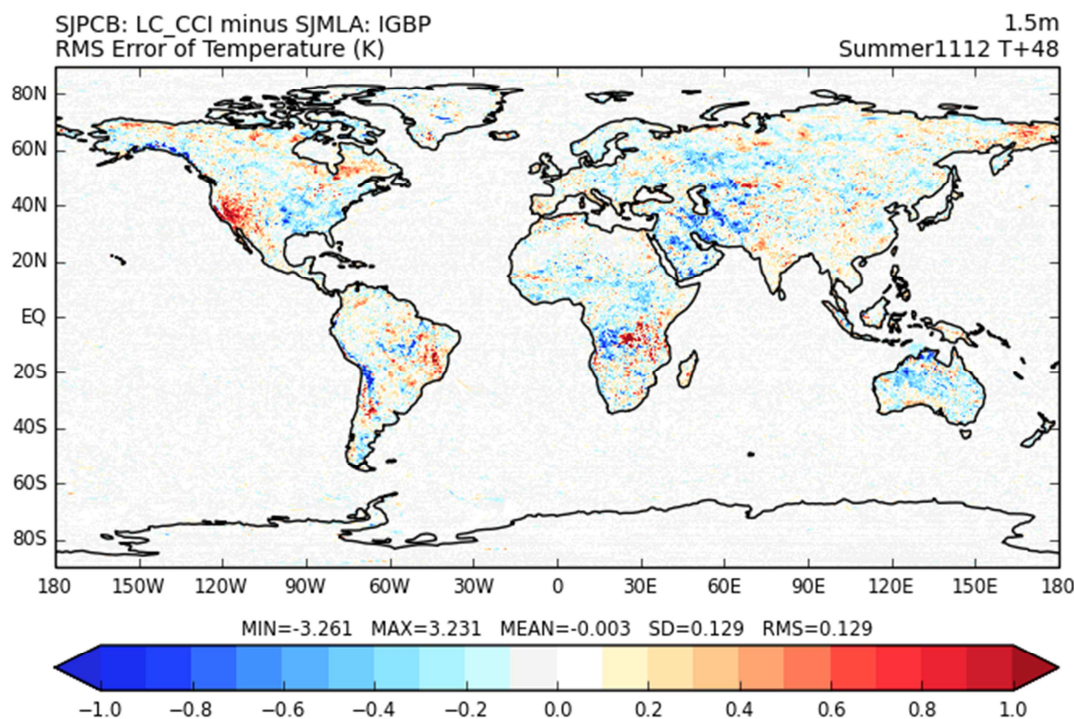


Figure 1-3. Spatial changes in Root Mean Squared (RMS) error for 1.5m air temperature during the northern hemisphere summer (2011-2012) at a forecast lead-time of 48 hours

The spatial pattern of the improvements in northern hemisphere tropical 1.5m air temperature at 48 hour lead times can be seen in Figure 1-3. Generally, northern hemisphere improvements of approximately 0.5 to 1K are found in the cropland area extending from the Black Sea, into Ukraine and Russia. Additionally, reductions in RMS error are found in the agricultural mid-West region on North America, and semi-arid regions extending from the Arabian Peninsula to the edges of the desertic area east of the Caspian Sea. In tropical regions, reductions in mean error are also found in semi-arid regions such as the Atacama desert in Chile, and central and Western Australia, as well as the open woodlands of Angola. Increases in RMS error are generally located in either sparsely vegetated or agricultural areas. This includes western North America, where an increase in shrub cover in LC\_CCI coincides with an increase in RMS.

The use of LC\_CCI did not result in improvements in all regions. In tropical land areas during the northern hemisphere winter (December to February), using LC\_CCI resulted in an increasing of the negative temperature bias (Figure 1-4 top row), and an increase in the RMS error compared to observations (Figure 1-4 bottom row). Figure 1-5 shows that these changes are largely due to increasing errors in semi-arid savannah regions of West and East Africa, in a belt extending from Senegal to Ethiopia. Furthermore, increases in temperature biases are found in India and Myanmar in largely cropland regions during the December, January, February period. Finally, increases in RMS error in the northern high latitudes (northern Russia and northern Canada) appear to coincide with areas of flooded vegetation in LC\_CCI.

Cases: —+— IGBP GA6.0 n320 —x— LC\_CCI GA6.0 n320

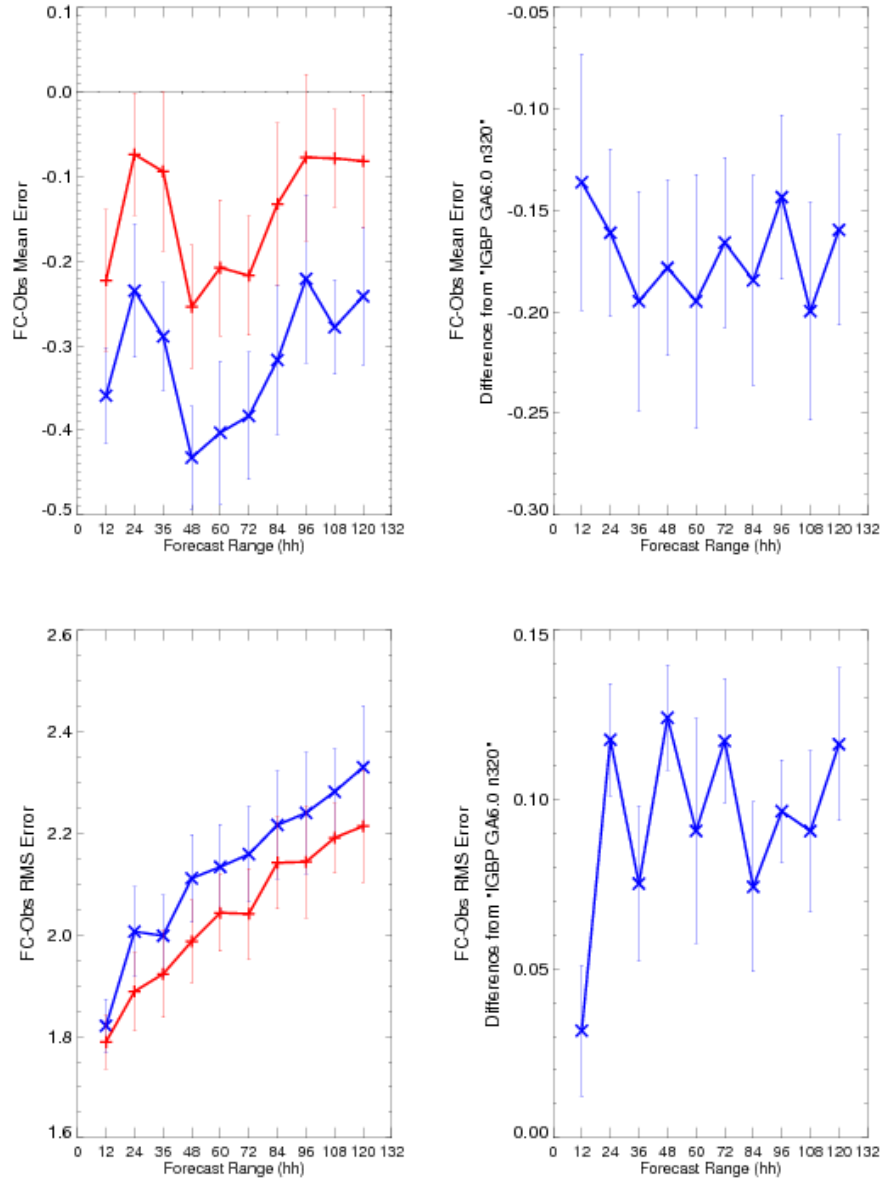


Figure 1-4. As above, but for surface air temperature over tropical land areas during the northern hemisphere winter (2010 to 2012)

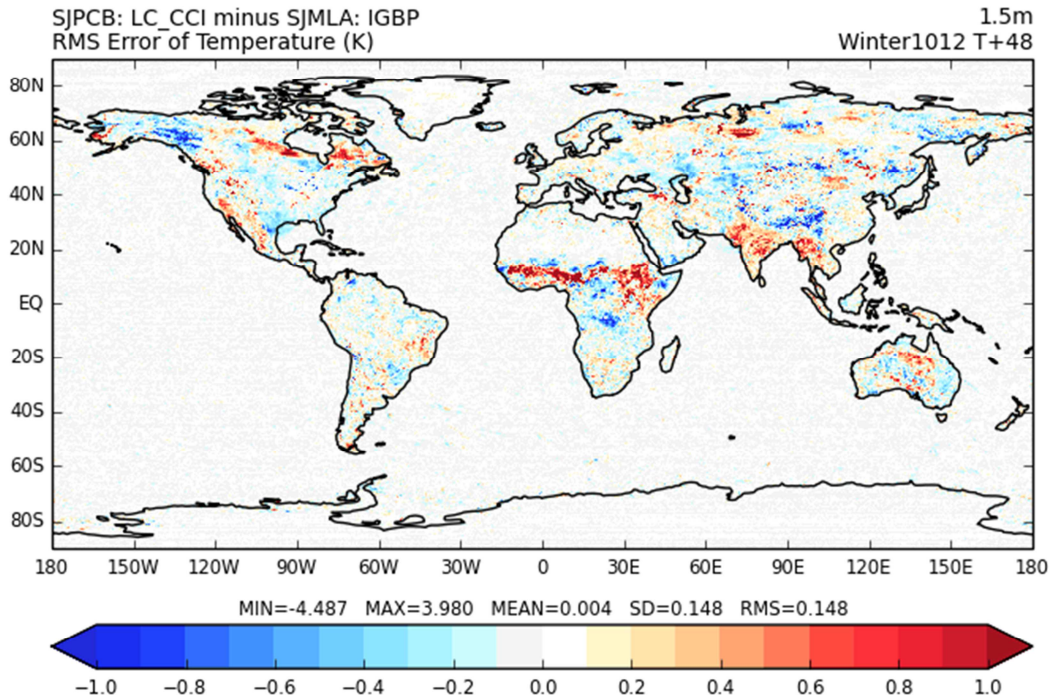


Figure 1-5. Change in RMS error of 1.5m air temperature during northern hemisphere winter at a forecast lead time of 48 hours

### Relative humidity

Changes in surface relative humidity are also evident in the LC\_CCI simulations. During the June-July-August period, reductions in the RMS error were found at all forecast lead times for North America land points (Figure 1-6). For tropical land points (Figure 1-7) small reductions in RMS error were found at forecast lead times of greater than 60 hours. In North America, the general improvement in RMS error is related to increases in relative humidity by greater than 1% (Figure 1-8), however, this is less clear over tropical areas.

Cases: —+— IGBP GA6.0 n320 —x— LC\_CCI GA6.0 n320

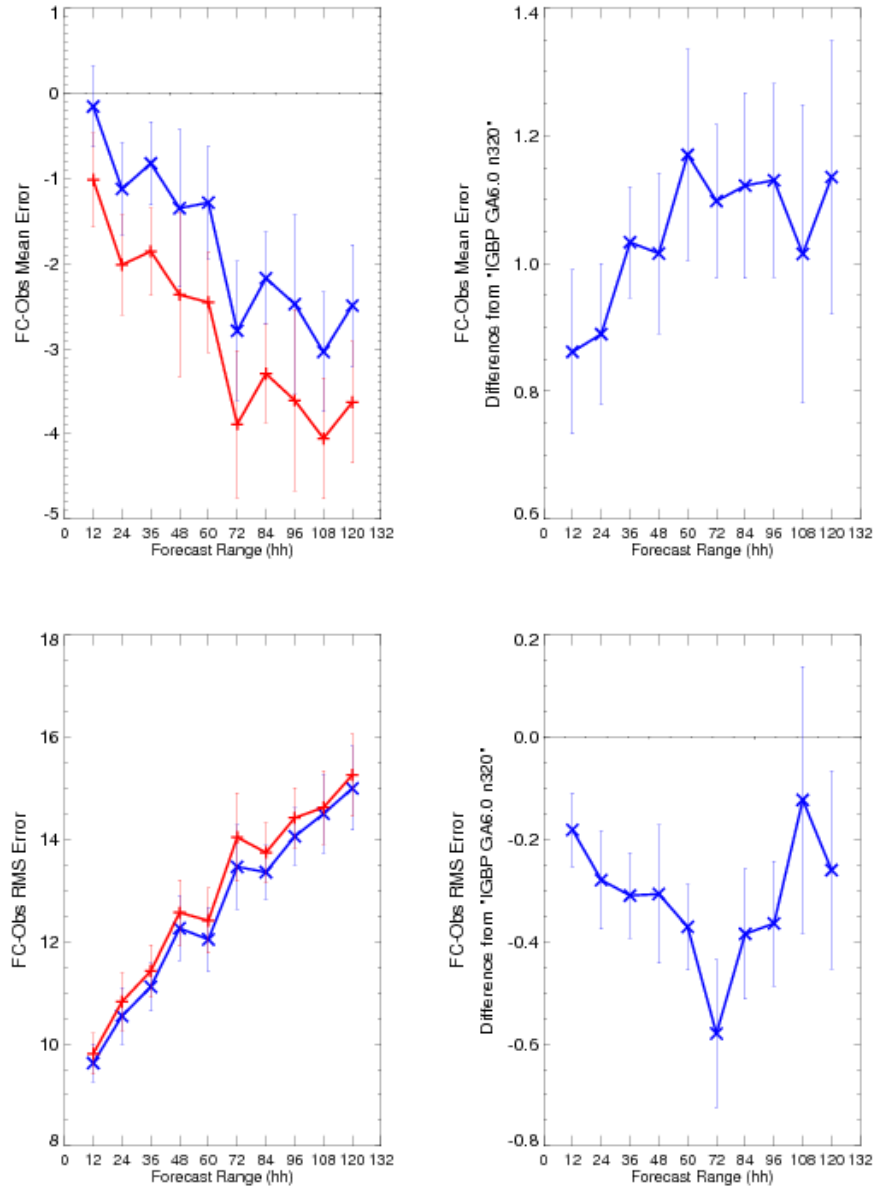


Figure 1-6. Summary of the change in the mean error and RMS error of northern hemisphere summer time relative humidity (%) forecasts for North America land points (90N to 20N) between 10/06/2011 and 23/08/2012. Red lines denote results from the control simulation using IGBP land cover, and blue lines denote simulations using LC\_CCI 2010 epoch. On all 4 plots, x-axis shows forecast range time, and y-axis shows mean absolute error in comparison to observations (top left), change in mean error (top right), RMS error (bottom left), and change in RMS error (bottom right). Error bars show standard error at 68% confidence level.

Cases: —+— IGBP GA6.0 n320 —x— LC\_CCI GA6.0 n320

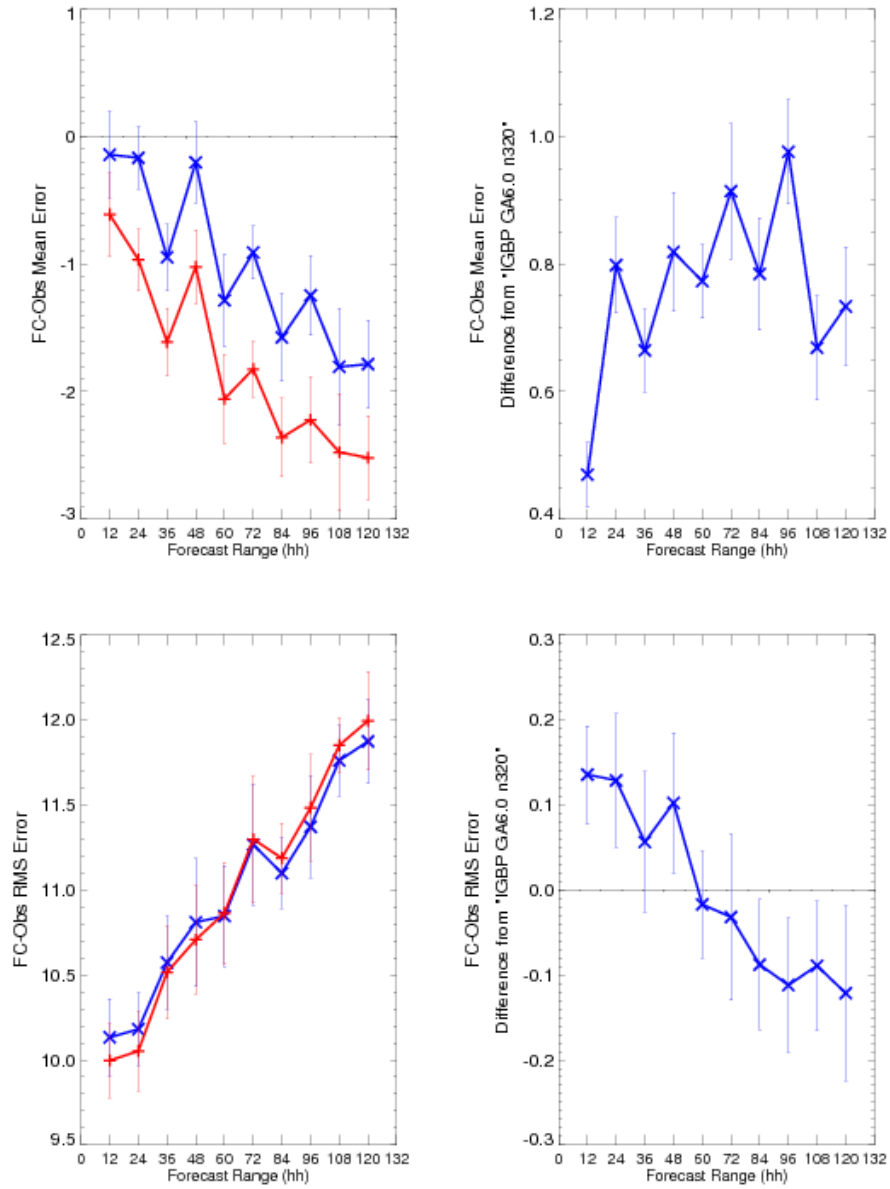


Figure 1-7. As above, but for tropical land points only

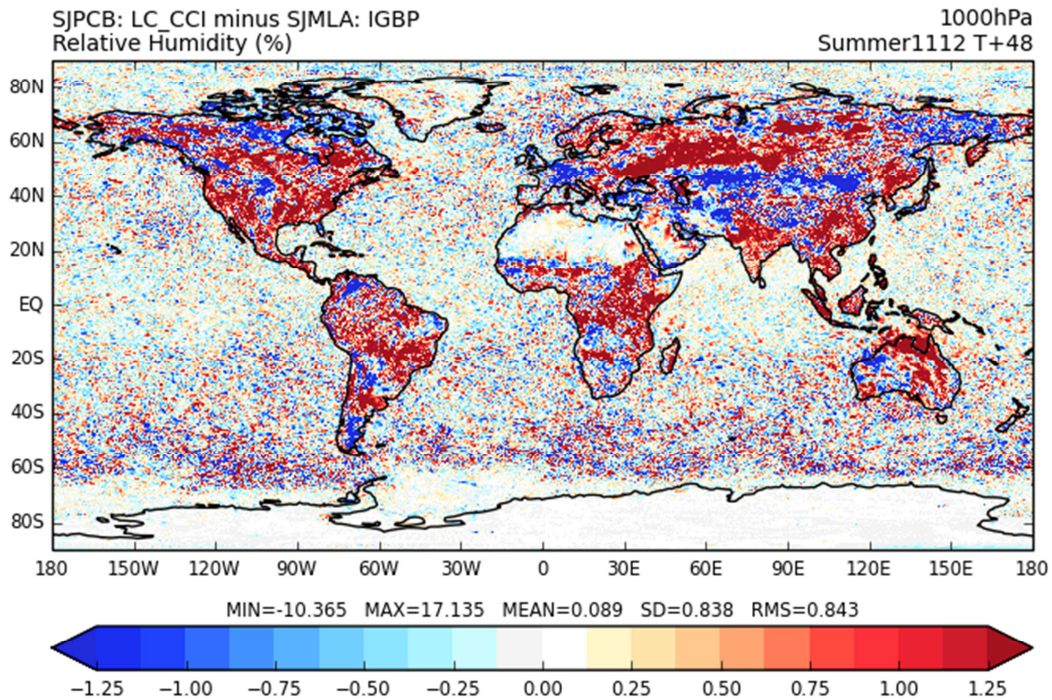


Figure 1-8. Absolute differences in surface (1000hPa) relative humidity (%) for northern hemisphere summer, at a forecast lead time of 48 hours

### 1.3.2 HadGEM3-AO Results

Increases in mean March-April-May 1.5m air temperatures are found in high northern latitudes under the LC\_CCI simulations, relative to the HadCRUT3 global monthly mean temperature dataset [RD.2]. In north-western Canada and Alaska, a temperature increase of up to 4K is found, correcting a large negative bias in this area (Figure 1-9). Similar changes also appear to occur in north and north-eastern Russia; however, it is more uncertain whether these increases are improvements given the lack of climate observations in the region (Figure 1-9; panel d). Simulated air temperature at 850mb height (close to the surface in the vertical dimension) was also compared to ERA-Interim reanalysis (Figure 1-10) for the March-April-May period. This also showed an improvement in mean temperatures for the season due to an increase in mean temperature by 2-3K.

	Ref	LC CCI Climate Assessment Report v1		
	Issue	Page	Date	
	1.0	28	13.07.2015	

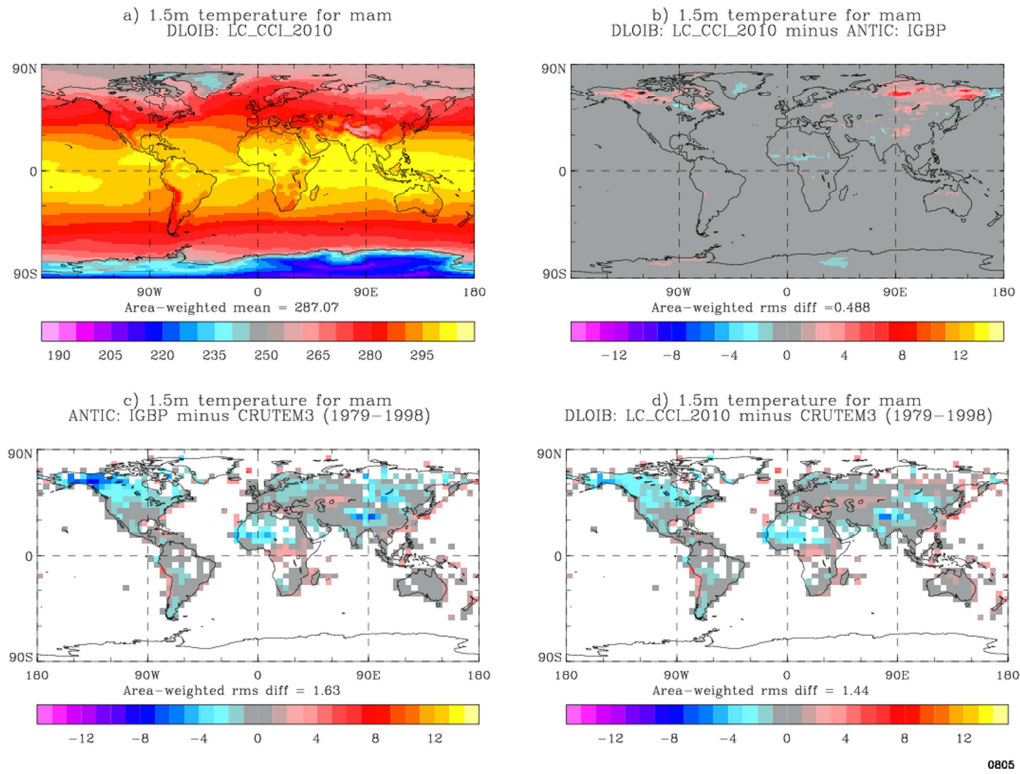
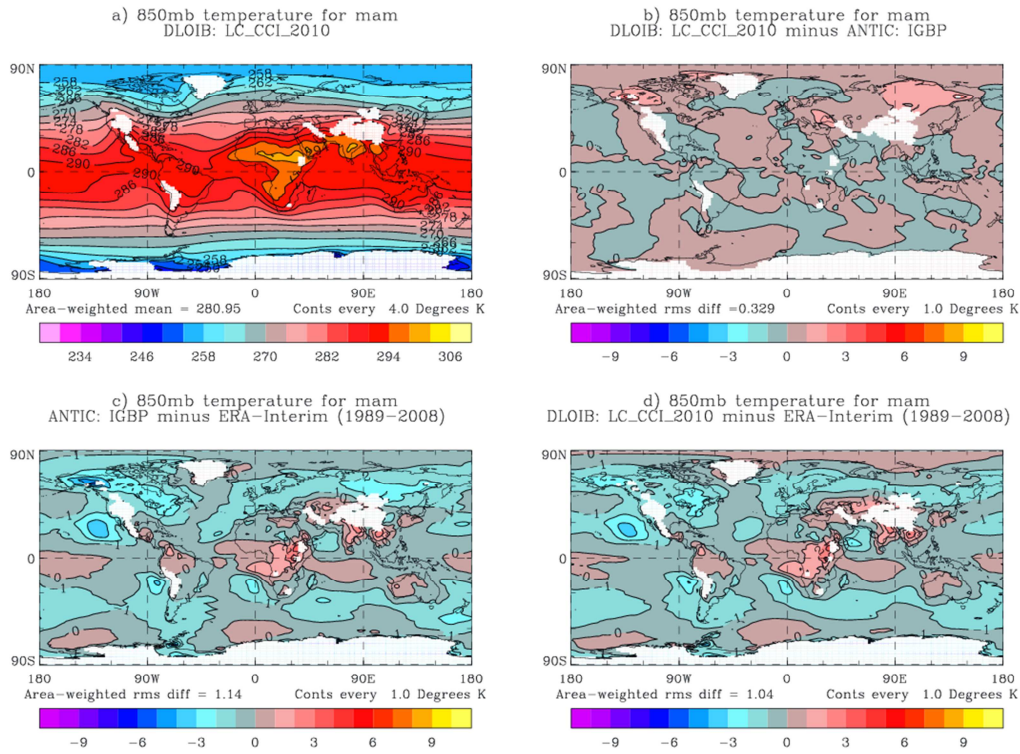


Figure 1-9. Change in March-April-May mean 1.5m air temperature in HadGEM3-AO simulations with LC\_CCI compared to IGBP land cover. Model simulations are compared to HadCRUT3 surface temperature observations for 1979-1998. Panels show (a) spatial distribution of temperature (Kelvin), (b) temperature difference between the two simulations (positive numbers show increases in LC\_CCI w.r.t. IGBP), (c) temperature anomaly for IGBP simulations compared to HadCRUT3, and (d) temperature anomaly for LC\_CCI simulations compared to HadCRUT3.



0475

Figure 1-10. As above, but for temperature at the height of 850mb air pressure compared to ERA-Interim for the period 1989-2008

In the LC\_CCI simulations, small changes are found in the RMSE of monthly GPP. However, in comparison to monthly estimates by [RD.19], notable improvements of up to  $10 \text{ g/m}^2/\text{day}$  are found in eastern China, central and eastern Europe, and the eastern Amazon. In Europe and China, these reductions in RMSE account for up to 50% of the IGBP error (Figure 1-11; bottom right). Decreases in annual GPP in the western Amazon are also associated with reductions in RMSE.

	Ref	LC CCI Climate Assessment Report v1		
	Issue	Page	Date	
	1.0	30	13.07.2015	

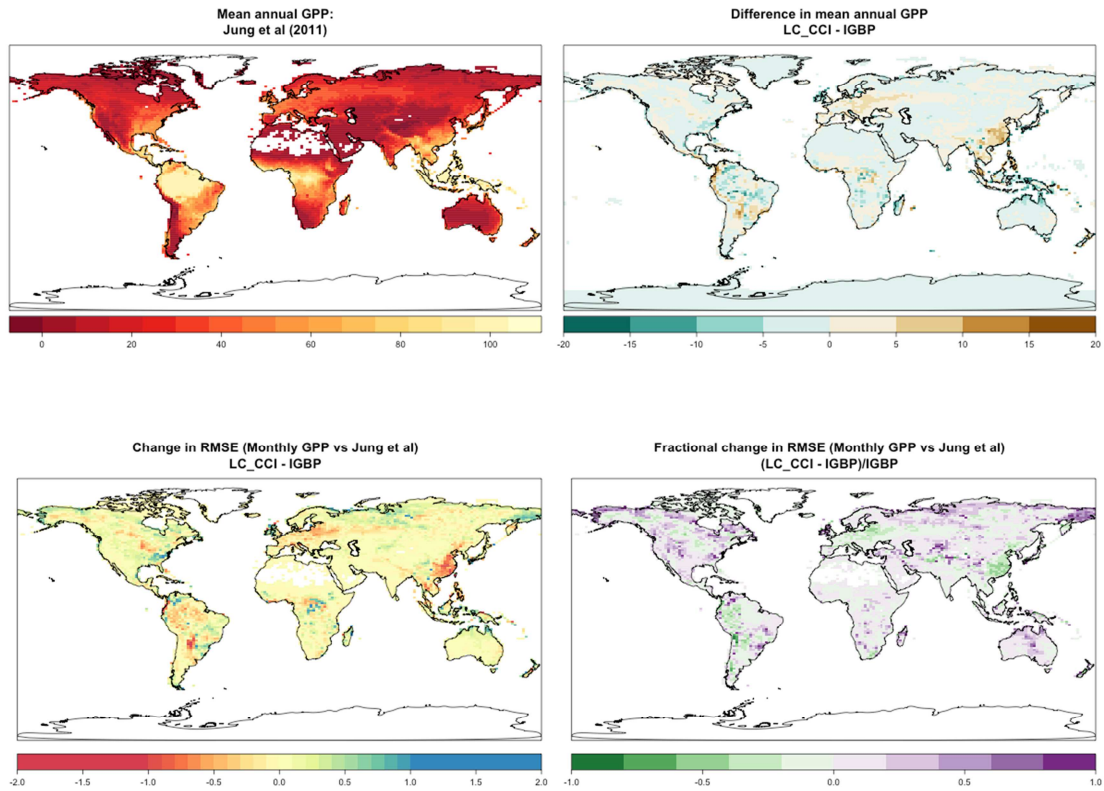


Figure 1-11. Change in simulated monthly Gross Primary Production (GPP) in relation to monthly GPP estimates by [RD.19] for the period 1982-2011. Panels show mean annual GPP estimates from [RD.19] (top left), absolute difference between the IGBP and LC\_CCI simulations (top right), change in root mean square error (RMSE), and fractional change in RMSE (bottom right).

	Ref	LC CCI Climate Assessment Report v1		
	Issue	Page	Date	
	1.0	31	13.07.2015	

Changes in RMSE for latent heat flux (Figure 1-12) are mostly found in arid or semi-arid areas, such as northern Australia, central North America, eastern Brazil, and the area stretching from Iraq to Kazakhstan. Notable areas of increases in RMSE are found in eastern China and Central and Eastern Europe, coinciding with the area of improvement in GPP estimates. In these locations, an increase in GPP has led to an increase in photosynthetic activity, which leads to an increase in latent heat flux via transpiration.

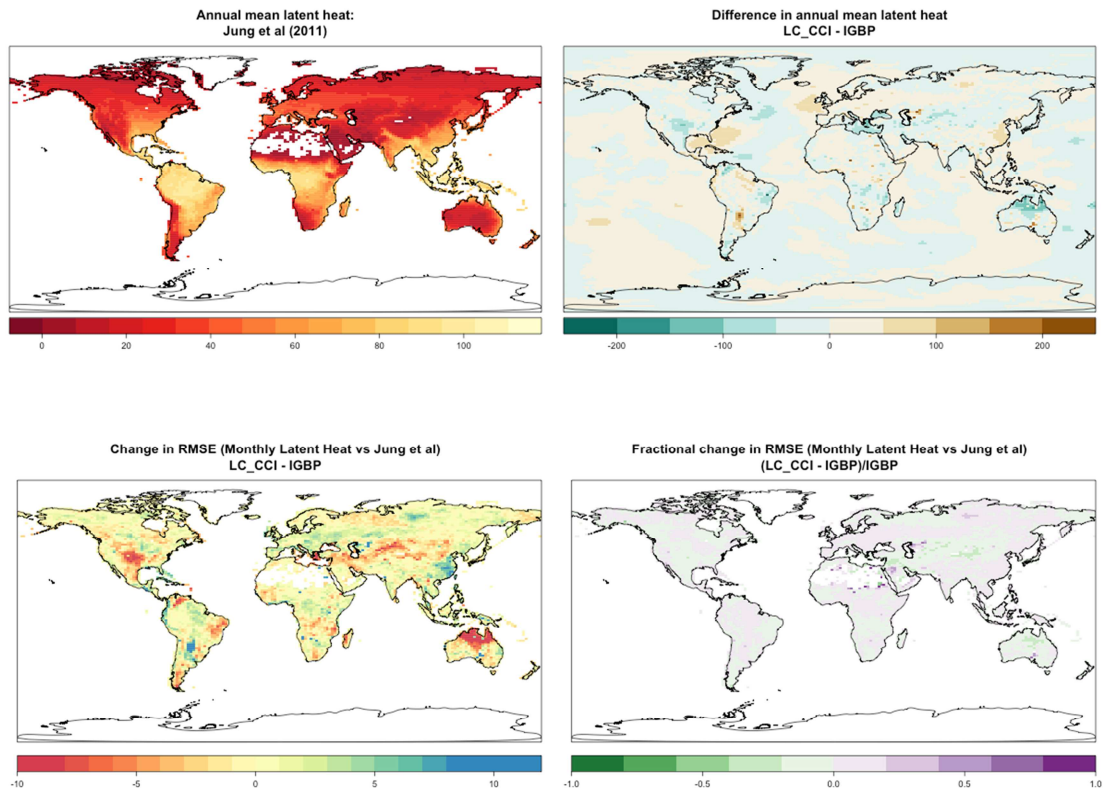


Figure 1-12. Change in simulated monthly latent heat flux ( $Wm^2$ ) in relation to monthly estimates by [RD.19] for the period 1982-2011. Panels show mean annual latent heat flux estimates from [RD.19] (top left), absolute difference between the IGBP and LC\_CCI simulations (top right), change in root mean square error (RMSE), and fractional change in RMSE (bottom right).

	Ref	LC CCI Climate Assessment Report v1		
	Issue	Page	Date	
	1.0	32	13.07.2015	

Differences in sensible heat flux between the LC\_CCI and IGBP simulations (Figure 1-13) are associated with areas of sparse vegetation or bare soil. In the high northern latitudes of Russia and Canada, increases in RMSE were found in locations where patches of sparse vegetation mixed with tree cover. Additionally, big increases in the bare soil fraction (Figure 1-14) in the deserts of Central Asia, the middle East, central Australia, and the Sahel, have led to reductions in sensible heat flux, which compared to [RD.19], represents a reduction in RMSE (Figure 1-13; bottom left).

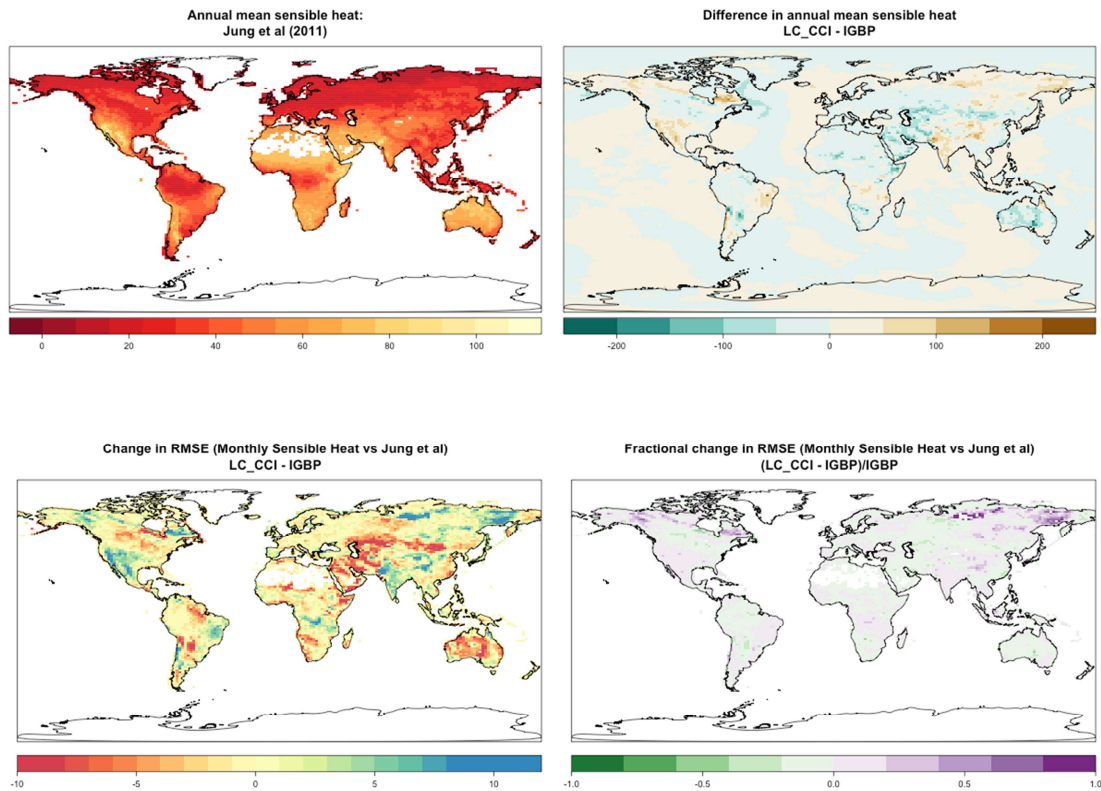


Figure 1-13. Change in simulated monthly sensible heat flux ( $Wm^2$ ) in relation to monthly estimates by [RD.19] for the period 1982-2011. Panels show mean annual sensible heat flux estimates from [RD.19] (top left), absolute difference between the IGBP and LC\_CCI simulations (top right), change in root mean square error (RMSE), and fractional change in RMSE (bottom right).

## Atmospheric Dust

Dust emissions from the land surface play a key role in the short-wave and long-wave radiation budget of the Earth. High concentrations of atmospheric dust can have a large radiative cooling effect on the both the land and ocean surface as it reflects solar energy that would have reached the surface, and consequently leads to a warming of the atmosphere. The radiative effect of dust also affects regional wind and rainfall patterns, and has been shown to have impact on the global carbon cycle [RD.10]. Therefore, dust is an important element of the earth system, and provides a mechanism by which land cover, in particular bare soil fraction, can impact earth system models.

	Ref	LC CCI Climate Assessment Report v1		
	Issue	Page	Date	
	1.0	33	13.07.2015	

Dust emissions occur from dry bare soils, therefore the fractional coverage of bare soil can influence the amount of dust available for transport in the atmosphere. The LC\_CCI 2010 product shows relatively large increases in bare soil fraction over most of the Earth's arid environments (Figure 1-14). Increases in bare fraction, relative to the IGBP land cover, are found over central Australia, central Asian deserts, and on the edge of the Sahara. Smaller increases of up to 30% extra bare soil fraction are found in central North America, southern Africa and the high northern latitudes. Many of these changes can be traced to both larger extents of bare soil and sparse vegetation classes, as well as differences in the cross-walking conversion matrix between LC\_CCI and IGBP approaches.

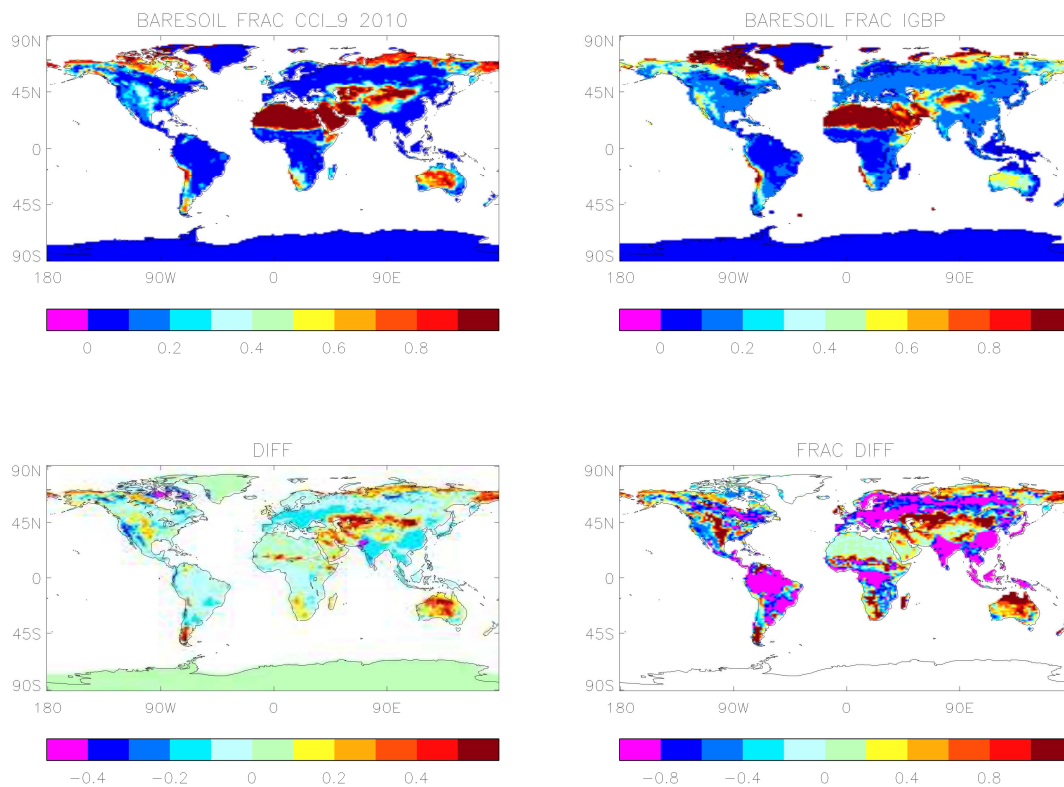


Figure 1-14. Bare soil fraction derived from LC\_CCI (top left) and IGBP (top right) land cover maps. Absolute difference ( $IGBP - LC\_CCI$ ) is shown in the bottom left, and fractional difference  $((IGBP - LC\_CCI)/IGBP)$  in the bottom right.

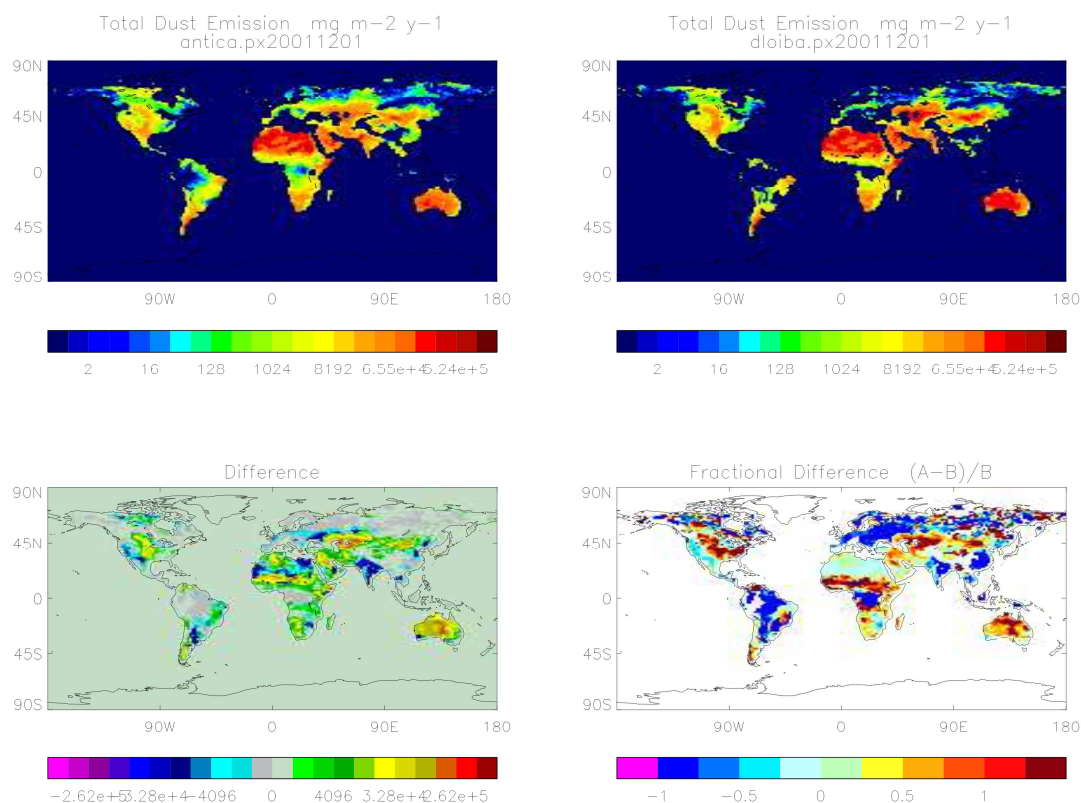


Figure 1-15. Total dust emissions ( $\text{mg}/\text{m}^2/\text{yr}$ ) derived from each land grid cell for simulations using IGBP (*antica*; top left) and LC\_CCI (*dloib*; top right). Absolute difference is shown in the bottom left (LC\_CCI – IGBP), and fractional difference  $((\text{IGBP} - \text{LC\_CCI})/\text{IGBP})$  in the bottom right.

Figure 1-15 shows that the emission from the land surface has increased under LC\_CCI in many of the regions where an increase in bare soil fraction was found. This is especially the case in central Asia, Australia, Sahelian Africa, and North America, where dust emissions have increased by more than 100%. This is also evident in Figure 1-16, which shows the total dust load in the atmosphere. Here, northern Australia and central Asia stand out as locations where the atmospheric load of dust has increased by more than 100%. This equates to up to an extra  $255 \text{ mg}/\text{m}^2$  of dust in the atmosphere over Australia and central Asia. Large fractional increases in dust load are also found over central North America and north-western Russia; however, atmospheric dust concentrations are generally much lower in these regions.

	Ref	LC CCI Climate Assessment Report v1		
	Issue	Page	Date	
	1.0	35	13.07.2015	

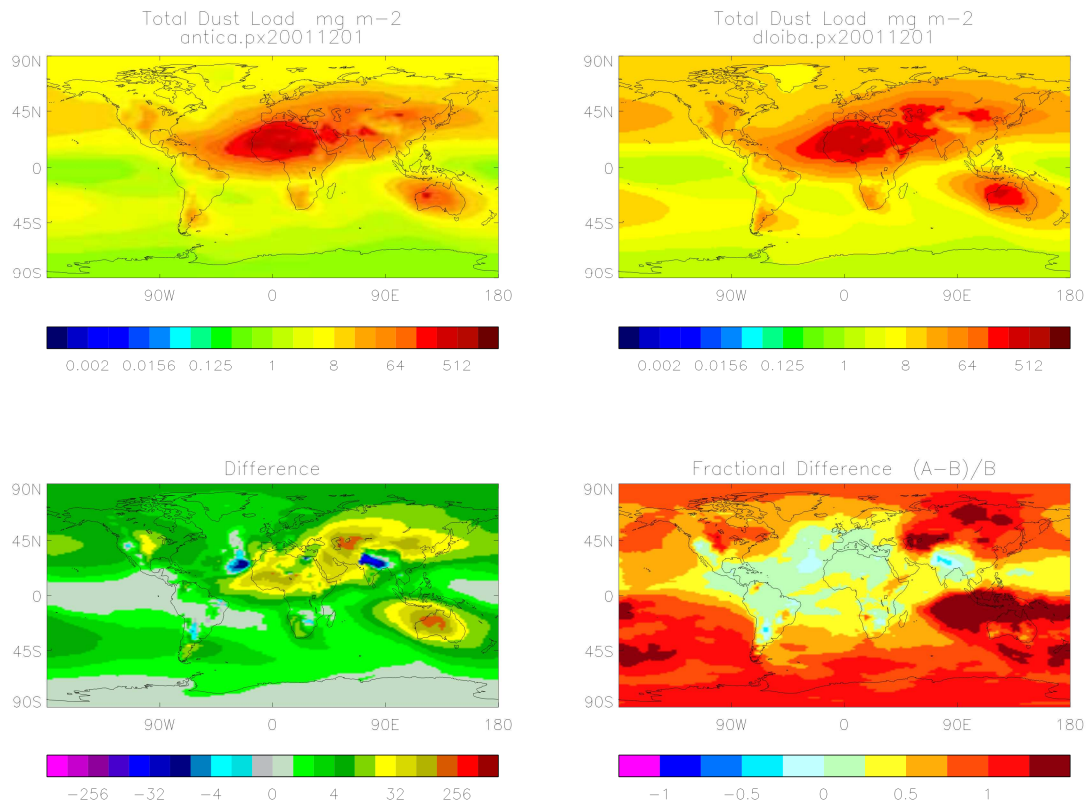


Figure 1-16. Total dust load ( $\text{mg}/\text{m}^2$ ) in the atmosphere for simulations using IGBP (antica; top left) and LC\_CCI (dloib; top right). Absolute difference is shown in the bottom left (LC\_CCI - IGBP), and fractional difference  $((\text{IGBP} - \text{LC\_CCI})/\text{IGBP})$  in the bottom right.

A major limitation of the assessment of climate models for dust emissions and transport is the lack of availability of long-term, spatially explicit observations of atmospheric dust. Where site-specific observations are available, one study found that climate models systematically underestimate dust emission, transport, and optical depth [RD.4], although this study fails to account for the fact that satellite products are to some extent also models with assumptions that maybe incompatible with climate models. The Moderate Resolution Imaging Spectro-radiometre (MODIS) and Multi-angle Imaging Spectro-radiometre (MISR) sensors onboard NASA's Terra satellite both provide estimates of aerosol optical depth (AOD) at 550nm wavelength. This wavelength is sensitive to a range of particle sizes (from 0.5 to 9microns), and provides a measure of the amount of solar radiation that is reflected or absorbed by all atmospheric aerosols.

Climate models are also able to calculate aerosol optical depth at 550nm wavelength, for comparison with satellite observations. The AMIP simulations used in this report account for observed historical emissions of sea salt, sulphate, black carbon, biogenic and organic carbon aerosols, which in addition to modelled dust emissions from the land surface, provide a reasonable basis for comparison with satellite observations. However, when making a simple comparison of satellite AOD to modelled AOD, there are a number of caveats to consider. These include the spectral properties of the underlying soil, cloud screening algorithms [RD.14], non-sphericity of dust [RD.8] and the

	Ref	LC CCI Climate Assessment Report v1		
	Issue	Page	Date	
	1.0	36	13.07.2015	

reflectance properties of the mineral dust particles suspended in the atmosphere. Generally speaking, satellite observations of AOD are less reliable over very bright land surfaces [RD.17]. Additionally, the HadGEM3 dust scheme assumes that dust from all sources has the same size-dependent radiative absorbing and reflecting properties, that are calibrated based on observations over the Sahara (the largest global source of dust). The combination of both of these factors means that land based comparisons of satellite and modelled AOD has significant uncertainty.

Given the above caveats, Figure 1-17 shows that both simulations used in this study underestimate AOD, in comparison to satellite observations (Figure 1-17; row 1 compared to row 2). However, the increase in dust emissions in the LC\_CCI simulations (Figure 1-15 and Figure 1-16) also appears to lead to an improvement in AOD, especially in locations such as central Asia and Australia. Here, the absence of stippling in the LC\_CCI simulations (Figure 1-17; row 3 and 4, column 2) shows that the dust contribution to AOD is more than 50%. In these locations, we would expect improvements to the AOD to be related to increases in the dust load. This is indeed the case in central and northern Australia, and in a belt stretching from the Caspian Sea across central Asia to Mongolia. Simulated AOD using LC\_CCI is quite similar to MISR estimates of AOD in these areas. Increases in the dust load over West Africa (Figure 1-16; bottom left) were also found to lead to a reduction in the underestimation of AOD for the region, and for the related dust plume in the Atlantic Ocean.

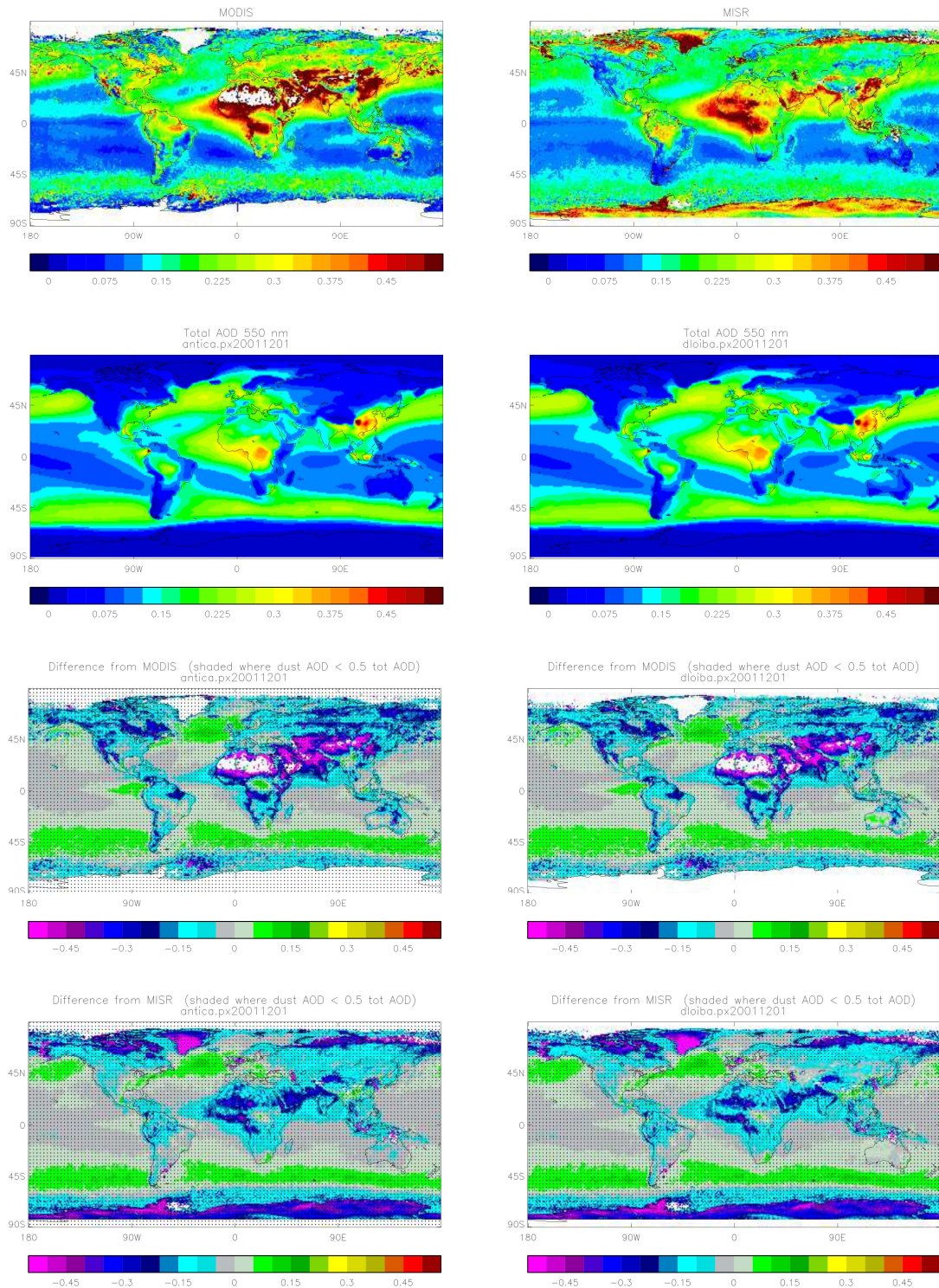


Figure 1-17. Comparison of aerosol optical depth (AOD) at 550 nm wavelength derived from MODIS (top left) and MISR (top right) to AOD from IGBP simulations (2<sup>nd</sup> row left) and LC\_CCI simulations (2<sup>nd</sup> row right). Differences between both simulations and MODIS (3<sup>rd</sup> row), and MISR (4<sup>th</sup> row) are also shown. The absence of stippling denotes areas where the total simulated AOD is comprised of more than 50% dust.

	Ref	LC CCI Climate Assessment Report v1		
	Issue	Page	Date	
	1.0	38	13.07.2015	

## 1.4 Summary

### *Global NWP Case Studies*

The key messages from the LC\_CCI simulation in comparison to the IGBP simulation are:

- There are small improvements in 1.5m air temperature and relative humidity for many land areas. These include:
  - June-July-August (JJA) improvements for Northern Hemisphere land and Tropical land
  - December-January-February (DJF) improvements in relative humidity for Northern Hemisphere land and Tropical land areas.
- Improvements do not occur everywhere, and in some cases, RMS error increases. For example, RMSE increases in 1.5m air temperature over the Sahel during the dry season (DJF).

Currently, the small improvements found in the above results are not sufficient to include the LC\_CCI product in the next version of the Met Office UM. However, it is expected that further benefits will be found when other model prognostic variables such as leaf area index and canopy height are included. Therefore, the conclusions from these simulations are that model improvements will be further enhanced by greater consistency in model prognostic variables.

### *Global Climate Simulations: HadGEM3-AO*

The various configurations of HadGEM3 form the basis for the UK's next generation Earth System Model. Therefore, current developments are focused on improving model skill in relation to many different aspects of the earth system, such as the carbon and hydrological cycles, and the earth's energy budget. Work is currently on-going to increase the number of plant functional types in HadGEM3, and this will involve using the LC\_CCI epochs and cross-walking table to create new PFT distributions for static land cover simulations. Therefore, the testing of LC\_CCI in HadGEM3-AO is a timely contribution. These simulations with Land Cover CCI 2010 epoch have shown improvements in the following:

- 1.5m air temperature in high northern latitudes in March-April-May (MAM). The same locations however show deterioration in RMSE for sensible and latent heat fluxes compared to [RD.19] estimates, which themselves maybe uncertain.
- GPP improvements in RMSE for eastern China, Central and Eastern Europe and the western Amazon, with regard to [RD.19] estimates. Caution should be taken in interpreting these comparisons however, because [RD.19] estimates are based on flux tower observations up-scaled using satellite fAPAR, CRU climate observations and the SYNMAP global land cover map (a synthesis of GLC2000, MODIS, and GLCC land cover products).
- Over most global arid areas, reductions in RMS error were found in sensible and latent heat fluxes relative to [RD.19] estimates. These changes were related to increases in bare soil fraction in warm arid areas. However, increases in bare soil fraction in high northern latitudes lead to increases in RMS error relative to [RD.19].

	Ref	LC CCI Climate Assessment Report v1		
	Issue	Page	Date	
	1.0	39	13.07.2015	

- In LC\_CCI simulations, a doubling of the dust load over many of the large global deserts was found. In comparison to aerosol optical depth estimates from MODIS and MISR sensors, this represents an improvement at 550nm wavelength.

	Ref	LC CCI Climate Assessment Report v1		
	Issue	Page	Date	
	1.0	40	13.07.2015	

## 2 EVALUATING THE LAND COVER AND WATER BODY PRODUCTS IN THE CONTEXT OF CLIMATE MODELING (*MPI-M*)

### 2.1 Summary

In the frame of the LC\_CCI project, the following activities have been conducted at the Max Planck Institute for Meteorology (MPI-M):

- 1) Evaluation of the Water Body (WB) product in the context of climate simulations;
- 2) Cross-walking procedure is revisited and updated. In the interaction with the lc-user-tool developers, we also supported debugging of the tool and further development;
- 3) Exploration of Normalized Difference Vegetation Index (NDVI) and Snow seasonality product has been made in order to update other surface parameters consistently with PFT;
- 4) Evaluation of the evapotranspiration product (ET);
- 5) Sensitivity study in order to estimate uncertainty of the LC maps and cross walking procedure.

In the section 2.2, the experimental setup is described including recent developments of JSBACH. In the section 2.3, simulations with the wetland extend dynamics scheme and comparison of simulations with WB product and other available wetland observations are presented. Section 2.4 contains the description of updated JSBACH cross-walking procedure and comparison of simulations with reference MPI PFT distribution and updated LC\_CCI PFTs. In the section 2.5, a first attempt to separate albedo into soil and vegetation fraction using NDVI and Snow product is presented. However, it seems that the current NDVI data are not sufficient to complete the task. Therefore, requirements for desired properties of NDVI and Snow products are listed. Contribution to the evaluation of ET product is part of the section 4.7 of the ET deliverable. Common efforts to estimate uncertainty of the LC maps are described in section 4 of this report.

### 2.2 JSBACH land surface model

JSBACH is the land surface component of the Max Planck Institute for Meteorology's Earth System Model (MPI-ESM). It represents the lower atmospheric boundary condition in MPI-ESM, but it can be also set up to run decoupled, i.e. in an offline mode. In that case, daily atmospheric forcing is needed to drive the model. We follow that approach in our experiments and make use of WFDEI

	Ref	LC CCI Climate Assessment Report v1		
	Issue	Page	Date	
	1.0	41	13.07.2015	

(WATCH Forcing Data methodology applied to ERA-Interim data) meteorological forcing data developed by [RD.30, RD.31]. Individual characteristics of JSBACH are summarized.

JSBACH has been developed by isolating the land components from ECHAM5 [RD.27] representing numerical parametrization of the soil hydrology, the soil heat transport, and the land surface energy balance. In order to simulate complexity of other terrestrial processes such as carbon and vegetation dynamics JSBACH is substantially extended. A large number of modules have been added including but not limited to photosynthesis and canopy radiation components, prognostic phenology scheme, carbon exchange module between vegetation and soils and vegetation dynamics. Here, we do not employ the dynamic vegetation module since we are interested in the effect of prescribed land cover and its conversion to PFT. Two major developments have been included in the operational JSBACH version compared to LC\_CCI Phase 1: a new soil carbon module (YASSO7) and a five layer soil hydrology scheme [RD.21]. In addition, a scheme for wetland extent dynamics (WEED) was recently implemented into JSBACH that is based on [RD.28]. The latter will also be evaluated regarding its skill to represent the global wetland distribution.

## 2.3 Water Body evaluation

The assessment of ESA LC\_CCI WB product is threefold. The first two applications are a comparison of ESA LC\_CCI WB product with other available observations and the evaluation of simulated surface water bodies generated by the JSBACH-WEED and the MPI Hydrology Model (MPI-HM). The third assessment is based on the comparison of JSBACH simulations using prescribed ESA LC\_CCI WB product boundary conditions at the land surface and with the dynamical WEED scheme. JSBACH and MPI-HM simulations are driven by WATCH forcing data based on ERA-Interim (WFDEI) at T63 resolution and 0.5 degrees, respectively.

### 2.3.1 Simulations and observations

Three JSBACH simulations have been performed for the purpose of this comparison:

- 1) Reference simulation, denoted JSB-OFF on figures without WEED scheme;
- 2) Simulation with wetland extends dynamics, denoted JSB-WEED on figures;
- 3) Simulation with prescribed wetland extends from ESA LC\_CCI WB product, denoted JSB-ESA on figures.

The implementation of the WEED scheme into JSBACH is still work in progress. The characteristics of the scheme which solves the water balance of wetlands and estimates their extent dynamically are described in [RD.28]. Table 2-1 shows the current status of development and implementation of the WEED scheme into JSBACH.

	Ref	LC CCI Climate Assessment Report v1		
	Issue	Page	Date	
	1.0	42	13.07.2015	

Table 2-1. Status of the development and implementation of WEED scheme into JSBACH

Development status in JSBACH			
Topic	Concept	Tested	JSBACH
Excess surface water	✓	✓	✓
Vertical water flows	✓	✓	✓
Horizontal wetland dynamics	✓	✓	✓
Lateral water flows	✎	✎	✎
Global parameter tuning	✓	✓	✎
Albedo and heat capacity	✗	✗	✗

Albedo and heat capacity calculations according to the wetland distribution are currently missing. Lateral flow (downstream transport) implementation is still work in progress. Current status is, that lateral outflow from one grid cell is already included and is given to the routing scheme (HD-Model), but no lateral inflow into the wetland can occur yet. Therefore lateral inflow does not yet contribute to the wetland extend.

The WB product is delivered as a stand-alone data set within Phase 2 but it is also incorporated in the global LC maps as the class 210. The following observational data sets are compared to the ESA LC\_CCI WB product as well as to distributions simulated by JSBACH WEED and MPI-HM:

- Global lake and wetland database (GLWD) by [RD.22];
- Land surface parameter 2 (LSP2) by [RD.20];
- Wetland ecosystem map (MATT) by [RD.23];
- Satellite derived inundation (SIND) by [RD.25, RD.26].

All of these datasets differ in their definitions of water bodies, resolutions, period of observation and observational methods. Therefore they show reasonable disagreement among each other. However, some agreement between all the datasets can be found as it will be shown in the following section.

### 2.3.2 Wetland extend comparison

Figure 2-1 shows the global maximum extent of the wetlands according to various datasets. Bottom rows are three model simulations. Both simulations with the wetland dynamics extend scheme (JSB-WEED and MPIHM) strongly overestimate extension of wetlands in tropical latitudes, especially in the Amazon and Congo River basins. The simulation with prescribed wetland boundaries (JSB-ESA) reduces the wetland extend even in comparison with ESA-CCI-WB.

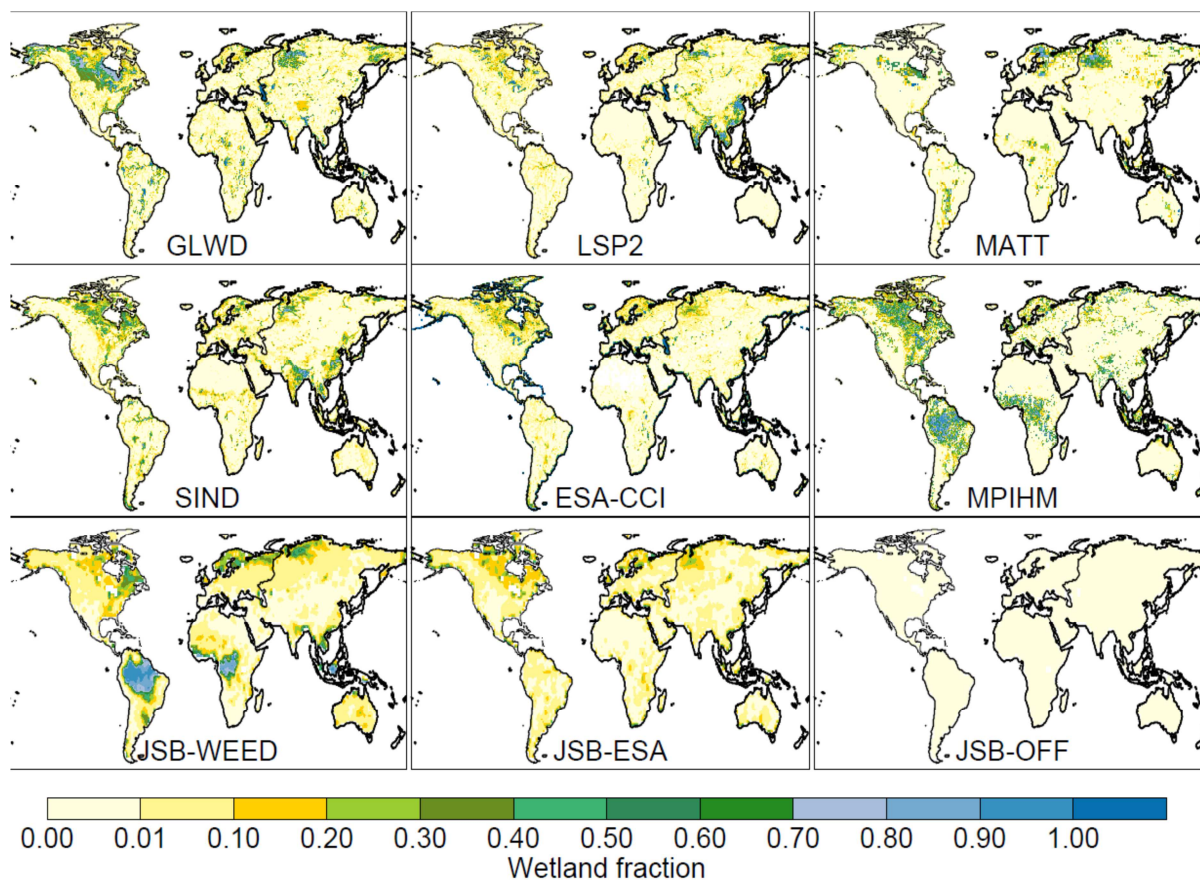


Figure 2-1. Maximum wetlands extend according to various observations and model simulations.

This is to be expected, since the LC\_CCI WB product represents maximum wetland extend. Therefore JSB-ESA cannot be larger than LC\_CCI WB. However, there are some grid cells inside prescribed boundaries of LC\_CCI WB for which the available water calculated from the surface water balance does not support the formation of wetland in the respective grid point. Also seasonal dynamics may contribute to the decrease of the simulated extend of actual wetlands that is smaller than the maximum extend. Thus, JSB-ESA will on average be always less than LC\_CCI WB. Not fully implemented lateral flow might also contribute to the reduced wetland extend in the JSB-ESA. Outflow that might reduce wetland is included in the scheme, but inflow that might increase the size of a wetland is still missing (see Table 2-1).

The zonal distribution of wetlands (Figure 2-2) provides quantified insight into the extension of wetlands according to various observations and simulations. Except in the tropics, all models are in the range of uncertainty of observations. While JSBACH-WEED and MPI-HM simulations in tropical latitudes strongly overestimate wetland extend, JSBACH-ESA simulation remains on the lower limit of the uncertainty of observations.

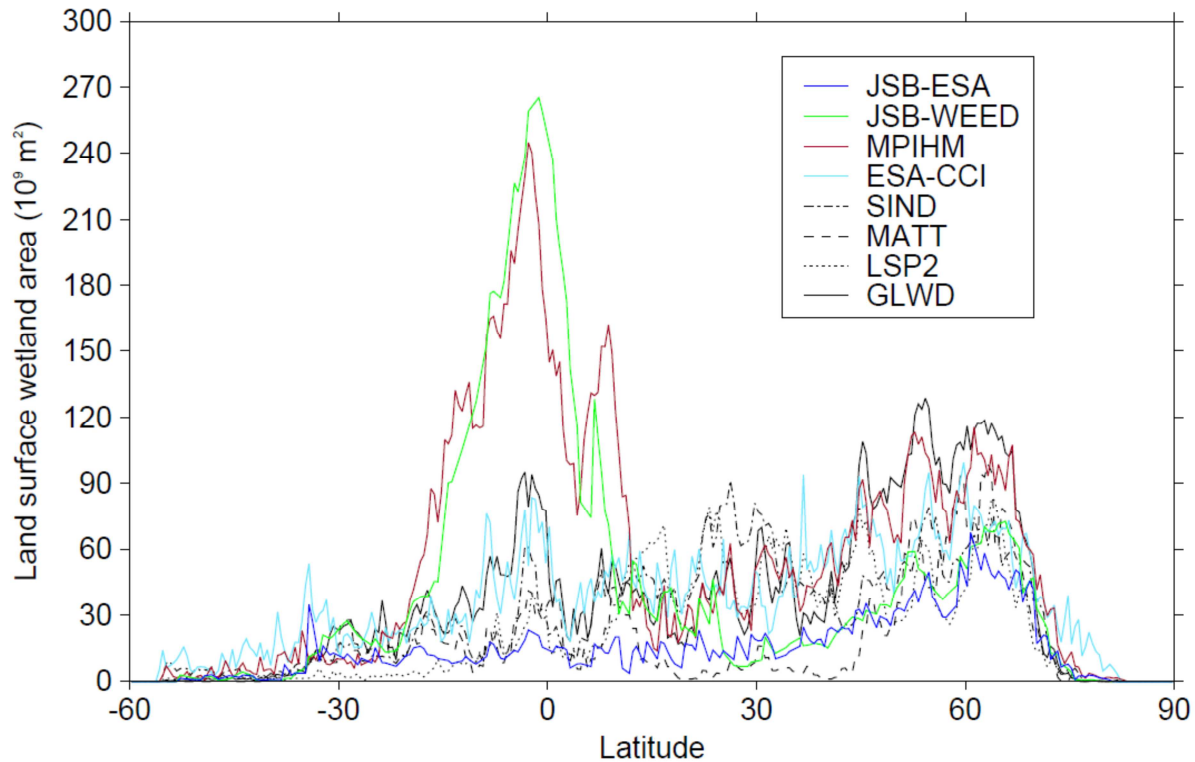


Figure 2-2. Zonal extend of wetlands from various datasets.

Figure 2-3 demonstrates that simulations with implemented wetland scheme either dynamical (WEED) or prescribed (ESA) introduce physically consistent changes into the JSBACH model. A comparison with Figure 2-1 demonstrates that the introduction of wetlands in the model leads to an increase of evaporation and a cooling of the surface. In certain parts of the world (eastern North America, tropical eastern South America, tropical Africa) evapotranspiration is stronger in the WEED simulation (and therefore cooling as well) than in the ESA simulation, as the dynamical scheme allows for a larger horizontal extend of wetlands than prescribed by ESA LC\_CCI WB product. Comparison of pond evaporation and pond depth (Figure 2-4) between WEED and ESA simulations suggest that excess water in the ESA simulations is deepening the pond reservoir while in the WEED simulations it contributes to the increase of evapotranspiration. It is worth to note here again, that these are both offline simulations, where the same amount of precipitation is prescribed by the forcing data, but it will be interesting to see how the wetland extend will affect precipitation in simulations coupled to an atmospheric component. Figure 2-5 shows seasonal cycles of evapotranspiration and runoff for three river basins (Amazon, Niger and Nile). It demonstrates that the implementation of WEED does not provide a systematic improvement of evapotranspiration. In the Amazon River basin, all three simulations strongly underestimate the seasonal cycle of evapotranspiration, while in the Niger River basin all three are in good agreement with observations. In the Nile river basins, the LC\_CCI WB simulation shows slightly better agreement with observation than the other two simulations. For the total runoff we have systematic decrease of runoff peaks for all three basins. The reference simulation has the highest amplitudes, while the WEED simulation has the lowest.

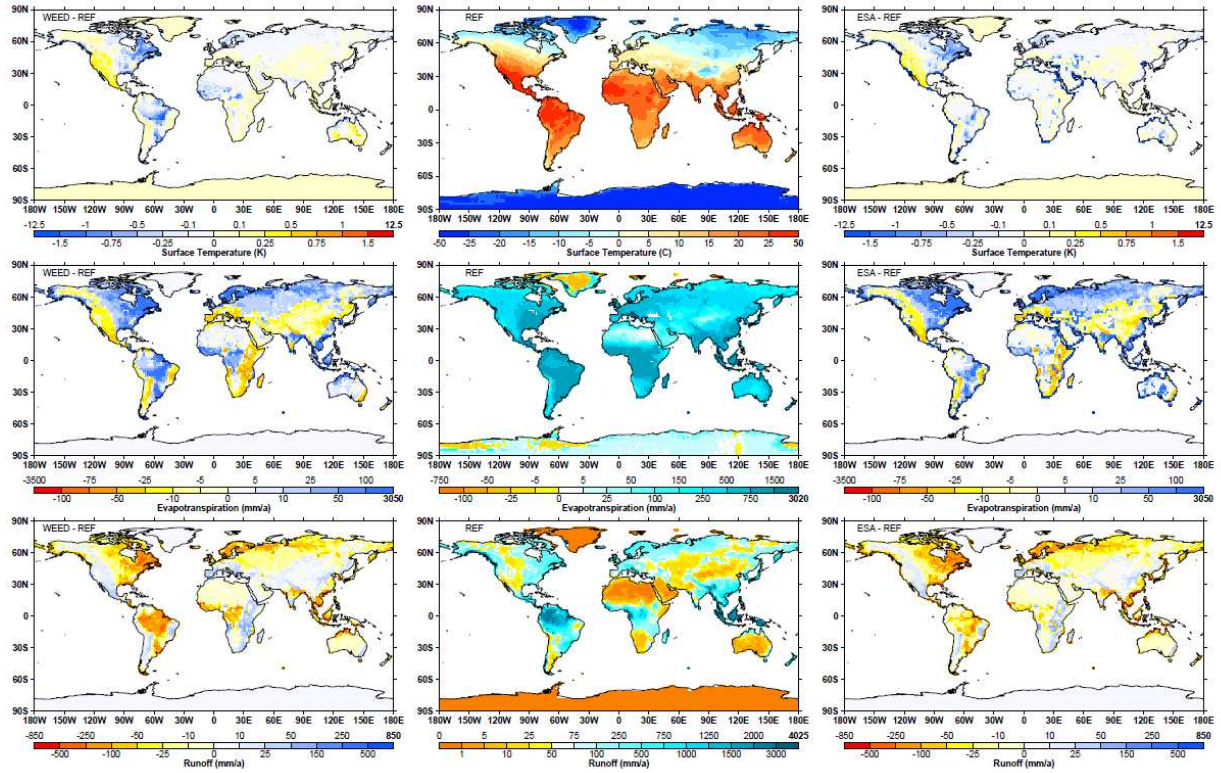


Figure 2-3. From top to bottom surface temperature, evapotranspiration and runoff. In the middle are absolute values for the reference simulation (REF) without wetlands, and on the left hand side difference WEED-REF, and on the right hand side ESA-REF

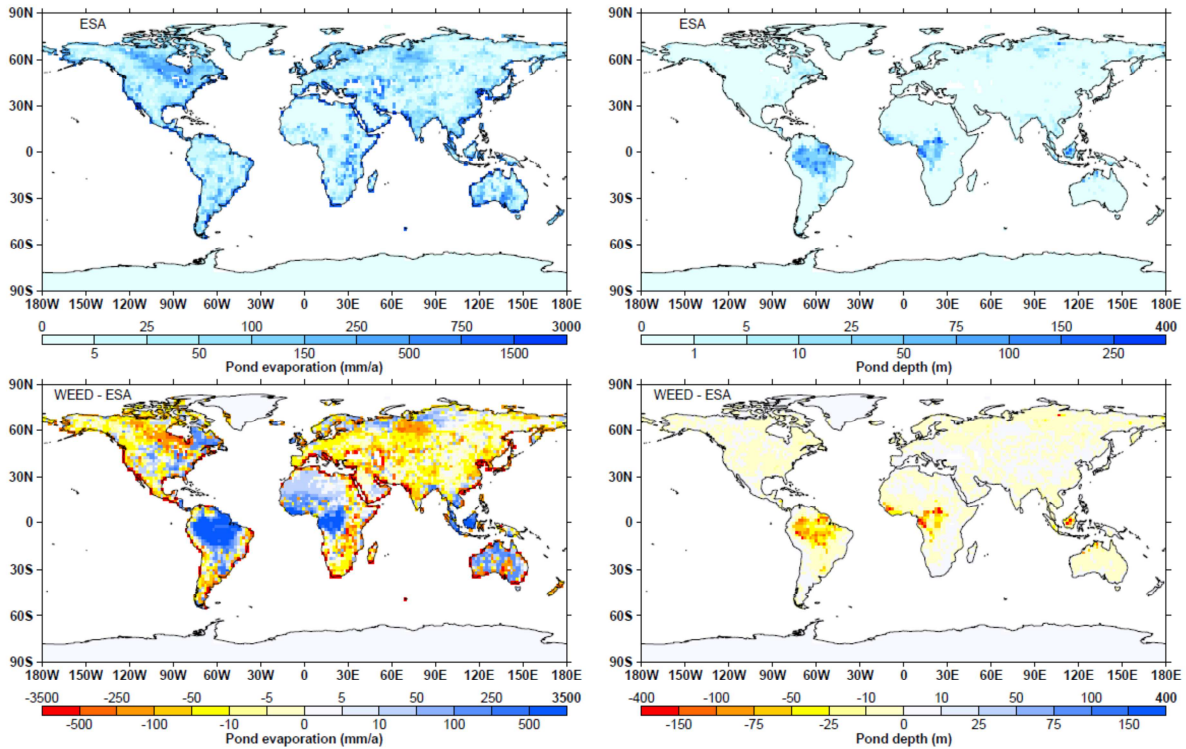


Figure 2-4. Pond evaporation and pond depth for ESA simulation (top) and difference WEED-ESA (bottom)

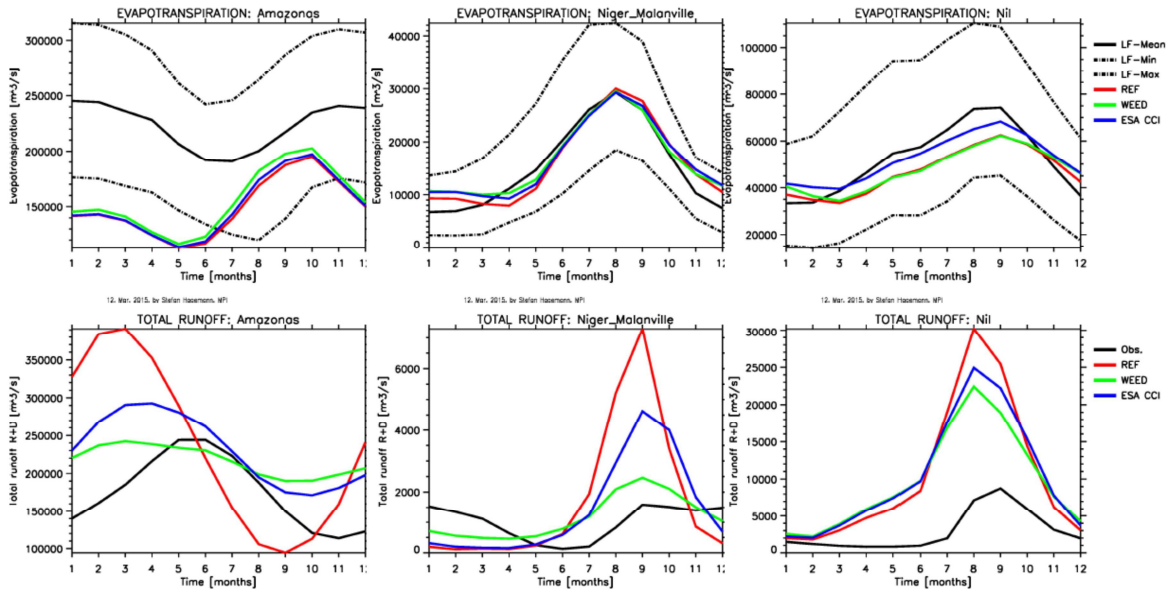


Figure 2-5. Seasonal cycle of evaporation (top) and total runoff compared with GRDC river discharge (bottom), for river basins of Amazon, Niger and Nile. Note that there must be a delay between total runoff and discharge as the former does not include the lateral transport through the river network.

	Ref	LC CCI Climate Assessment Report v1		
	Issue	Page	Date	
	1.0	47	13.07.2015	

### 2.3.3 Conclusions and outlook

Global observational datasets of wetland extend differ in their definition of a wetland, resolution, period of acquisition, method of observation and data processing. This results in a large range of uncertainty in the observational data. Model simulations with JSB-WEED and MPI-HM fit in that range of uncertainty, except in the equatorial latitudes and in particular in the Amazon and Congo River basins. This is probably due to underestimated evapotranspiration and a lack of lateral flow implementation into the WEED scheme. However, wetlands in the equatorial latitudes are usually below the huge treetops, which might be another issue that contributes to the discrepancy between model and observation, since satellites misinterpret wetlands for forest. Nevertheless, the JSB-ESA simulation with prescribed boundaries managed to reduce overestimated wetlands in the tropics by accumulating excess water in the terrestrial water storage. In general, JSBACH simulations with wetland extend dynamics scheme introduce physically consistent changes into the model. However, there are no significant improvements in annual cycles of evapotranspiration, indicating that problems are probably due to parametrization of evapotranspiration in JSBACH (in addition and especially its calculation using forcing data). In Phase 1, it was pointed out that JSBACH coupled with atmosphere component ECHAM6, yields a better seasonal cycle of ET than the offline JSBACH forced by WFDEI. In general this analysis shows some impact of the WEED scheme implementation on JSBACH simulations. However, some processes are still poorly represent or missing, such as lateral flow, and consistency between surface albedo and heat capacity. Improvement and update of the WEED scheme is planned for the next stage. Though the ESA LC\_CCI WB product fits quite well into the range of uncertainty of available observations, several requirements have been recognized from the modelling perspective that might significantly improve quality of the data set:

- 1) Temporal information should be included on monthly time scale or finer and extend over longer periods (10 years or longer). Thus, information on climatology and trends can be derived ;
- 2) Flood events and flood plains seem to be lacking in existing products at some locations while simulated by several models. This could be due to corrupted observations for snow or vegetation cover regions (e.g. in the Amazon basin). Here, it needs to be verified and communicated whether such floodplains do not exist or just have not been detected by the satellite.

Additional valuable information that are not directly related to spatial mapping are:

- 1) Local time series of water depth with uncertainty information ;
- 2) Periods with frozen surface water bodies and the thickness of the frozen layer ;
- 3) Temperature time series in surface water bodies ;
- 4) Identification of the dominant surface water body type (lake/wetland/...) for a grid cell.

## 2.4 Revision and update of the cross-walking procedure for JSBACH

In the frame of the ESA LC\_CCI project, a new global LC data set was produced. LC is classified as one of Essential Climate Variables (ECV), and defined as the physical material at the surface of the earth (for example: trees, grass, bare soil, water). The ESA LC\_CCI product complies with the United

	Ref	LC CCI Climate Assessment Report v1		
	Issue	Page	Date	
	1.0	48	13.07.2015	

Nations Land Cover Classification Scheme (UN-LCCS). However, the UN-LCCS set of rules is not directly suitable for climate modelling. Therefore, the ESA LC\_CCI categorical classes need to be converted to model specific PFT distributions.

#### 2.4.1 ESA LC\_CCI product and lc-user-tool

In the frame of the cross-walking procedure from LC classes to PFTs, an evaluation and beta testing of the lc-user-tool (a software package developed by Brockmann Consult (BC) for manipulation of the ESA LC\_CCI data) was performed. For that purpose, two versions (June 2014 and August 2014) of the ESA LC\_CCI data have been tested. The LC data are available for three epochs: 2000, 2005 and 2010. Aggregations to a regular 0.5° resolution and a Gaussian T63 resolution (N48 grid corresponding approximately to 1.875° resolution) were performed.

The data for each epoch were cross-walked for the use with JSBACH (at T63 ~1.875° and 2° spatial resolutions) using the following steps:

- lc-user-tool is used to aggregate and convert LC classes into PFTs. Table 2-2 contains information on the cross-walking procedure. The first step of this conversion yields 10 vegetation types: Trees (Tr) and Shrubs (Sr) that can be Broadleaf Evergreen (BrEv), Broadleaf Deciduous (BrDe), Needleleaf Evergreen (NeEv), Needleleaf Deciduous (NeDe), and Grass that can be natural (NatGr) or managed (ManGr); 3 non-vegetated types: bare soils (BaSo), water bodies and wetlands (WB/WL), and snow-ice (SnoI);
- JSBACH currently supports 21 PFTs. However, in the standard configuration only 13 types distributed over 11 tiles (Table 2-3) are used. In this step, the 10 types from the previous step need to be converted into 13 JSBACH-PFTs. This process includes reducing of 4 tree types into 2 (evergreen and deciduous) types since the processes that will make use of distribution of needleleaf and broadleaf trees are still not implemented into JSBACH. The same applies for shrubs, with one exception. JSBACH in the recent version does not have implemented processes with evergreen shrub. Therefore, this type is treated as a raingreen shrub. Pasture and crops do not exist in the output of lc-user-tool. Therefore, additional maps and some educated guessing are applied to estimate the distribution of those types. The ratio between crops and pasture is kept the same as in the original JSBACH map and some unrealistic consequences of that assumption have been corrected. Pasture is generated from one third of managed grass and one third of natural grass. Crops are generated from two third of managed grass and the rest of two third of natural grass is treated as a grass in JSBACH. The non-vegetated type of polar ice caps is designated as glacier and ice, and is essentially the same in JSBACH as in the lc-user-tool output. Bare soil in JSBACH has an explicit treatment. Therefore this type is scaled to other tiles so that sum of all JSBACH PFT fractions adds to 1.
- In this step, we apply climatic and photosynthetic pathway rules. For that purpose, an updated world map of the Köppen-Geiger (K-G) climate classification adopted from [RD.24] is used. The photosynthetic pathway, i.e. the C4 vegetation percentage, is taken from International Satellite Land Surface Climatology Project (ISLSCP) Initiative II [RD.29] data. The rules are adopted from [RD.11] as follows: classes 1, 2, 3, 4, 6 are tropical, 5 and 7-28 are extra-

	Ref	LC CCI Climate Assessment Report v1		
	Issue	Page	Date	
	1.0	49	13.07.2015	

tropical classes. The polar classes 29 and 30 are not used here. Photosynthetic pathways larger than 50% are set to C4 and the rest to C3.

Some adaptations are needed in order that PFT maps correspond better with reality. C4 vegetation rarely appears in K-G 8-28 climate zones, thus C4 pasture for K-G classes 8-28 is converted into C3 grass. For the same reason, unrealistic distribution of C4 grass in K-G 8-28 zones is reassigned to be C3 grass. In the first approximation we treat evergreen shrubs as a raingreen shrub in JSBACH.

Table 2-2. Cross walking table for converting ESA-CCI-LC classes into JSBACH PFTs.

ID	color	LC CCI description	Tree			Shrub			Grass			Non-Vegetated			Total %		
			BrEv	BrDe	NeEv	NeDe	BrEv	BrDe	NeEv	NeDe	NatGr	ManGr	BasGr	WlWB		Snoi	NoBa
0		No data														100	100
10		Cropland, rainfed									100						100
11		Herbaceous cover								100							100
12		Tree or shrub cover					50			50							100
20		Cropland, irrigated or post-flooding								100							100
30		Mosaic cropland (>50% / natural vegetation (tree, shrub, herbaceous cover) (<50%)	5	5			5	5		15	60						100
40		Mosaic natural vegetation (tree, shrub, herbaceous cover) (>50%) / cropland (<50%)	5	5			7.5	10	7.5	25	40						100
50		Tree cover, broadleaved, evergreen, closed to open (>15%)	90				5	5									100
60		Tree cover, broadleaved, deciduous, closed to open (>15%)		70				15		15							100
61		Tree cover, broadleaved, deciduous, closed (>40%)		70				15		15							100
62		Tree cover, broadleaved, deciduous, open (15-40%)		30				25		35	10						100
70		Tree cover, broadleaved, evergreen, closed to open (>15%)			70			5	5	15							100
71		Tree cover, needleleaved, evergreen, closed (>40%)			70			5	5	15							100
72		Tree cover, needleleaved, evergreen, open (15-40%)			30			5	5	30							100
80		Tree cover, needleleaved, deciduous, closed to open (>15%)						70	5	5	15						100
81		Tree cover, needleleaved, deciduous, closed (>40%)						70	5	5	15						100
82		Tree cover, needleleaved, deciduous, open (15-40%)						30	5	5	30						100
90		Tree cover, mixed leaf type (broadleaved and needleleaved)	30	20	10	5	5	5	5	15	10						100
100		Mosaic tree and shrub (>50%) / herbaceous cover (<50%)	10	20	5	5	5	10	5	40							100
110		Mosaic herbaceous cover (>50%) / tree and shrub (<50%)	5	10	5			5	10	60							100
120		Shrubland						20	20	20	20						100
121		Shrubland evergreen						30		30							100
122		Shrubland deciduous							60								100
130		Grassland								60	40						100
140		Lichens and mosses								60	40						100
150		Sparse vegetation (tree, shrub, herbaceous cover) (<15%)	1	3	1		1	3	1	5	85						100
151		Sparse tree (<15%)	2	6	2					5	85						100
152		Sparse shrub (<15%)						2	6	2	5	85					100
153		Sparse herbaceous cover (<15%)								15	85						100
160		Tree cover, flooded, fresh or brakish water	30	30						20						20	100
170		Tree cover, flooded, saline water	60					20								20	100
180		Shrub or herbaceous cover, flooded, fresh/saline/brakish water	5	10				10	5	40						30	100
190		Urban areas								15	75					5	100
200		Bare areas									100						100
201		Consolidated bare areas									100						100
202		Unconsolidated bare areas									100						100
210		Water bodies													100		100
220		Permanent snow and ice														100	100

	Ref	LC CCI Climate Assessment Report v1		
	Issue	Page	Date	
	1.0	51	13.07.2015	

Table 2-3. PFT types used in JSBACH. Tile column indicates types used in this study and their distribution, while ID column indicate so far implemented types into JSBACH.

Tile#	ID	Cover Type Name
1	1	Glaciers
1	2	Tropical evergreen trees
2	3	Tropical deciduous trees
3	4	Extra-tropical evergreen trees
4	5	Extra-tropical deciduous trees
	6	Temperate broadleaf evergreen trees
	7	Temperate broadleaf deciduous trees
	8	Coniferous evergreen trees
	9	Coniferous deciduous trees
5	10	Raingreen shrubs
6	11	Deciduous shrubs
7	12	C3 grass
8	13	C4 grass
	14	Pasture
9	15	C3 pasture
10	16	C4 pasture
	17	Tundra
	18	Swamp
	19	Crops
11	20	C3 crop
11	21	C4 crop

Figure 2-6 shows the main properties of the new PFT distributions. There are less trees (33% Tropical Evergreen (TrET), 47% TrTD (Tropical Deciduous), 47% Extra-Tropical Evergreen (ExET), and 20% Extra-Tropical Deciduous (ExDT)) and more herbaceous types (more grass (C3Gr and C4Gr), less pasture (C3Pa and C4Pa), similar crops (C3Cr and C4Cr)). Deciduous shrubs (DeSh) were almost nonexistent in the reference JSBACH distributions and raingreen shrubs (RgSh) has similar amount as the reference JSBACH PFT distribution.

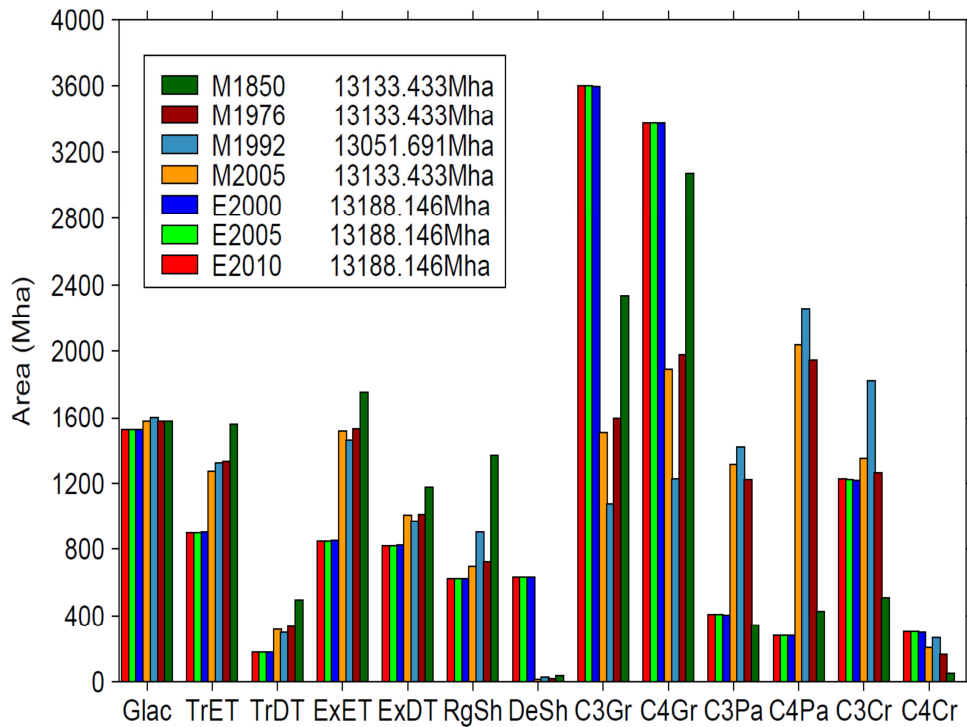


Figure 2-6. Total area of JSBACH PFTs for various epochs. E2000, E2005 and E2010 are for PFT maps derived from the various ESA-CCI-LC epochs. The others are JSBACH reference maps representing various years in time.

Figure 2-7 shows new global PFT distribution and Figure 2-8 the difference with the reference distribution. These two figures summarize the geospatial differences between the default JSBACH PFT distributions and newly derived from the ESA LC\_CCI products. The most striking differences appear in herbaceous types, especially C3 and C4 grasses, and extra tropical evergreen forest in the northern latitudes.

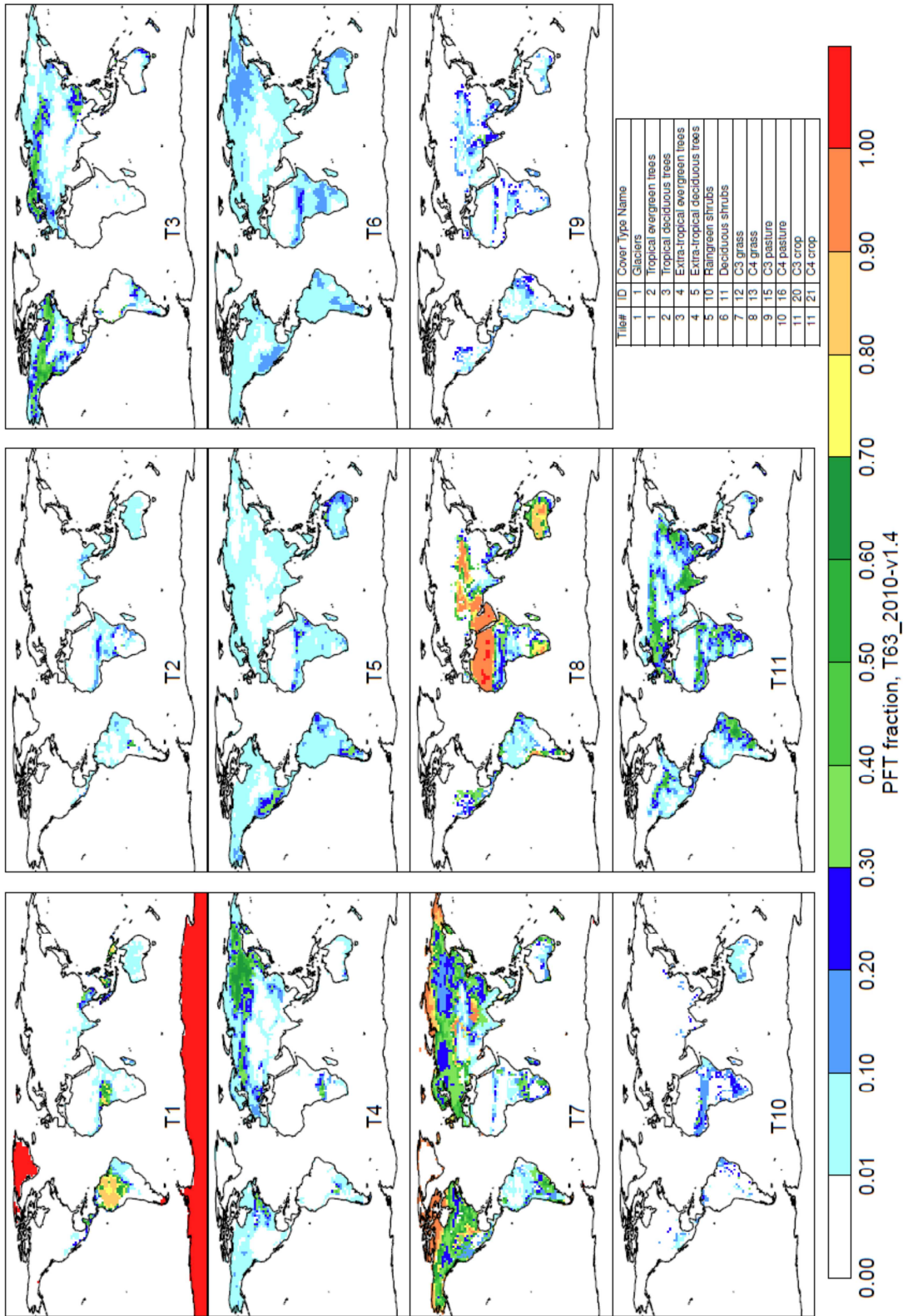


Figure 2-7. PFT fractions of ESA-CCI-LC map for the 2010 epoch.

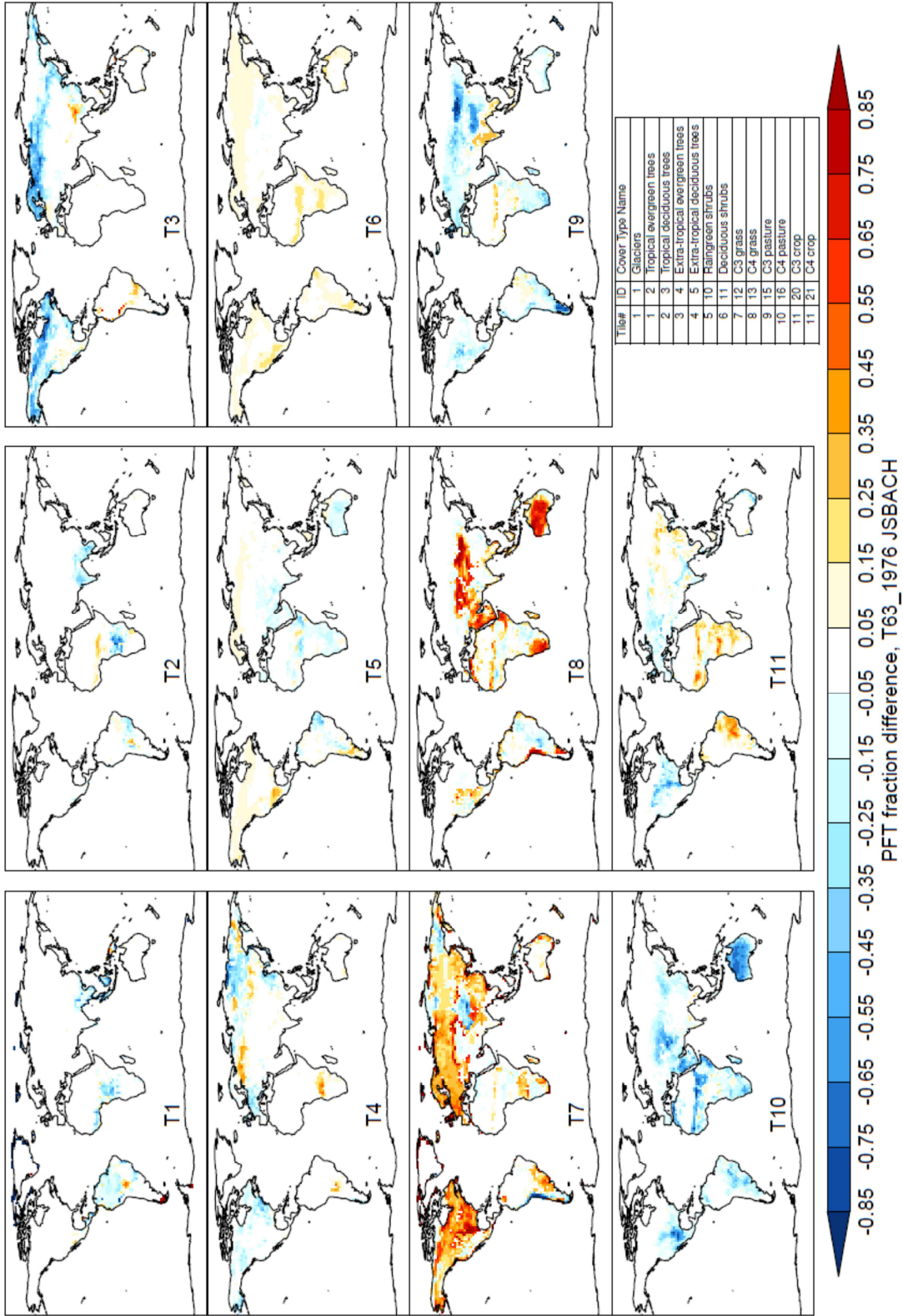


Figure 2-8. PFT fraction differences between ESA-CCI-LC and JSBACH reference map.

	Ref	LC CCI Climate Assessment Report v1		
	Issue	Page	Date	
	1.0	55	13.07.2015	

## 2.4.2 JSBACH offline simulations

Two JSBACH simulations driven by WFDEI data were performed at T63 resolution. The simulation with default JSBACH PFT distributions is labelled MPI and ESA is the simulation with PFTs derived from the CCI\_LC maps. These simulations are evaluated for the 1981-2010 period. Sensitivities of the hydrological, energy and carbon cycles are investigated. The following variables are compared between simulations with the new LC\_CCI and the old reference PFT distributions: (i) evapotranspiration and runoff as an indicator of changes in hydrological cycle, (ii) temperature and albedo as an indicator for changes in the energy cycle and (iii) GPP as an indicator of carbon cycle sensitivity.

## 2.4.3 Results

Less evergreen trees in northern extra-tropical latitudes (Figure 2-8, T3) leads to an increased annual mean albedo (Figure 2-9) and decreased evapotranspiration (Figure 2-9). Net effect is cooling up to 0.5 K at those latitudes (Figure 2-9). In South America, probably an increase in extra-tropical trees (Figure 2-8, T3 and T4) results in a decrease in albedo (Figure 2-9). However, similar as for the other regions of the world, the net effect on surface temperature depends on regional factors. Due to the global decrease of trees, GPP is also decreased globally but there is also slight increase in certain regions of the world (Figure 2-9).

The hydrological cycle is investigated in more detail for the world's major river basins (Murray, Parana, Amazon, Mississippi, Mackenzie, Congo, Niger, Nile, Ganges/Brahmaputra, Yangtze and Danube). Annual mean biases of evapotranspiration and runoff show a small decrease for the majority of the river basins except for Niger, Nile and Yangtze (Figure 2-10). Both model simulations show similar annual cycles of evapotranspiration which is in good agreement with Land-FLUX observation for some basins especially in the late summer and the autumn (Danube, Mackenzie, Mississippi and Lena). Annual cycles of evapotranspiration are shown for Danube and Congo River basins in Figure 2-11. An interesting feature is shown for the Congo River basin in which both simulations differ from each other, which is caused by larger differences in the PFT distributions. Here, LC\_CCI derived PFT distributions have 35% less tropical evergreen trees and tropical deciduous trees are reduced by more than 50% in comparison to the reference PFT distribution. Therefore, this change in evapotranspiration might be due to deforestation in the basin that was not included in the JSBACH reference data. The annual cycle of albedo from the LC\_CCI simulation (Figure 2-12) shows better agreement with some satellite observations (GLOBALBEDO-DHR and GLOBALBEDO-BHR).

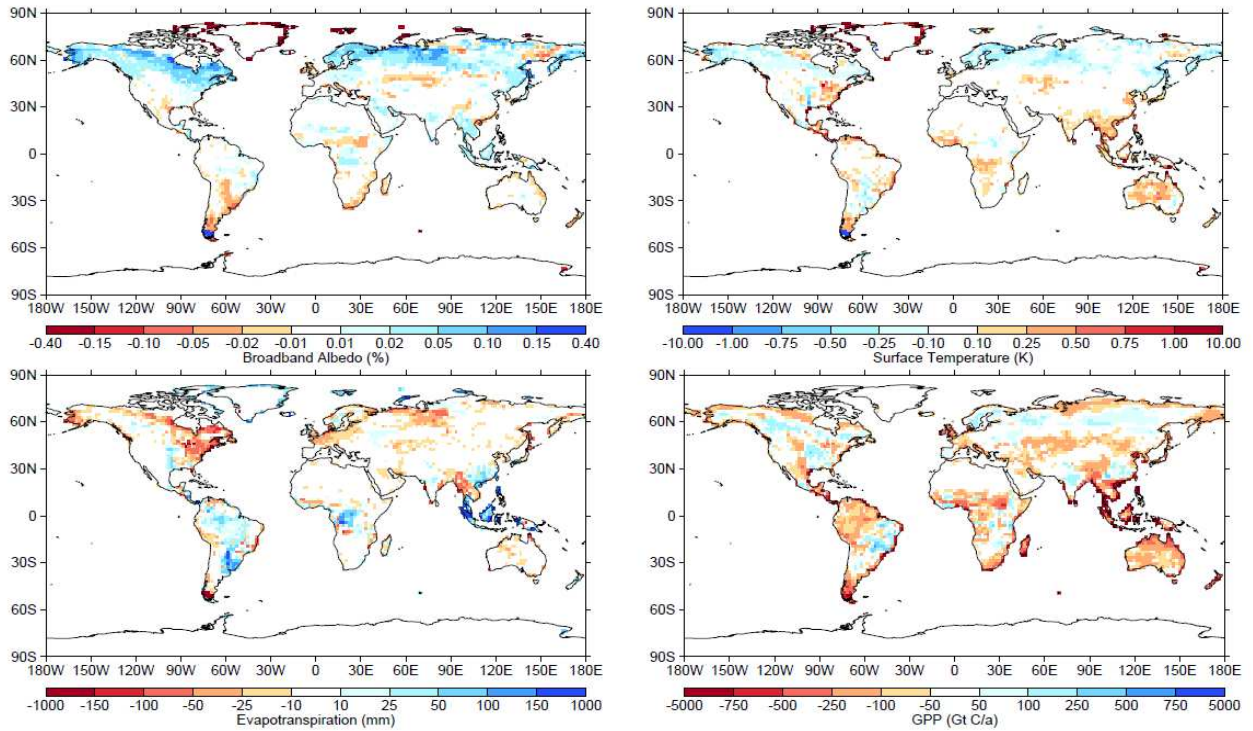


Figure 2-9. Spatial differences between ESA (PFT distributions derived from ESA-CCI-LC) and MPI (default JSBACH PFT distributions) simulations: broadband albedo, surface temperature, evapotranspiration and GPP.

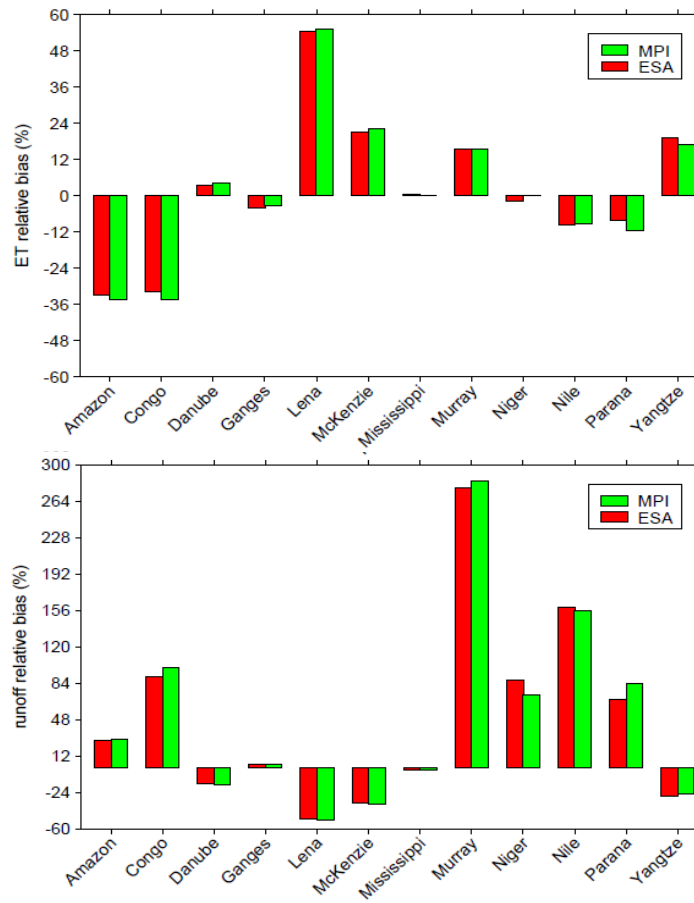


Figure 2-10. Relative annual mean biases for the major river basins of the world: evapotranspiration (top) and runoff (bottom).

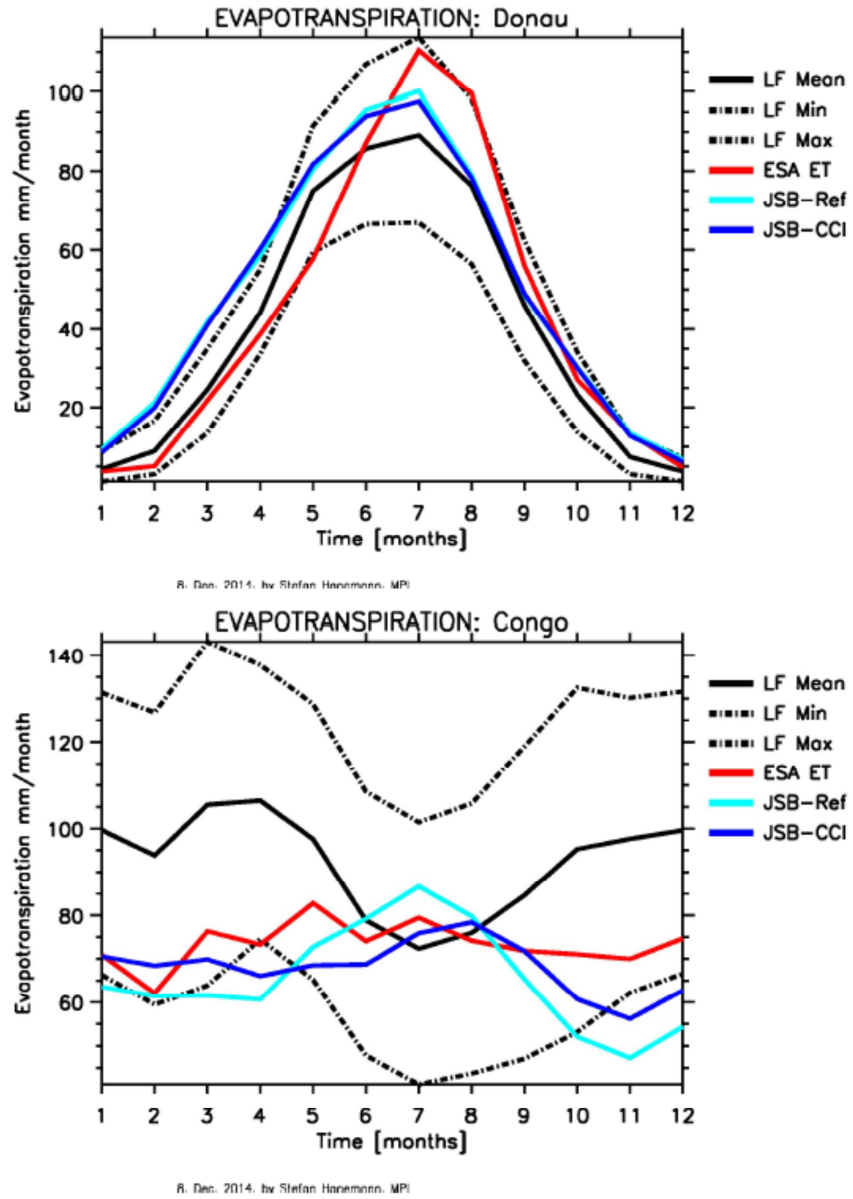


Figure 2-11. Annual cycle of evapotranspiration for Danube (top) and Congo (bottom) river basins

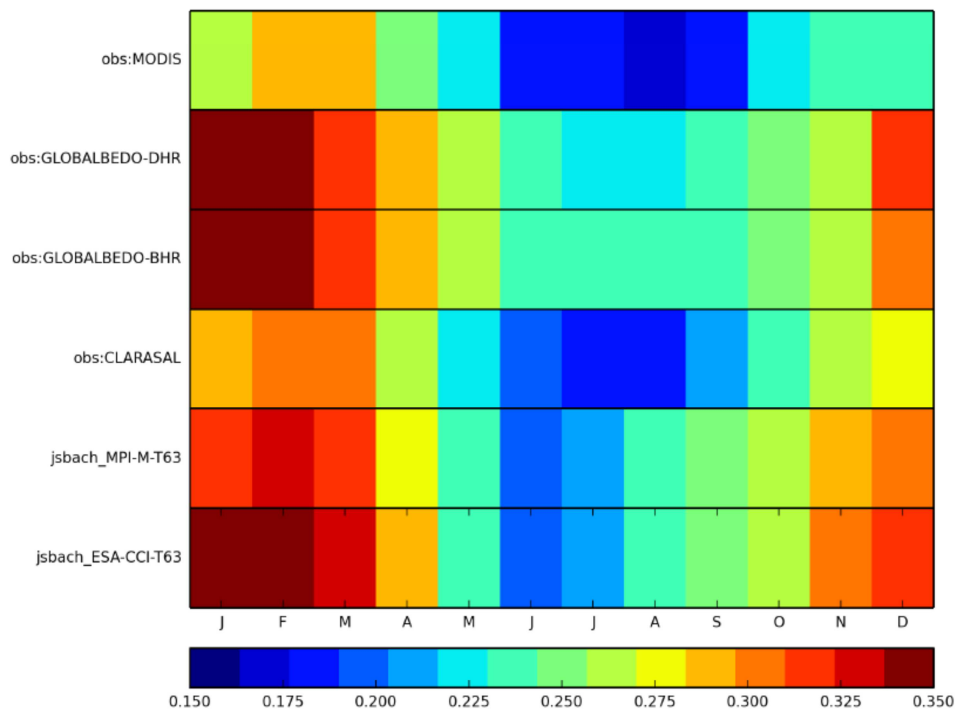


Figure 2-12. Albedo seasonal cycle

#### 2.4.4 Conclusions and outlook

Since Phase I of the project, JSBACH has gone through several revisions and updates. The most notable one being the introduction of a new five layer soil hydrology scheme in which not only the root zone is differentiated into several layers, but also layers below are added [RD.21]. There were also updates of ESA LC\_CCI data and some improvements in the cross-walking method including the further development of the lc-user-tool. Similar as in Phase I, there are some differences between the reference and ESA LC\_CCI simulations but first results do not show huge impact of the new PFT distributions on the simulations. However, there are still some features that can be improved or implemented into the current CCI\_LC maps and/or cross-walking procedure. The biggest source of inconsistency between LC data and PFT distribution currently implemented into JSBACH comes from the lack of information about pasture and crops, i.e. there is no clear guidance on how to convert natural and managed grass into crops, pasture and grass. Similar is the case with shrubs phenotypes. Currently, JSBACH distinguishes between evergreen, raingreen and summergreen shrub types, while the LC\_CCI maps provide information about evergreen and deciduous shrubs distribution. These issues are recognized as a first priority in order to improve consistency and conversion of the LC\_CCI map into JSBACH PFT distribution. Other nice features will be to have delineation of climate zones and distinction between C3 and C4 photosynthetic pathways.

	Ref	LC CCI Climate Assessment Report v1		
	Issue	Page	Date	
	1.0	60	13.07.2015	

## 2.5 Diversification of albedo into vegetation and soil fraction

In order to calculate albedo of the snow-free land in JSBACH, the background albedo needs to be separated into vegetation and soil part. For the current version of the JSBACH maps of background albedo (visible and Near Infrared (NIR) bands) have been derived from MODIS data. This leads to an inconsistency with the PFT distribution derived from the ESA LC\_CCI data, therefore we were exploring possibilities how to separate background albedo from GLOBALBEDO dataset into vegetation and soil fraction. Ideal for this exercise would be to have at least a couple of years with a monthly time series of vegetation fraction which is consistent with the GLOBALBEDO data set and to apply multiple linear regressions. Additionally, the snow seasonality product for the same period is needed. However, since vegetation fraction is available only as an annual average for 5 years epochs, NDVI seasonality product is used as a proxy for vegetation fraction, but first results turned out to be unrealistic. There are several reasons, for which that might be or any combination of them:

- 1) Inconsistency between the GLOBALBEDO dataset and the NDVI seasonality product;
- 2) Too short period of availability of the NDVI seasonality product;
- 3) NDVI does not seem to be a proper proxy for vegetation fraction;
- 4) Linear regression may not be a proper model for relationship between NDVI and albedo.

Separation of background albedo into soil and vegetation fraction is recognized as the highest priority task in order to assure consistency between albedo scheme and PFT distribution in JSBACH.

	Ref	LC CCI Climate Assessment Report v1		
	Issue	Page	Date	
	1.0	61	13.07.2015	

## 3 USING THE LAND COVER CCI PRODUCTS TO ASSESS PHENOLOGY AND LAND COVER TRANSITIONS (*LSCE*)

### 3.1 Using the NDVI seasonality product to evaluate phenology in the Orchidee Land Surface Model

#### 3.1.1 Introduction

The aim of this work was to investigate how the NDVI seasonality product produced by the LC\_CCI project can help to evaluate and improve the phenology of the ORCHIDEE Terrestrial Biosphere Model (TBM). Leaf phenology, the timing of leaf onset, growth and senescence, is a critical component of the coupled soil-vegetation-atmosphere system as it directly controls the seasonal exchanges of carbon, C, as well as affecting the surface energy balance and hydrology through changing albedo, surface roughness, soil moisture and evapotranspiration. In order to make realistic predictions of interactions between vegetation and the carbon, water and energy cycles it is crucial to account for these feedbacks in TBMs through prognostic leaf phenology schemes [RD.32, RD.35]. Model evaluation studies have shown that there are biases in the growing season length, magnitude of the Leaf Area Index (LAI) and uncertainty in the inter-annual variability predicted by TBMs when compared to ground-based observations of leaf emergence and LAI [RD.33, RD.38] or satellite-derived measures of vegetation greenness and LAI [RD.34, RD.37]. As expected, incorrect representations of the timing of leaf onset and senescence, as well as the rate of leaf growth and fall, results in inaccurate model predictions of the seasonal carbon, water and energy exchange.

The objective of a recent study by [RD.36] was to investigate whether biases in LAI simulations were the result of inaccurate parameters in the model or an incorrect structural representation of phenology. In order to test this, they performed an optimisation of the phenology-related parameters in the ORCHIDEE TBM using satellite-derived NDVI from the MODIS instrument. The MODIS data were used as they are widely available to download online. However the prior (reference) simulation and posterior (optimised) simulations need to be compared to independent datasets. In this study therefore, we use the LC\_CCI NDVI seasonality product to evaluate the optimised ORCHIDEE phenology simulations.

In addition, [RD.36] raised questions about how best to perform the optimisation of such models. Currently, different phenology models are assigned to different PFTs in ORCHIDEE, therefore the parameters are optimised for each PFT independently. However, the optimisations did not work well for some PFTs, and others, such as natural C3 grasses, span a wide range of climate types. Thus [RD.36] suggested optimising by PFT may not be the best approach and that parameters may be better

	Ref	LC CCI Climate Assessment Report v1		
	Issue	Page	Date	
	1.0	62	13.07.2015	

grouped according to different climate types. One way to examine the behaviour of different vegetation types at global scales is to examine the distribution of phenology metrics depending on how those vegetation types are grouped. In this instance, phenology metrics refer to the Start of Season (SOS) and End of Season (EOS) dates that give the time of leaf onset and senescence. These metrics can be calculated from the data. Although [RD.36] use the full daily NDVI time series to optimise the phenology-related parameters of the model, essentially the aim was to improve the predictions of the SOS and EOS. Comparing the distribution of SOS and EOS dates grouped by PFT, land cover type or climate type can give us an idea whether the PFT-dependent parameterisation is the best approach.

### 3.1.2 Methods

Firstly the NDVI seasonality product was aggregated to the model grid cell resolution of  $0.72^\circ$  using the aggregation tool provided by the LC\_CCI project.

Two issues arose when considering using the NDVI seasonality product to evaluate the model phenology. Firstly, as only the Mean Seasonal Cycle (MSC) of the complete NDVI time series is provided per pixel, an evaluation of the full model time series cannot be performed. Secondly and in relation to the first issue, the model does not simulate NDVI; instead it calculates the fraction of Absorbed Photosynthetically Active Radiation (fAPAR) as a function of the LAI. The fAPAR is linearly related to NDVI thus we can compare the model fAPAR and NDVI by normalising the both to their maximum and minimum values. The simulated fAPAR have already been normalised to their maximum and minimum values based on the whole time series, but we cannot do the same for the NDVI seasonality product as we only have the MSC.

Thus in this study, we do compare the MSC of both the model and the data, but we do not expect their magnitudes to be similar. However we can still see if the overall phase (timing) of MSC is better captured by the optimised model. The MSC was compared to the NDVI seasonality at global scale and for the following latitudinal regions boreal ( $60-90^\circ$ ), temperate ( $30-60^\circ$ ) and tropical ( $0-30^\circ$ ) regions north and south of the equator (where relevant).

As we cannot directly evaluate the magnitude of the model fAPAR, instead we evaluate the month in which the model reaches the maximum fAPAR compared to the month in which the NDVI is at its maximum value. Lastly, we calculate the SOS and EOS dates for each grid cell. These are defined as the point in the time series where the fAPAR or NDVI are half the value of the annual amplitude. Pixels with two seasonal cycles are ignored. Again, as we are looking at the MSC, these are mean values. In all of the abovementioned analyses, both the prior and posterior model simulations are compared with the LC\_CCI NDVI seasonality product.

Finally, in order to investigate the secondary objective of this work, the SOS and EOS dates that were calculated for each  $0.72^\circ$  grid cell are grouped according both PFT and then climate type. The K-G climate classification of [RD.24] was used for this purpose. However, there are  $\sim 30$  climate classes in the original classification. TBMs typically group their vegetation classes into larger units, focusing on tropical, temperate and boreal biomes. Here we follow the methodology of [RD.11] for grouping the K-G classes into 5 super classes: tropical, temperate warm, temperate cold, boreal warm and boreal cold. The distributions per PFT and per biome are then compared, in order to test the hypothesis that

some parameters of the model should be optimised per biome and not per PFT, as was done in [RD.36].

### 3.1.3 Results

#### *Evaluating the optimized phenology in ORCHIDEE*

Figure 3-1 clearly shows that the optimisation has improved the timing mean seasonal cycle of the model fAPAR when compared to the LC\_CCI NDVI in the northern hemisphere, especially with regard to the end of the growing season. Indeed, the main result of the optimisations was that the end of the growing season started much earlier after optimisation, as a result of an increase in the temperature threshold needed for senescence to occur [RD.36]. Although the full time series of the LC\_CCI NDVI data need to be normalised in order to more directly compare the overall magnitude of the seasonal cycle, it is certainly promising that the optimised model compares more favourably with an independent dataset. In future, we aim to discuss performing a more extensive evaluation of the ORCHIDEE phenology with the full time series of data in collaboration with the LC\_CCI team.

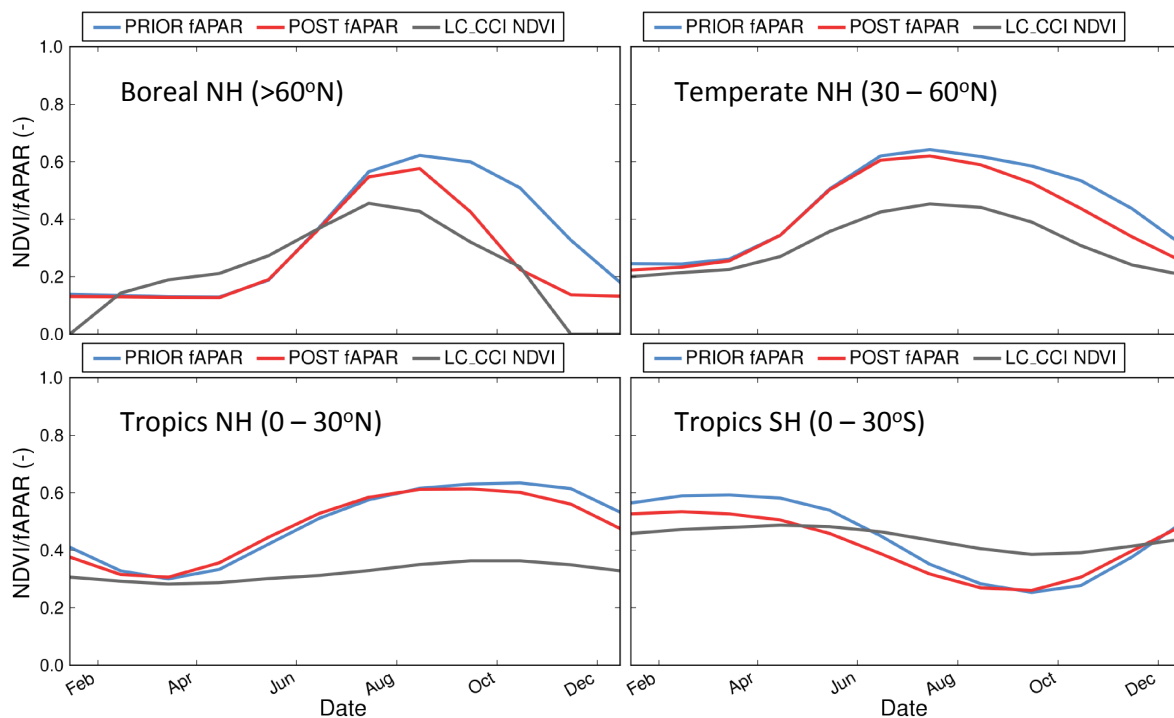


Figure 3-1. Plots showing the mean seasonal cycle for the modelled fAPAR (prior = blue; posterior = red) and LC CCI NDVI (grey) for 4 regions (boreal, temperate and tropical northern hemisphere (NH) and the tropical region in the southern hemisphere (SH)).

Figure 3-2 shows the mean SOS dates calculated from the model and the LC\_CCI NDVI seasonality product. The prior map shows the model simulation with the default parameter values (Figure 3-2a), and the posterior map shows the simulation after the optimisation (Figure 3-2b). The difference between the two is shown in Figure 3-2c. The optimisation has resulted in an earlier start of the season

by ~30 days for much of the northern hemisphere and the dry tropical regions in the southern hemisphere. This has not changed the spatial patterns considerably in the northern hemisphere with respect to the LC\_CCI product (Figure 3-2d). However, the predicted SOS dates along the southern limit of the Sahelian region better match the LC\_CCI product, as does the savannah region south of the Central African Rainforest. Areas that still require improvement include central South America and central Australia.

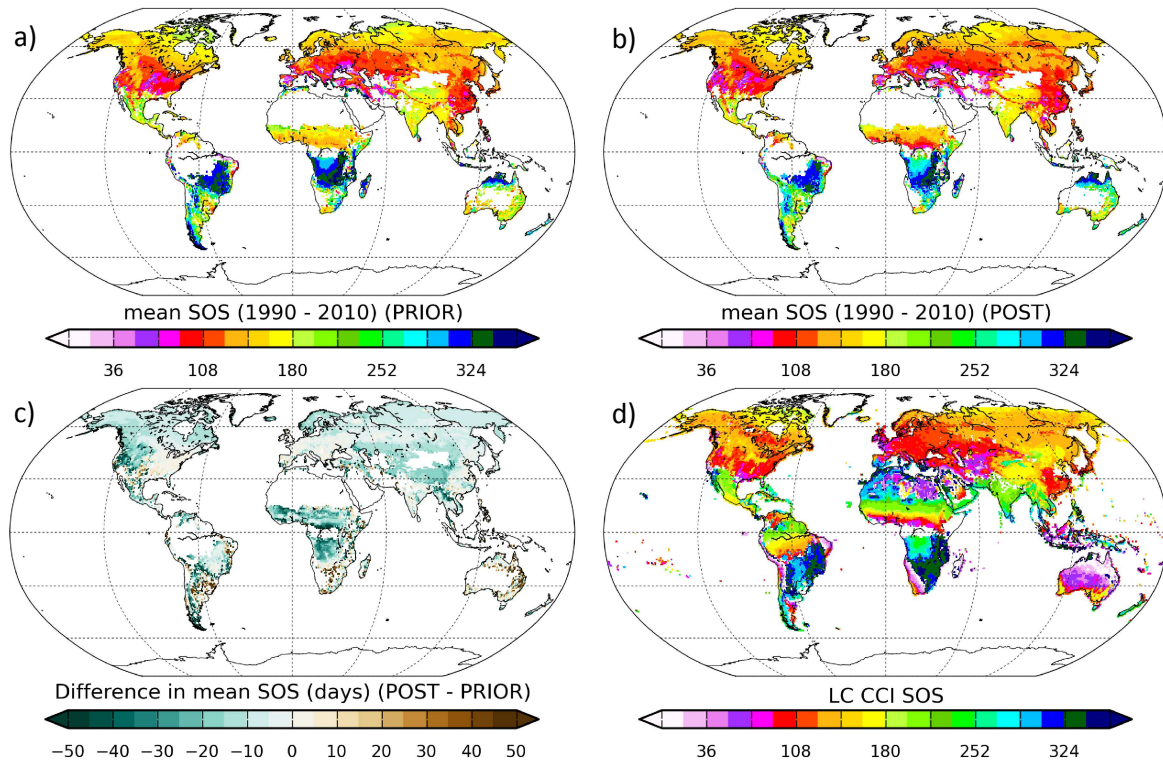


Figure 3-2. Global maps showing the modelled prior and posterior SOS dates (a, b) and their difference (c) compared to those derived from the LC CCI product (d).

Figure 3-3 shows the same maps as Figure 3-2 but for the EOS dates. As seen in Figure 3-1, the most dramatic impact of the optimisation was the dramatic reduction in growing season length caused by the earlier start to leaf senescence of ~100 days (Figure 3-3b,c) across the northern hemisphere; only the Sahelian region and the drylands of southern USA experience a later onset of leaf fall after the optimisation (Figure 3-3c). When compared to the independent LC\_CCI product, we can see that the optimisation has resulted in a dramatic improvement in the predicted end of the growing season across the northern hemisphere and Sahelian region. Evergreen regions were not included in this model analysis as they do not have specific phenology models in the ORCHIDEE TBM.

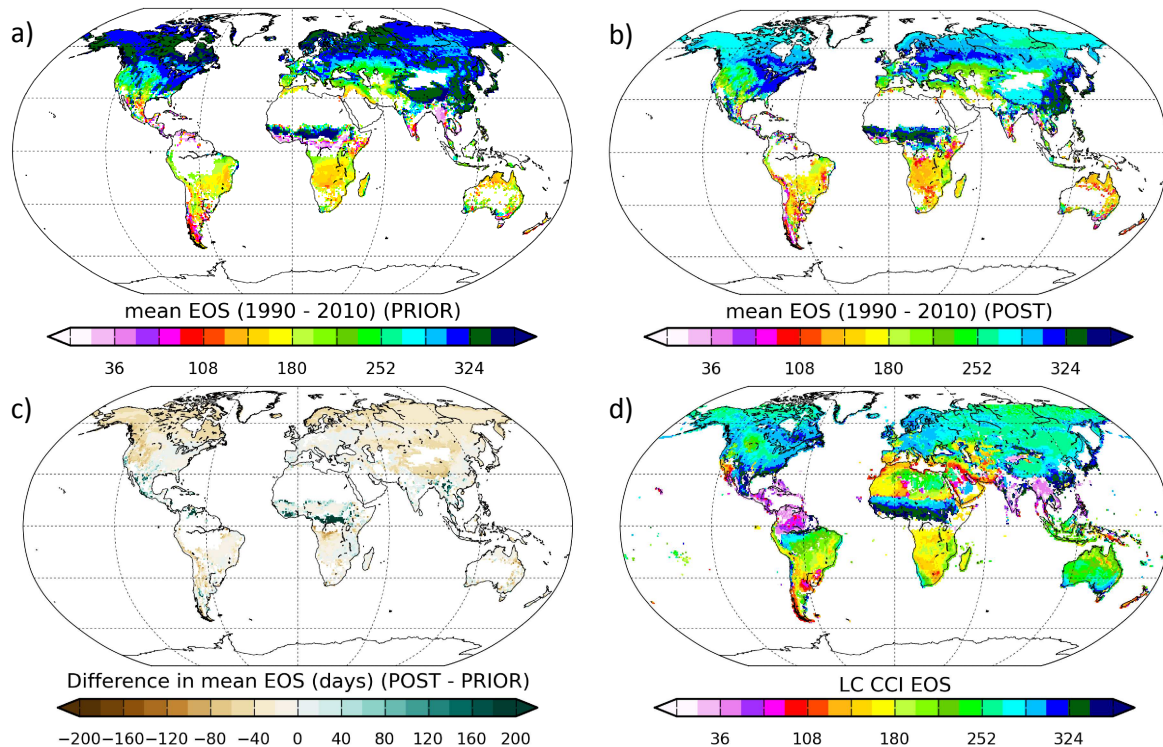


Figure 3-3. Global maps showing the modelled prior and posterior EOS dates (a, b) and their difference (c) compared to those derived from the LC CCI product (d).

One issue with this analysis is that the mean SOS and EOS dates of the ORCHIDEE model were derived for a different time period than for the LC\_CCI data. Another is that the SOS and EOS dates for the LC\_CCI product were calculated on the basis of the weekly data provided in the NDVI seasonality, and not daily data as were used for the ORCHIDEE calculations. This means that the SOS and EOS dates derived from the LC\_CCI product are more uncertain than if daily data could be used. Still, the global maps presented here still show that at large scale the data can be used for an evaluation and that the ORCHIDEE model performs better after optimisation.

### *Evaluating the global distribution of SOS and EOS dates per PFT and per biome*

The aim of this work was to investigate whether the SOS and EOS dates derived at global scale are more tightly distributed when grouping by climate type rather than by PFT. In current generation TBMs, the parameters are generally defined based on PFTs and not on any other grouping. [RD.36] suggested that some parameters might be better defined on the basis of species or underlying climate or environmental conditions. Since the objective is to improve the phenology models, which simulate the start of leaf onset and senescence, we can start by examining SOS and EOS dates derived from data, in order to investigate the above hypothesis.

Figure 3-4 to Figure 3-6 show the distributions of SOS and EOS date per PFT and per climate biome for tropical, temperate and boreal biomes, respectively. Most forest PFTs in ORCHIDEE are designated as tropical, temperate and boreal, and therefore are compared to the distribution by that specific biome type. Figure 3-4 shows that the distribution across the tropical PFTs is similar to the case where the pixels are grouped based on the tropical biome type. There is wide range of values in all cases, likely related to the fact that these are generally water-limited environments that exist within different precipitation regimes. Thus the parameters of the model may need to be optimised and defined at regional or species level, rather than at large scales of PFTs or biomes.

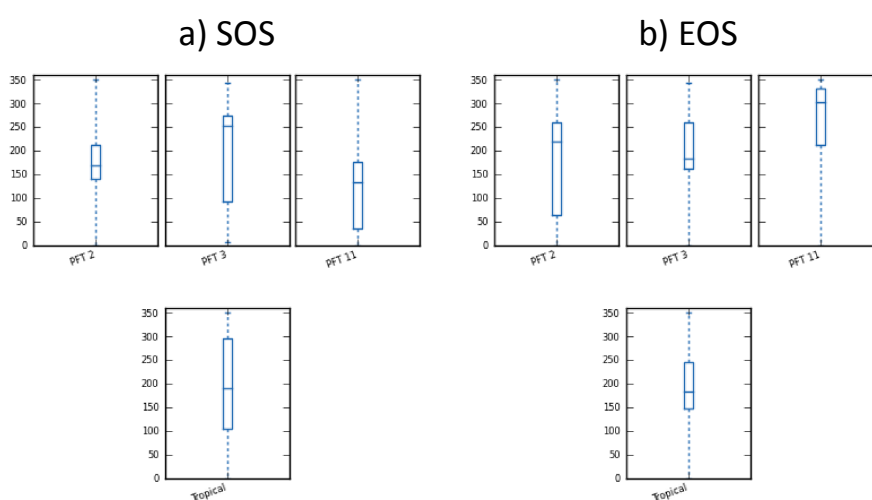


Figure 3-4. Box and whisker plots showing the distributions of SOS (a) and EOS (b) dates per PFT (top panel) and by climate type (bottom panel) for Tropical regions. PFT 2, 3 and 11 are defined as tropical PFTs in the ORCHIDEE TBM.

Contrary to the tropical regions, the distributions for temperate and tropical PFTs are all smaller than if the grid cells were grouped by climate type, which is the opposite of the hypothesis presented above, except for PFT 5 (Figure 3-5). The reason for this could be related to the fact that PFT5 (temperate broadleaved evergreen PFT) encompasses species that exist both in Europe and in south-eastern Australia, and the northern and southern hemispheres are approximately 6 months out of phase in their growing seasons.

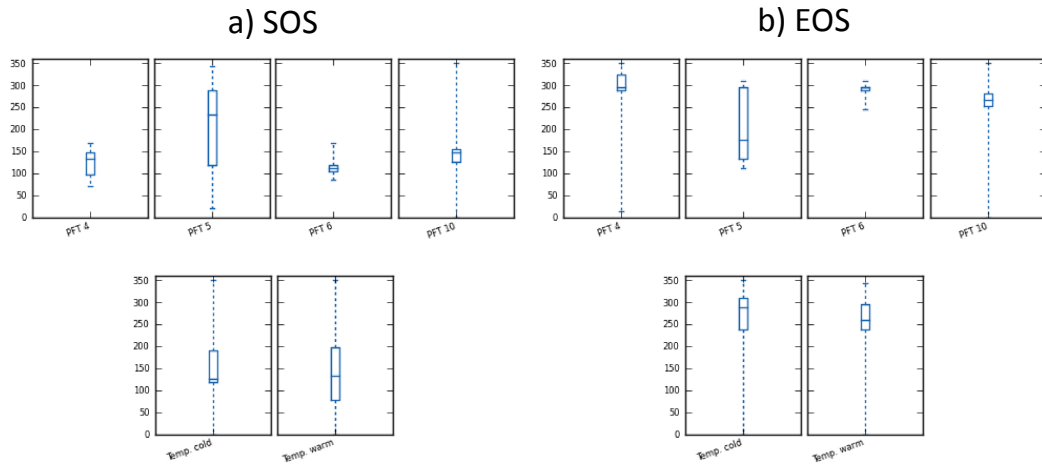


Figure 3-5. Box and whisker plots showing the distributions of SOS (a) and EOS (b) dates per PFT (top panel) and by climate type (bottom panel) for Temperate regions. PFT 4 – 6 are defined as temperate forest PFTs in the ORCHIDEE TBM, and PFT 10 is natural C3 grass which is found in temperate and boreal regions. The bottom panel shows the distribution for both temperate warm and cold regions as defined by the K-G classification and following [RD.11].

This is a surprising result, especially in the case of natural C3 grasses (PFT10) that are widely distributed across the globe. Clearly for vegetation types with phenology that is mostly driven by temperature or daylength, and not moisture availability, the underlying physiology and structural differences between the PFTs are important, and thus grouping parameters on the basis of PFTs is justified in this instance.

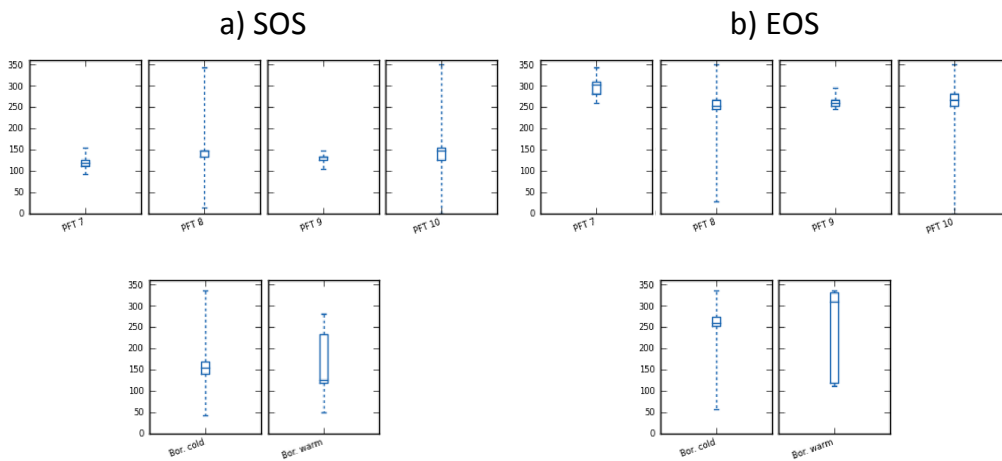


Figure 3-6. Box and whisker plots showing the distributions of SOS (a) and EOS (b) dates per PFT (top panel) and by climate type (bottom panel) for Boreal regions. PFT 7 – 9 are defined as boreal forest PFTs in the ORCHIDEE TBM, and PFT 10 is natural C3 grass which is found in temperate and boreal regions. The bottom panel shows the distribution for both boreal warm and cold regions as defined by the K-G classification and following Poulter et al. (2011).

	Ref	LC CCI Climate Assessment Report v1		
	Issue	Page	Date	
	1.0	68	13.07.2015	

However, the analysis could be taken to the next step by calculating the underlying phenology parameters on the basis of the SOS and EOS dates calculated here. This has not been done yet because the SOS and EOS dates derived from the LC CCI product were based on weekly data based on the mean seasonal cycle, and not on the full time series. However, a more complete investigation could take place in the future in collaboration with the LC CCI data providers.

### 3.1.4 Discussion and Conclusion

The results presented here represent a very preliminary analysis to illustrate how the LC\_CCI NDVI seasonality product can be used to evaluate and improve the phenology models in the ORCHIDEE TBM. It is crucial to validate the results of an optimisation with an independent dataset, and the LC\_CCI product has allowed us to do that. This shows that these data are also valuable to land surface modellers for model evaluation, rather than just using the land cover maps to drive the simulations. We have shown that the optimisation of the ORCHIDEE phenology has resulted in a better match in the timing of the mean seasonal cycle of the model for northern hemisphere regions when compared to the LC\_CCI data, as well as a marked improvement in the predicted EOS dates.

However, several issues arose when performing the analysis, which limited the extent to which we could use the LC\_CCI data. Firstly, the SOS and EOS dates would ideally be calculated using daily data to improve the accuracy of the derived dates, as leaf onset and senescence can take place quite rapidly for some vegetation types. Secondly, only having access to the mean seasonal cycle limited the analysis we could perform. Ideally, the full NDVI time series would be used. This would also enable the modellers to compare the model and data from the same time period. Finally, and in relation to the last point, in order to compare with modelled fAPAR, we need to normalise the model simulations and the NDVI data. This cannot be achieved when only the mean seasonal cycle is provided.

Furthermore, the major questions related to the vegetation seasonal cycle in the context of climate change are the trends and inter-annual variability in the phenology-related metrics such as SOS and EOS. This type of analysis cannot be performed without the full time series. There are currently only a few long time series of NDVI available to the public. The NDVI record used in the LC\_CCI project therefore represents a valuable added product that could be widely used for the type of analysis presented and discussed here. We therefore suggest to the LC\_CCI project team that they consider calculating phenology related metrics for each year and releasing this as a “seasonality product” with the CCI project. Or that they consider releasing the full time series, although we appreciate this would be a considerable effort.

## 3.2 Assessing land cover transitions

### 3.2.1 Introduction

Land Use change is thought to be an important contributor to the total anthropogenic emissions of CO<sub>2</sub>, second only to emissions from fossil fuel burning. Therefore, this process must be accounted for in earth system model simulations. Current estimates of land use change emissions based on FAO data [RD.40] are  $0.9 \pm 0.8 \text{ PgC yr}^{-1}$  during the past decade [RD.39]. However this estimate is still

	Ref	LC CCI Climate Assessment Report v1		
	Issue	Page	Date	
	1.0	69	13.07.2015	

uncertain. Given its importance understanding the impact of anthropogenic changes to the biosphere, further quantification and evaluation of the current estimates are needed. [RD.41] have recently contributed to this effort by publishing estimates based on 30m resolution Landsat data. The new state-of-the-art land cover maps produced in the LC\_CCI project can significantly aid in this regard. As deforestation is the primary source of land use change emissions, the aim of this work was to calculate the forest transitions between the three epoch maps (2000, 2005 and 2010) and to compare these estimates with those produced by [RD.41] and the FAO [RD.40].

### 3.2.2 Methods

In order to calculate the initial forest area in 2000, the LC classes were converted into the 13 PFTs used in LSMs using the “cross-walking” table defined in Phase 1 of the LC\_CCI project and described in [RD.12]. The transitions between the PFTs were then calculated in the following steps:

- i) The LC maps between the different epochs were compared to determine which classes had changed;
- ii) The possible transitions between the LC classes were then calculated (e.g. Forest to Grass (F to G) or Crop to Forest (C to F), etc.
- iii) The transitions in the LC classes were translated into the PFTs as described above.

### 3.2.3 Results

This section presents the main results at global scale of the LC transition study. A more detailed description of the results, including LC transitions per region and country, will be provided in [RD.42], which will be submitted to an EGU journal in June 2015 and will include partners from the LC\_CCI project.

The gross loss and gain in forest area at global scale between 2000 and 2010 was 172,171 and 9,844 km<sup>2</sup>, respectively. A gain in forest area was only found during the second period, from 2005 to 2010. The gross loss in forest area decreased from 144,482 km<sup>2</sup> during 2000-2005 to 27,689 km<sup>2</sup> during 2005-2010 [RD.42]. A similar trend of decreasing deforestation rate was also presented in FAO's report [RD.40]. Global maps of net forest loss using the LC\_CCI products are compared to those from [RD.41] study in Figure 3-7 [RD.42]. The gross forest loss and gain from 2000 to 2012 reported by [RD.41] are 2.3 and 0.8 million km<sup>2</sup>, respectively. Thus, the net global forest loss (1.5 million km<sup>2</sup>) is much higher than that from the ESA LC\_CCI product (0.16 million km<sup>2</sup>). The largest disagreements can be seen in the Northern Hemisphere high latitude regions of Canada and Siberia. In the tropical areas, the net forest loss is also much lower in the estimates derived from the ESA LC\_CCI product compared to [RD.41]. The reasons behind this are likely the high spatial resolution of Landsat [RD.41] and the multiple year integration of the ESA LC\_CCI maps. Although there is a strong difference between the absolute areas, the geographical distributions are roughly similar (Figure 3-7). The mutual hotspots of net forest loss are concentrated in South America, Middle Africa and Southeast Asia.

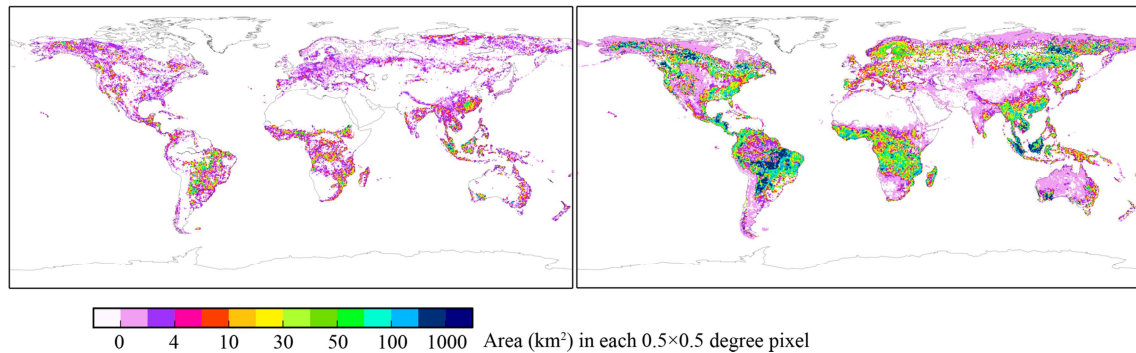


Figure 3-7. The net forest loss from 2000 to 2010 in the estimates of ESA (left) and the net forest loss from 2000 to 2012 in the estimates of Hansen et al. (2013) (right).

Transitions were observed between most major LC types but not pasture. Nine transitions were found for the 2000 to 2005 period, and twelve for the 2005 to 2010 period, although the total transition area is much lower in the 2<sup>nd</sup> period ~42,500km<sup>2</sup> compared to ~1,700,000km<sup>2</sup> [RD.42]. Figure 3-8 shows the transition matrix between all forest and all other land cover types globally. The majority of the transitions are related to conversion from forest to crops. During 2000-2005, the LC transitions with the largest area are forest to crop, forest to bare soil, and forest to shrubs, accounting for 50%, 17%, and 14%, respectively, of the total transition area (Figure 3-8, middle). During 2005-2010, the largest transitions are forest to crops and shrub to crop, representing 49% and 16% of the total, while the percentages of bare soil to crops, forest to shrub, and forest to grass are small but similar, ranging from 6% to 8% (Figure 3-8, middle) [RD.42].

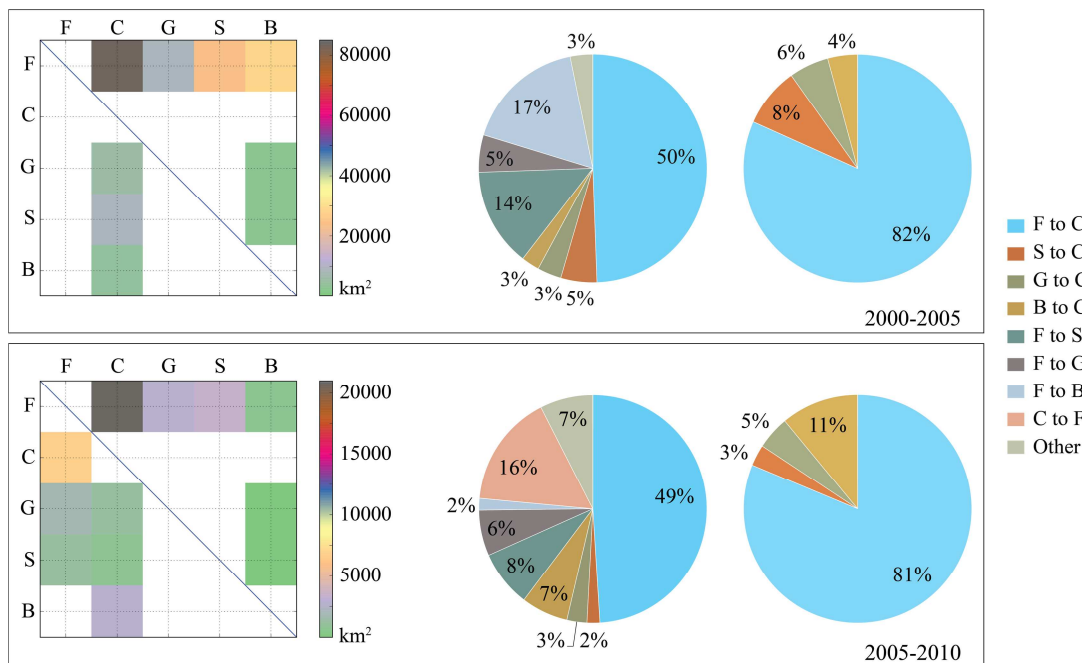


Figure 3-8. The global transition matrix (left), the global composition patterns of all transitions (middle), and the global composition patterns of crop gain (right) during 2000-2005 and during 2005-2010. In the matrix, the row names represent the sources of transitions, and the column names represent the gains. The colour represents the global area of each transition.

	Ref	LC CCI Climate Assessment Report v1		
	Issue	Page	Date	
	1.0	71	13.07.2015	

### 3.2.4 Discussion and perspectives

The differences between the LC\_CCI estimates and the [RD.41] datasets are likely due to the different resolution of the satellite products used and the fact that multiple years were integrated to produce the LC\_CCI maps [RD.42]. The release of yearly land cover maps has been discussed in Phase 2 of the LC\_CCI project. This would certainly be beneficial to studies such as this, as well as to climate modellers who require annual land cover maps to run historical simulations. The higher resolution (30m) Landsat data used in [RD.41] can be used to detect smaller-scale changes in land cover, such as forest harvest and replanting. Thus the LC\_CCI estimates probably underestimate the true magnitude of net changes in forest area, although the fact that the geographical distribution corresponds well with [RD.41] dataset is encouraging [RD.42]. The FAO estimates [RD.40] are also higher than those found with the LC\_CCI, though comparing with these data is not trivial as the FAO data are derived from multiple different sources, including field- and satellite-based estimates.

One puzzling result in this study is that forest gain is only detected between 2005 and 2010. This needs to be further discussed with the LC\_CCI project members involved in algorithm development and the production of the LC maps.

Detecting land cover transitions is of key importance for climate modellers. This study focused on forest transitions; however, as other LC changes are included in the product (for example from grass to crops) this study will be extended to give a more complete picture of land cover change emissions over the past 15 years, with the hope of providing a more accurate estimate for the climate modelling community.

	Ref	LC CCI Climate Assessment Report v1		
	Issue	Page	Date	
	1.0	72	13.07.2015	

# 4 EVALUATION OF THE LC-PFT MAPPING UNCERTAINTY

## 4.1 Introduction

Current generation LSMs use the concept of PFTs to group different vegetation types and species according to similar physiological, biochemical and structural characteristics. The model equations are largely the same for all PFTs, except for certain processes, but the parameters (fixed values) of the equations are mostly PFT-dependent. Thus it is crucial to have accurate information on the PFT fractions in each grid cell. However, PFTs cannot be mapped directly – instead the PFT fractions are derived from species or LC maps that are obtained from other sources of information. The process of converting species or LC classes to PFTs (so-called “cross-walking” procedure) relies on various rules and/or other data sources such as a climate or biome classification, and thus is somewhat subjective [RD.11, RD.12]. Firstly, the LC classification itself can be interpreted in different ways, for example, what fraction of a tree PFT should be assigned to the “closed to open forest” class, which is classified as >40% tree cover? Mixed LC classes pose a particular problem in this regard. Secondly, many LSMs further divide PFTs according to climatic biomes (e.g. into boreal, temperate or tropical biomes). This requires a climate classification, the most commonly used of which is the K-G classification. The K-G system prescribes certain rules to divide the climate data “surfaces” into 31 classes within 5 main types: equatorial, arid, warm temperate, snow and polar. Several sources of uncertainty may arise in this step alone, one being that although various studies have followed this classification they have used different underlying climate datasets (e.g. [RD.44], [RD.24]). Also, the K-G system produces maps with different types of biomes than are used in LSMs, and therefore they themselves have to be grouped depending on how they fit within the LSM description. A third major source of uncertainty in the cross-walking procedure is how to split between C3 and C4 grasses. In the past, each LSM has followed certain rules based on temperature thresholds (e.g. [RD.11]) or using C3/C4 maps derived in other studies (e.g. [RD.45]).

The question of how PFT mapping uncertainty impacts model simulations has been addressed in the previous studies. [RD.13] showed that inaccuracies in satellite-derived LC maps, the aggregation of satellite data to coarser resolution and uncertainty in the LC-to-PFT conversion gave rise to differences of up to ~15% in the gross annual carbon uptake (GPP) across the UK. However [RD.46] found that different meteorological driving data produced greater differences in modelled GPP than different land cover products.

In Phase 1 of the ESA LC\_CCI Project, the Climate Users assessed the impact of driving the models using new PFT maps derived from state-of-the-art land cover maps provided by the project. However, only one cross-walking procedure was followed – there was no assessment of the impact of the accuracy of the LC map itself, or of the subjective choices which are made in the LC-to-PFT cross walking procedure. In this study we attempt to address this issue with the aim of understanding the

	Ref	LC CCI Climate Assessment Report v1		
	Issue	Page	Date	
	1.0	73	13.07.2015	

relative influence of the mapping and cross-walking uncertainty on the spatio-temporal patterns of carbon, water and energy fluxes. However, in order to properly account for all the possible sources of variability detailed above we would need to perform tens to hundreds of model simulations. Here, we simplify the problem by investigating scenarios of “extreme uncertainty” in the context of biomass. We achieve this by quantifying either “minimum” or “maximum” biomass maps for each source of uncertainty: cross-walking uncertainty and land cover uncertainty. We run 3 offline LSMs with both extremes of biomass derived from different sources, and examine their impact on carbon, water and energy fluxes. The key scientific questions we aim to answer are:

- i) Which locations have the greatest amount of uncertainty in the fractional cover of PFTs?
- ii) Do these locations differ according to the source of uncertainty?
- iii) How does the balance between PFTs change according to different sources of uncertainty?

The motivation for this work is to both advice the land cover mapping community about the accuracy requirements for land cover maps, and to provide insights to the earth system modelling community on the implications of decisions taken when converting from land cover to PFTs.

## 4.2 Methodology

The aim of this experimental design is to quantify the effect of uncertainties in the land cover information used in climate models on key indicators of processes in the carbon, hydrological and energy cycles. In order to achieve this, we express uncertainty in the context of either minimizing or maximizing biomass. Using this framework, we quantify the sensitivity of land surface models to uncertainty deriving from the land cover classification approach, and from the cross-walking conversion of land cover classes to fractions of PFTs. In addition to PFT fractions produced with the reference map and cross walking table, 4 different perturbations of PFT fractions were generated, as follows:

1. Land cover uncertainty with alternative classes selected only when
  - a. biomass is minimized ;
  - b. biomass is maximized ;
2. Cross walking table uncertainty with fractions adjusted to
  - a. minimise biomass ;
  - b. maximise biomass.

### 4.2.1 Land Cover class uncertainty

Land cover classification uncertainty (LCU) was assessed using plausible alternative land cover classes that were identified during the land cover classification procedure. An alternative land cover class was deemed to be available for a 300m pixel when the likelihood of it being correct was above 85%, according to the maximum likelihood classifier [AD.7]. The alternative class was chosen for the resulting minimum (maximum) biomass land cover map if it occurs below (above) the first choice class in the biomass hierarchy shown in Table 4-1. If the alternative class was lower down (higher up)

	Ref	LC CCI Climate Assessment Report v1		
	Issue	Page	Date	
	1.0	74	13.07.2015	

the hierarchy of biomass than the first choice class, then it was selected for the minimum (maximum) biomass map. Where no alternative class was available, or the biomass hierarchy criteria were not met, the land cover class remained unchanged from the original map.

*Table 4-1. Each land cover class within the Land Cover CCI legend is assigned a class within a biomass hierarchy for use in assessing classification uncertainty. The highest biomass is tree, followed by shrub, grass, moss and lichen and then bare*

LAND COVER CLASS	DESCRIPTION	BIOMASS HIERARCHY
0	No data	n/a
10	Cropland, rainfed	Grass
11	Cropland, Herbaceous cover	Grass
12	Cropland, Tree or shrub cover	Shrub
20	Cropland, irrigated or post-flooding	Grass
30	Mosaic cropland (>50%) / natural vegetation (tree, shrub, herbaceous cover) (<50%)	Grass
40	Mosaic natural vegetation (tree, shrub, herbaceous cover) (>50%) / cropland (<50%)	Grass
50	Tree cover, broadleaved, evergreen, closed to open (>15%)	Tree
60	Tree cover, broadleaved, deciduous, closed to open (>15%)	Tree
61	Tree cover, broadleaved, deciduous, closed (>40%)	Tree
62	Tree cover, broadleaved, deciduous, open (15-40%)	Shrub
70	Tree cover, needleleaved, evergreen, closed to open (>15%)	Tree
71	Tree cover, needleleaved, evergreen, closed (>40%)	Tree
72	Tree cover, needleleaved, evergreen, open (15-40%)	Shrub
80	Tree cover, needleleaved, deciduous, closed to open (>15%)	Tree
81	Tree cover, needleleaved, deciduous, closed (>40%)	Tree
82	Tree cover, needleleaved, deciduous, open (15-40%)	Shrub
90	Tree cover, mixed leaf type (broadleaved and needleleaved)	Tree
100	Mosaic tree and shrub (>50%) / herbaceous cover (<50%)	Tree
110	Mosaic herbaceous cover (>50%) / tree and shrub (<50%)	Grass
120	Shrubland	Shrub
121	Shrubland evergreen	Shrub
122	Shrubland deciduous	Shrub
130	Grassland	Grass
140	Lichens and mosses	Moss/Lichens
150	Sparse vegetation (tree, shrub, herbaceous cover) (<15%)	Bare

	Ref	LC CCI Climate Assessment Report v1		
	Issue	Page	Date	
	1.0	75	13.07.2015	

LAND COVER CLASS	DESCRIPTION	BIOMASS HIERARCHY
151	Sparse tree (<15%)	Bare
152	Sparse shrub (<15%)	Bare
153	Sparse herbaceous cover (<15%)	Bare
160	Tree cover, flooded, fresh or brakish water	Tree
170	Tree cover, flooded, saline water	Tree
180	Shrub or herbaceous cover, flooded, fresh/saline/brakish water	Grass
190	Urban areas	Bare
200	Bare areas	Bare
201	Consolidated bare areas	Bare
202	Unconsolidated bare areas	Bare
210	Water bodies	n/a
220	Permanent snow and ice	n/a

The assignment of each LC class to a class within a generalized biomass hierarchy is shown in Table 4-1. No effort has been made to quantify specifically the biomass associated with each class – biomass classes are assigned purely with the aim of describing subjectively where a LC class fits within the vegetation succession from tree to shrub to grass cover. The biomass hierarchy is intended to be used to prioritize one LC class over another, to help in the decision of whether to replace the 1<sup>st</sup> choice class with a 2<sup>nd</sup> choice class. For example, if a grid cell has first choice class 40 (grass), and the second choice class 12 (shrub) exceeds the minimum probability threshold, then, if we are making a 'maximum biomass' map, we would use class 12 in the 'max biomass' uncertainty map. If we are making a 'minimum biomass' map, then we don't change the class.

The 2 resulting LC maps were converted to PFT fractions using the LC\_CCI user tool (version 3.7), and the resulting fractions were aggregated further to meet the needs of the JSBACH, JULES and ORCHIDEE land surface models. It is proposed that the final PFT fraction maps for minimum and maximum biomass represent the largest possible range of quantifiable land cover class uncertainty in the context of land surface models.

#### 4.2.2 Cross-walking uncertainty

Uncertainty also arises from the translation of land cover classes to the PFTs used in land surface models. In this case, assumptions are made on the fraction of each PFT that occurs within a given land cover class. These assumptions are based on the fractional cover of major vegetation types derived from the Land Cover Classification System (LCCS) [RD.47] that is the basis of the LC\_CCI legend [RD.12]. The LCCS description defines a range of fractions of vegetation cover for each LC\_CCI class. This information is then used to guide expert judgement on the exact fractions of PFTs that occur in each land cover class, resulting in a cross-walking matrix that translates land cover classes into plant functional types.

	Ref	LC CCI Climate Assessment Report v1		
	Issue	Page	Date	
	1.0	76	13.07.2015	

In cross-walking procedure, uncertainty arises in the translation of a land cover class to the fractional cover of the PFTs used by LSMs. Uncertainty in the fraction of each PFT found within a given land cover class may arise from a number of factors, namely:

- Regional variations in the density of cover;
- Variations in agreement between experts ;
- Coarse spatial resolution of satellite retrievals;
- Lack of very high resolution calibration datasets.

Each of the above factors may affect the values found in the reference LC\_CCI cross-walking table [RD.12]. However, it is currently not known how sensitive LSMs are to plausible perturbations in this table.

In this experiment, cross-walking uncertainty was quantified in the context of either minimum or maximum biomass (Table 4-2). Where possible, the LCCS class description was used to create a “minimum biomass” and a “maximum biomass” cross-walking matrix. For example, class 61 (Broadleaf deciduous tree cover, closed (>40%)) is converted to 70% broadleaf deciduous tree PFT in the reference dataset. In the “minimum biomass” cross-walking, this value reduces to 40%, the minimum fractional cover permitted by the LCCS description. Conversely, in the “maximum biomass” cross-walking, 100% of the grid cell is converted to broadleaf deciduous tree PFT.

Table 4-2. Perturbations of the cross walking table from [RD.12]

ID	Description	BLE Tree			BLD Tree			NLE Tree			NLD Tree			BLE Shrub			BLD Shrub			NLE Shrub			NLD Shrub			Natural Grass			Managed Grass			Bare Soil			Water	Snow / Ice
		Min Bm	Ref	Max Bm	Min Bm	Ref	Max Bm	Min Bm	Ref	Max Bm	Min Bm	Ref	Max Bm	Min Bm	Ref	Max Bm	Min Bm	Ref	Max Bm	Min Bm	Ref	Max Bm	Ref	Ref												
0	No data	0	0	0	0	0	0	0	0	0	0	0	0	0	0	0	0	0	0	0	0	0	0	0	0	0	0	0	0	0	0	0	0	0		
10	Cropland, rainfed	0	0	0	0	0	0	0	0	0	0	0	0	0	0	0	0	0	0	0	0	0	0	0	0	0	0	60	100	100	40	0	0	0	0	
11	Herbaceous cover	0	0	0	0	0	0	0	0	0	0	0	0	0	0	0	0	0	0	0	0	0	0	0	0	0	60	100	100	40	0	0	0	0		
12	Tree or shrub cover	0	0	0	0	0	0	0	0	0	0	0	0	0	0	30	50	50	0	0	0	0	0	0	0	0	0	30	50	50	40	0	0	0	0	
20	Cropland, irrigated or post-flooding	0	0	0	0	0	0	0	0	0	0	0	0	0	0	0	0	0	0	0	0	0	0	0	0	0	100	100	100	0	0	0	0	0		
30	Mosaic cropland (>50%) / natural vegetation (tree, shrub, herbaceous cover) (<50%)	0	5	10	0	5	10	0	0	0	0	0	0	3.3	5	5	3.3	5	5	3.4	5	5	0	0	0	15	15	15	75	60	50	0	0	0	0	
40	Mosaic natural vegetation (tree, shrub, herbaceous cover) (>50%) / cropland (<50%)	0	5	15	0	5	15	0	0	0	0	0	0	7.5	7.5	7.5	10	10	10	7.5	7.5	7.5	0	0	0	25	25	25	50	40	20	0	0	0	0	
50	Tree cover, broadleaved, evergreen, closed to	70	90	100	0	0	0	0	0	0	0	0	7.5	5	0	7.5	5	0	0	0	0	0	0	0	15	0	0	0	0	0	0	0	0	0		

ID	Description	BLE Tree			BLD Tree			NLE Tree			NLD Tree			BLE Shrub			BLD Shrub			NLE Shrub			NLD Shrub			Natural Grass			Managed Grass			Bare Soil			Water	Snow / Ice
		Min Bm	Ref	Max Bm	Min Bm	Ref	Max Bm	Min Bm	Ref	Max Bm	Min Bm	Ref	Max Bm	Min Bm	Ref	Max Bm	Min Bm	Ref	Max Bm	Min Bm	Ref	Max Bm	Ref	Ref												
	open (>15%)																																			
60	Tree cover, broadleaved, deciduous, closed to open (>15%)	0	0	0	40	70	100	0	0	0	0	0	0	0	0	15	15	0	0	0	0	0	0	0	45	15	0	0	0	0	0	0	0	0		
61	Tree cover, broadleaved, deciduous, closed (>40%)	0	0	0	40	70	100	0	0	0	0	0	0	0	0	15	15	0	0	0	0	0	0	0	45	15	0	0	0	0	0	0	0	0		
62	Tree cover, broadleaved, deciduous, open (15-40%)	0	0	0	15	30	40	0	0	0	0	0	0	0	0	25	25	25	0	0	0	0	0	0	50	35	35	0	0	0	10	10	0	0	0	
70	Tree cover, needleleaved, evergreen, closed to open (>15%)	0	0	0	0	0	0	40	70	100	0	0	0	5	5	0	5	5	0	5	5	0	0	0	45	15	0	0	0	0	0	0	0	0		
71	Tree cover, needleleaved, evergreen, closed (>40%)	0	0	0	0	0	0	40	70	100	0	0	0	5	5	0	5	5	0	5	5	0	0	0	45	15	0	0	0	0	0	0	0	0		

ID	Description	BLE Tree			BLD Tree			NLE Tree			NLD Tree			BLE Shrub			BLD Shrub			NLE Shrub			NLD Shrub			Natural Grass			Managed Grass			Bare Soil			Water Ref	Snow / Ice Ref
		Min Bm	Ref	Max Bm	Min Bm	Ref	Max Bm	Min Bm	Ref	Max Bm	Min Bm	Ref	Max Bm	Min Bm	Ref	Max Bm	Min Bm	Ref	Max Bm	Min Bm	Ref	Max Bm	Min Bm	Ref	Max Bm											
72	Tree cover, needleleaved, evergreen, open (15-40%)	0	0	0	0	0	0	15	30	40	0	0	0	0	0	0	5	5	5	5	5	5	0	0	0	45	30	30	0	0	0	30	30	20	0	0
80	Tree cover, needleleaved, deciduous, closed to open (>15%)	0	0	0	0	0	0	0	0	0	40	70	100	5	5	0	5	5	0	5	5	0	0	0	0	45	15	0	0	0	0	0	0	0	0	0
81	Tree cover, needleleaved, deciduous, closed (>40%)	0	0	0	0	0	0	0	0	0	40	70	100	5	5	0	5	5	0	5	5	0	0	0	0	45	15	0	0	0	0	0	0	0	0	0
82	Tree cover, needleleaved, deciduous, open (15-40%)	0	0	0	0	0	0	0	0	0	15	30	40	0	0	0	5	5	5	5	5	5	0	0	0	45	30	30	0	0	0	30	30	20	0	0
90	Tree cover, mixed leaf type (broadleaved and needleleaved)	0	0	0	20	30	50	13.3	20	33.3	6.7	10	16.7	5	5	0	5	5	0	5	5	0	0	0	0	35	15	0	0	0	0	10	10	0	0	0
100	Mosaic tree and shrub (>50%) / herbaceous	7.5	10	15	15	20	30	3.8	5	7.5	3.7	5	7.5	5	5	5	10	10	10	5	5	5	0	0	0	50	40	20	0	0	0	0	0	0	0	0



ID	Description	BLE Tree			BLD Tree			NLE Tree			NLD Tree			BLE Shrub			BLD Shrub			NLE Shrub			NLD Shrub			Natural Grass			Managed Grass			Bare Soil			Water	Snow / Ice
		Min Bm	Ref	Max Bm	Min Bm	Ref	Max Bm	Min Bm	Ref	Max Bm	Min Bm	Ref	Max Bm	Min Bm	Ref	Max Bm	Min Bm	Ref	Max Bm	Min Bm	Ref	Max Bm	Ref	Ref												
160	Tree cover, flooded, fresh or brakish water	20	30	37.5	20	30	37.5	0	0	0	0	0	0	0	0	0	0	0	0	0	0	0	0	0	0	30	20	12.5	0	0	0	0	0	0	20	0
170	Tree cover, flooded, saline water	40	60	75	0	0	0	0	0	0	0	0	0	30	20	12.5	0	0	0	0	0	0	0	0	0	0	0	0	0	0	0	0	0	0	20	0
180	Shrub or herbaceous cover, flooded, fresh/saline/brakish water	0	0	0	0	5	5	0	10	10	0	0	0	0	0	0	12.7	10	10	6.4	5	5	0	0	0	50.9	40	40	0	0	0	0	0	0	30	0
190	Urban areas	0	0	0	2.5	2.5	2.5	2.5	2.5	2.5	0	0	0	0	0	0	0	0	0	0	0	0	0	0	0	15	15	15	0	0	0	75	75	75	5	0
200	Bare areas	0	0	0	0	0	0	0	0	0	0	0	0	0	0	0	0	0	0	0	0	0	0	0	0	0	0	0	0	0	0	100	100	100	0	0
201	Consolidated bare area	0	0	0	0	0	0	0	0	0	0	0	0	0	0	0	0	0	0	0	0	0	0	0	0	0	0	0	0	0	0	100	100	100	0	0
202	Unconsolidated bare areas	0	0	0	0	0	0	0	0	0	0	0	0	0	0	0	0	0	0	0	0	0	0	0	0	0	0	0	0	0	0	100	100	100	0	0
210	Water bodies	0	0	0	0	0	0	0	0	0	0	0	0	0	0	0	0	0	0	0	0	0	0	0	0	0	0	0	0	0	0	0	0	0	100	0
220	Permanent snow and ice	0	0	0	0	0	0	0	0	0	0	0	0	0	0	0	0	0	0	0	0	0	0	0	0	0	0	0	0	0	0	0	0	0	0	100

	Ref	LC CCI Climate Assessment Report v1		
	Issue	Page	Date	
	1.0	82	13.07.2015	

### 4.2.3 PFT aggregation

In order to summarize the PFT uncertainty information so that it is broadly comparable for all LSMs, we aggregated the results of the PFT fractions into 4 cover types: tree, shrub, grass and bare. The PFT fractions were aggregated according to Table 4-3.

*Table 4-3. Aggregation of PFTs for analysis*

PFT	AGGREGATED COVER TYPE
Broadleaf Evergreen Tree	Tree
Broadleaf Deciduous Tree	
Needleleaf Evergreen Tree	
Needleleaf Deciduous Tree	
Broadleaf Evergreen Shrub	Shrub
Broadleaf Deciduous Shrub	
Needleleaf Evergreen Shrub	
Needleleaf Deciduous Shrub	
Natural Grass	Grass
Managed Grass	
Bare Soil	Bare
Water	Not perturbed
Snow and Ice	Not perturbed

## 4.3 Results

### 4.3.1 PFT maps

Figure 4-1 shows the maps resulting from the uncertainty in the LC mapping uncertainty (2<sup>nd</sup> and 4<sup>th</sup> column), as detailed in Section 4.2.1 and from both the LC mapping uncertainty and the cross-walking procedure, as detailed in Section 4.2.2 (1<sup>st</sup> and 4<sup>th</sup> columns) compared to the reference case (3<sup>rd</sup> column).

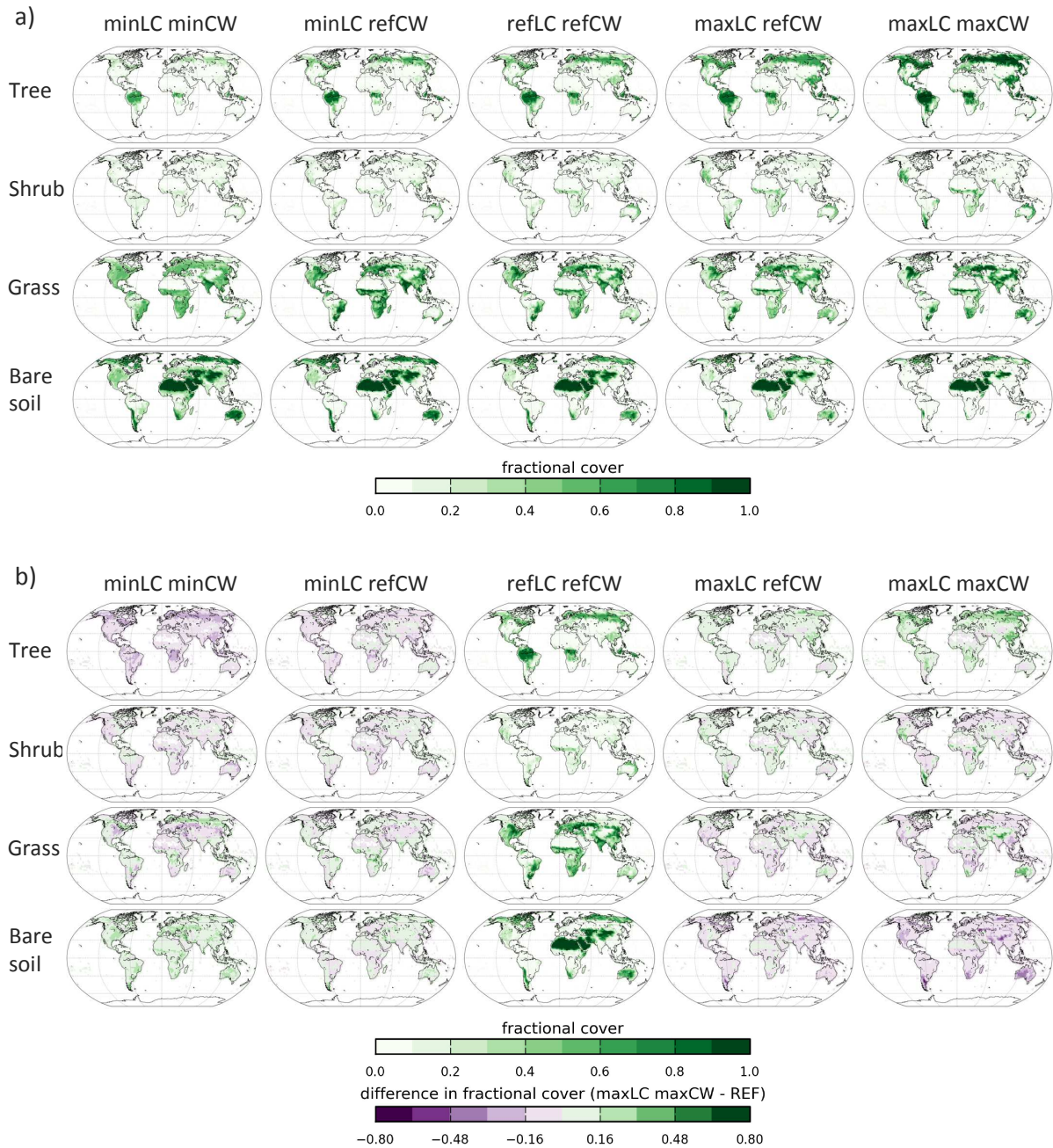


Figure 4-1. Maps showing a) the fraction of vegetation for the Trees (1<sup>st</sup> row), Shrubs (2<sup>nd</sup> row), Natural and Managed Grasses (3<sup>rd</sup> row) and Bare soil (4<sup>th</sup> row), and b) the difference between each case and the reference for each of the uncertainty simulations. The reference case is shown in the middle column (refLC refCW), the minimum biomass vegetation distribution maps are shown to the left of the reference case, first with minimum LC maps and the reference cross-walking table (minLC refCW – 2<sup>nd</sup> column) and with both the minimum biomass LC maps and minimum cross-walking table (minLC minCW – 1<sup>st</sup> column). To the right of the reference map are the equivalent maximum biomass vegetation distributions (maxLC refCW – 4<sup>th</sup> column, maxLC maxCW – 5<sup>th</sup> column).

	Ref	LC CCI Climate Assessment Report v1		
	Issue	Page	Date	
	1.0	84	13.07.2015	

Figure 4-1a shows maps of the actual vegetation fraction for the major biomass classes (tree, shrub, grass) and bare soil uncertainty cases according to method described in Section 4.2.1 and 4.2.2. The reference map with the original LC\_CCI map and the default cross-walking table (as detailed in [RD.12]) is shown in the central column. The left hand columns (1<sup>st</sup> and 2<sup>nd</sup>) show maps of the “minimum biomass” cases produced with both sources of uncertainty and with just the LC map uncertainty, respectively. The right hand side (4<sup>th</sup> and 5<sup>th</sup> columns) shows the equivalent for the “maximum biomass” uncertainty. Figure 4-1b shows equivalent maps but for the “maximum” and “minimum” cases (1<sup>st</sup>, 2<sup>nd</sup>, 4<sup>th</sup>, 5<sup>th</sup> columns), the difference compared to the reference is shown.

In line with the methodology, the bare soil, grass and shrubland minimum biomass maps have greater fractional coverage, but lower biomass, than the forests. In the maximum biomass maps biomass increases for regions that are dominated by the class in question. The overall spatial distribution of the tree and shrub classes (Figure 4-1a top two rows) does not change, but the fraction of vegetation cover increases in an approximate linear trend between the minimum and maximum biomass changes. The spatial distribution does change for the bare soil fraction, except for regions where there is no uncertainty in the bare soil class, such as in the Sahara desert and the central Asian arid plains. The bottom row in Figure 4-1 a and b show the bare soil distributions. The bare soil class represents a negative of vegetation and looking at the bare soil changes (Figure 4-1b), we can also get an idea about changes in vegetation. In the bare soil class, there is a deprivation of vegetated area (i.e. increase in the minimum biomass columns) or decrease in the bare soil fraction (i.e. decrease in the maximum biomass columns) globally in comparison with reference map when both sources of uncertainty are considered, respectively (minLC minCW or maxLC maxCW). In general, there is a strong increase of bare soil fraction for the high latitudes, North America, Chile and semi-arid regions in Australia and Central Asia. The minimum LC uncertainty (minLC refCW) can result in a decrease in the bare soil fraction for the minimum biomass case, or conversely an increase for the maximum biomass case. This shows the impact of decisions made in the cross-walking table for dealing with complex mixed classes. For example, for the minimum biomass LC only map, there was an increase in a “sparse vegetation” class in the African Central Rainforest, but this class actually has a lower fraction of bare soil and a higher fraction of grass, compared to the mosaic classes in the original map, so overall the bare soil fraction has decreased.

The grassland class is the most complicated. The spatial distribution does change, especially in high latitude regions (>60°N) and tropical rainforests where grass is present in minimum biomass maps but not in the maximum biomass case (as the tree fraction has strongly increased). The opposite is true for semi-arid regions such as central Australia where there is almost no grass in the minimum biomass cases (as the bare soil fraction has increased) but a strong increase for the maximum biomass scenarios. The minimum LC reference cross-walking case appears similar to the maximum LC maximum cross-walking case, and this is again due to complexities that arise due to the LC-to-PFT conversion factors implemented in the cross-walking table for classes with a complex mosaic of vegetation.

### 4.3.2 PFT Uncertainty by Giorgi Region

Regional variations in the plant functional type fractions can have significant impacts on the regional exchanges of heat, moisture and carbon in land surface models. Here, we summarize the different uncertainty scenarios according to the large-scale climatic regions suggested by [RD.48], as shown in Figure 4-2 and Table 4-4.

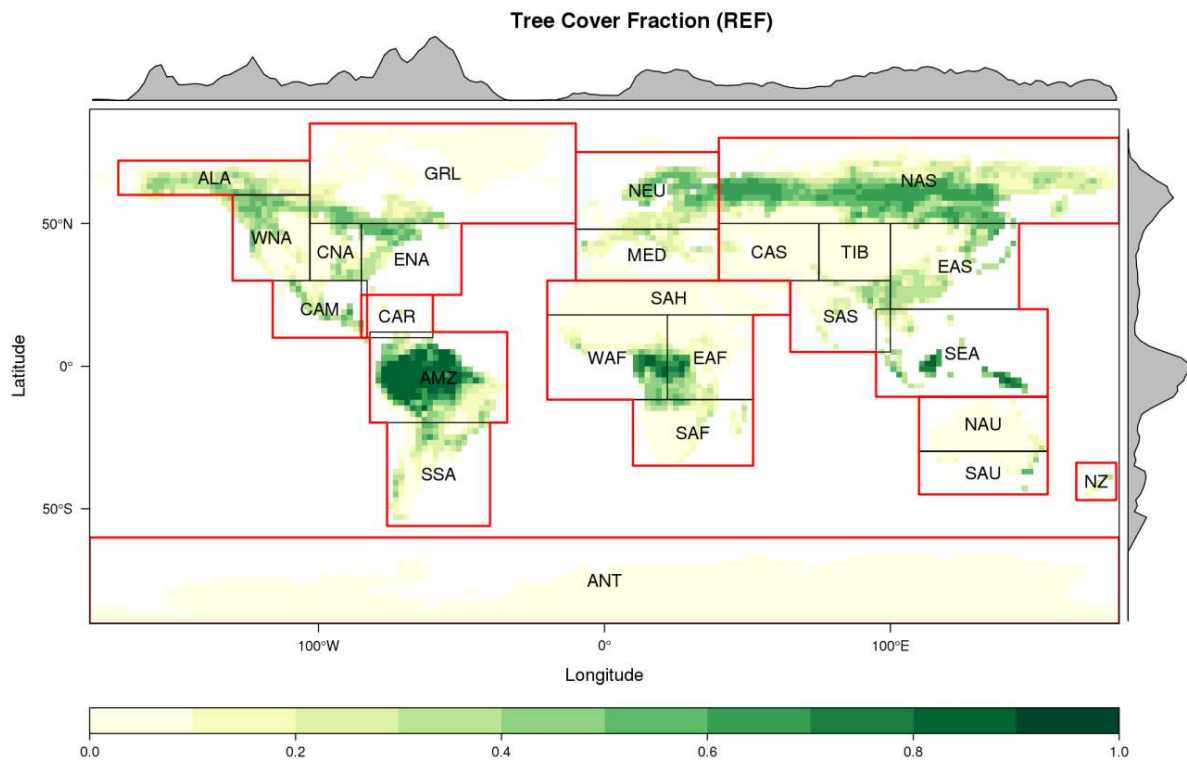


Figure 4-2. Giorgi Regions used for summarising vegetation fractions, overlaid onto tree fractional cover from the reference land cover map. Red boundaries indicate the continent boundaries used in Figure 4-3 and the surrounding grey histograms show longitudinal (top), and latitudinal (right) mean fractions

	Ref	LC CCI Climate Assessment Report v1		
	Issue	Page	Date	
	1.0	86	13.07.2015	

Table 4-4. Description of Giorgi regions as shown in Figure 4-2

ID	Description	Continent
<b>ALA</b>	Alaska, Northwestern Canada	North America
<b>GRL</b>	Greenland, Eastern Canada	North America
<b>WNA</b>	Western North America	North America
<b>CNA</b>	Central North America	North America
<b>ENA</b>	Eastern North America	North America
<b>CAM</b>	Central America	North America
<b>AMZ</b>	Amazonia	South America
<b>SSA</b>	Southern South America	South America
<b>NEU</b>	Northern Europe	Europe
<b>MED</b>	Southern Europe, Northern Africa	Europe
<b>SAH</b>	Sahara	Africa
<b>WAF</b>	Western Africa	Africa
<b>EAF</b>	Eastern Africa	Africa
<b>SAF</b>	Southern Africa	Africa
<b>NAS</b>	Northern Asia	Asia
<b>CAS</b>	Central Asia	Asia
<b>TIB</b>	Tibetan Plateau	Asia
<b>EAS</b>	Eastern Asia	Asia
<b>SAS</b>	Southern Asia	Asia
<b>SEA</b>	Southeast Asia	Asia
<b>NAU</b>	Northern Australia	Australasia
<b>SAU</b>	Southern Australia	Australasia
<b>CAR</b>	Caribbean	South America
<b>ANT</b>	Antarctic land south of 60S	Antarctic
<b>NZ</b>	New Zealand	Australasia

Figure 4-3 shows the mean area-weighted fraction of cover of each cover type for all the Giorgi regions as coloured bars, and the fractional cover arising from each uncertainty scenario as points. It is immediately apparent that there is considerable uncertainty in most regions for most cover types. Only regions such as the Sahara, where there is clearly one cover type, have little variance between the uncertainty scenarios. Generally, we see equal amounts of uncertainty arising from the LC map and the cross-walking table, shown by the equal vertical spacing of points. However, it is notable in all parts of Africa (East Africa: EAF; Southern Africa: SAF; and West Africa: WAF) that LC uncertainty has a relatively small effect on the bare soil fraction. In these areas, cross-walking table uncertainty has the largest impact on bare fraction. In other continents with a large bare fraction, such as Asia and Australasia, LC uncertainty and cross-walking uncertainty appear to have equal effects.

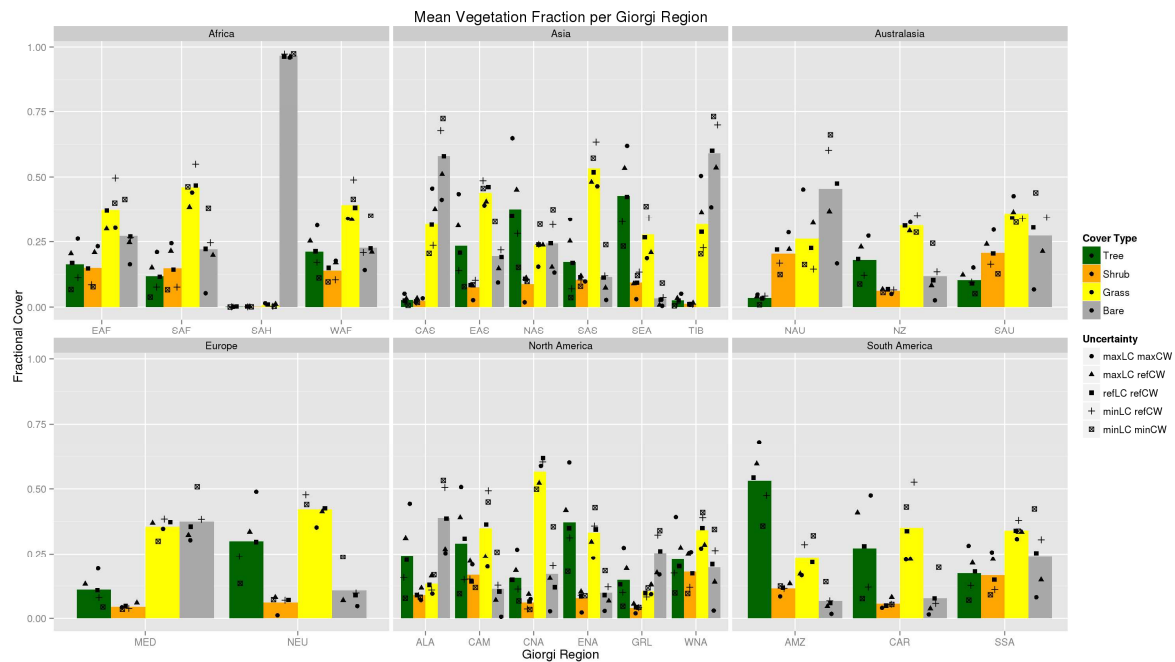


Figure 4-3. Mean fractional cover for each Giorgi Region, separated by continent. Values shown by the coloured bars represent the spatial mean for each cover type in the reference land cover map. Error bars show the minimum and maximum values for each bar from the uncertainty estimates

The difference between minimum biomass and maximum biomass scenarios is also apparent in Figure 4-3. In regions where all four cover types are represented, we see that the maximum biomass scenarios tend to have more tree and shrub cover than the reference scenario, and less grass and bare fraction than the reference. Figure 4-3 also shows that combining the upper range of uncertainty in both LC (maxLC) and cross-walking (maxCW) leads to the highest fraction of tree cover in all regions (see filled circles). The same is also true for bare fraction, where the lower range of uncertainty for both LC (minLC) and cross-walking (minCW) leads to the highest fraction of bare cover in all regions (see open squares with cross).

Interestingly, grass fractions do not follow the same pattern as tree and bare fractions. For this cover type, we find that the combination of minLC and reference cross-walking (refCW) results in the highest fraction of grass cover in many regions. This occurs in Africa (East, West and Southern), Asia (south and East), as well as New Zealand, Central America, Southern South America, and Northern Europe. This therefore indicates that while the minLC scenario results in more grass cover in these regions, the minCW scenario results in less grass cover. The fact that this is not true for all regions also indicates that cross-walking uncertainty can either lead to an increase or decrease in grass cover. An increase in grass cover under a maximizing biomass scenario may occur, for example, where perturbations in the cross-walking of sparsely vegetated classes lead to greater grass fractions. However, more densely vegetated classes (such as mosaics of tree, shrub and grass cover) would experience a reduction in grass fraction under a maximizing biomass scenario.

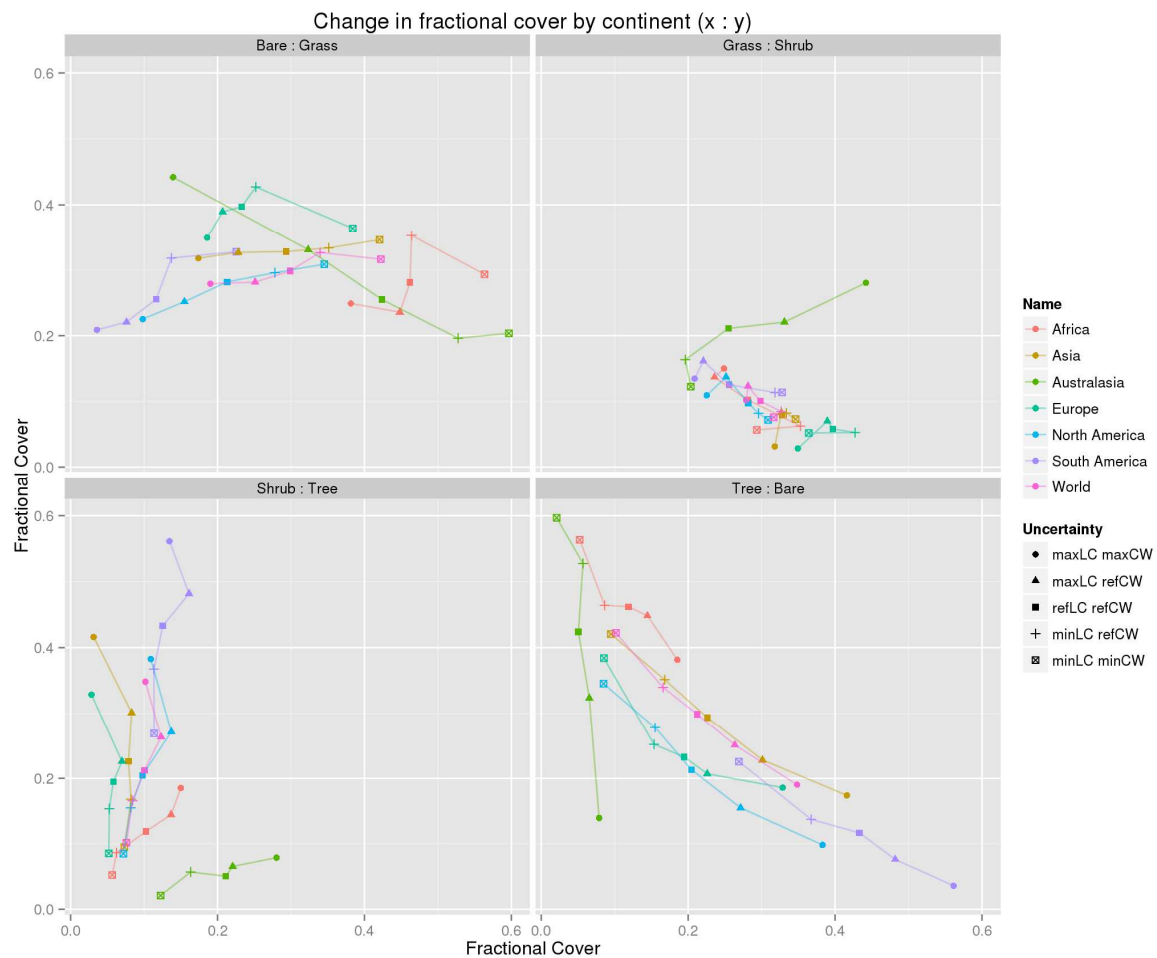


Figure 4-4. Impact of uncertainty on the balance between different vegetation types at the continental (and global) scale. Each point shows the average fraction of one cover type compared to another, over a given continent (or the whole world) for a given type of uncertainty. Labels at the top of each scatterplot indicate the cover types shown in the x axis (first label), and the y axis (second label).

Figure 4-4 shows the relationship between all cover types for each continent, and how they change under different uncertainty scenarios. The relationships between bare soil and tree cover (bottom right) are quite linear, indicating that as tree cover increases, bare soil fraction decreases in equal proportions for all uncertainty scenarios. This happens at similar rates for most of the world, but it is much steeper in Australasia, where a relatively small reduction in tree cover along the gradient of minLC-minCW to maxLC-maxCW occurs at the same time as a very large increase in bare soil fraction.

The relationship between bare soil and grass cover also reveals interesting patterns. Africa and South America show small increases in bare soil fraction, but large increases in grass cover for uncertainty related to land cover (minLC to maxLC). However, cross walking uncertainty in these regions has the opposite effect; large increases in bare fraction are found (minCW to maxCW), and small changes in grass fraction. In particular, the minCW scenario has the effect of decreasing grass cover (relative to minLC-refCW) in both Africa and Europe.

	Ref	LC CCI Climate Assessment Report v1		
	Issue	Page	Date	
	1.0	89	13.07.2015	

### 4.3.3 Latitudinal uncertainty

Figure 4-5 provides a quantified insight into the uncertainty range due to the LC classification and the LC map conversion into a PFT distribution. The most prominent feature is the complementary distribution of trees and bare soil areas modified by shrub and grass. If we have had only trees and bare soil, the maximum of the tree distribution would appear complementary to the minimum of the bare soil area. The tree area distribution is characterized by tropical-equatorial (from 25°S to 10°N), subtropical (around 30°S) and northern midlatitude-arctic (from 40°N to 70°N) maxima. The range of these peaks varies from  $\sim 700 \times 10^9 \text{ m}^2$  (subtropical) up to  $\sim 1500 \times 10^9 \text{ m}^2$  (northern midlatitude-arctic). The distribution of the bare soil area reaches its peak in the zone where the tree distribution area reaches its minimum. The range of uncertainty in the bare soil area distribution varies from  $\sim 750 \times 10^9 \text{ m}^2$  in the arctic zone up to  $\sim 1200 \times 10^9 \text{ m}^2$  (around 40°N). It is interesting to note that the arctic maximum (north of 60°N) of the bare soil uncertainty is predominantly due to LC classification uncertainty and not the cross-walking procedure. Therefore this indicates that cross-walking uncertainty has very little impact on bare soil area at this latitude, with almost all of the uncertainty related to choice of land cover class. Further south, however, around 60°N uncertainty in grass cover is almost all related to cross walking uncertainty, and not land cover uncertainty.

The almost ideal bipolar character of the bare soil and forest distributions is modified by shrubs and grasses. Grasses show a similar range of uncertainty for the whole globe ( $\sim 200\text{-}600 \times 10^9 \text{ m}^2$ ). It is worth to note that the uncertainty changes its amount in accord with the excess or deprivation of the bare soil and forest area distributions. For example in the southern subtropical zone ( $\sim 28^\circ\text{S}$ ), the conversion method that maximizes biomass by LC classification and cross-walking procedure (MaxLC MaxCW) has the lowest amount of the bare soil in comparison with other conversion methods. In that same region, MaxLC MaxCW provides the largest amount of grass as long as the forest is not becoming predominant vegetation type ( $\sim 25^\circ\text{S} - 10^\circ\text{N}$ ). In that zone, MaxLC MaxCW conversion method provides the lowest amount of grass in comparison to other conversion methods. The pattern of change in shrub area distribution appears to be more complex. However, the most remarkable feature is a sudden drop of shrubs northern of  $\sim 45^\circ\text{N}$  for MaxLC MaxCW conversion method, while all other conversions provide about the same amount of shrubs.

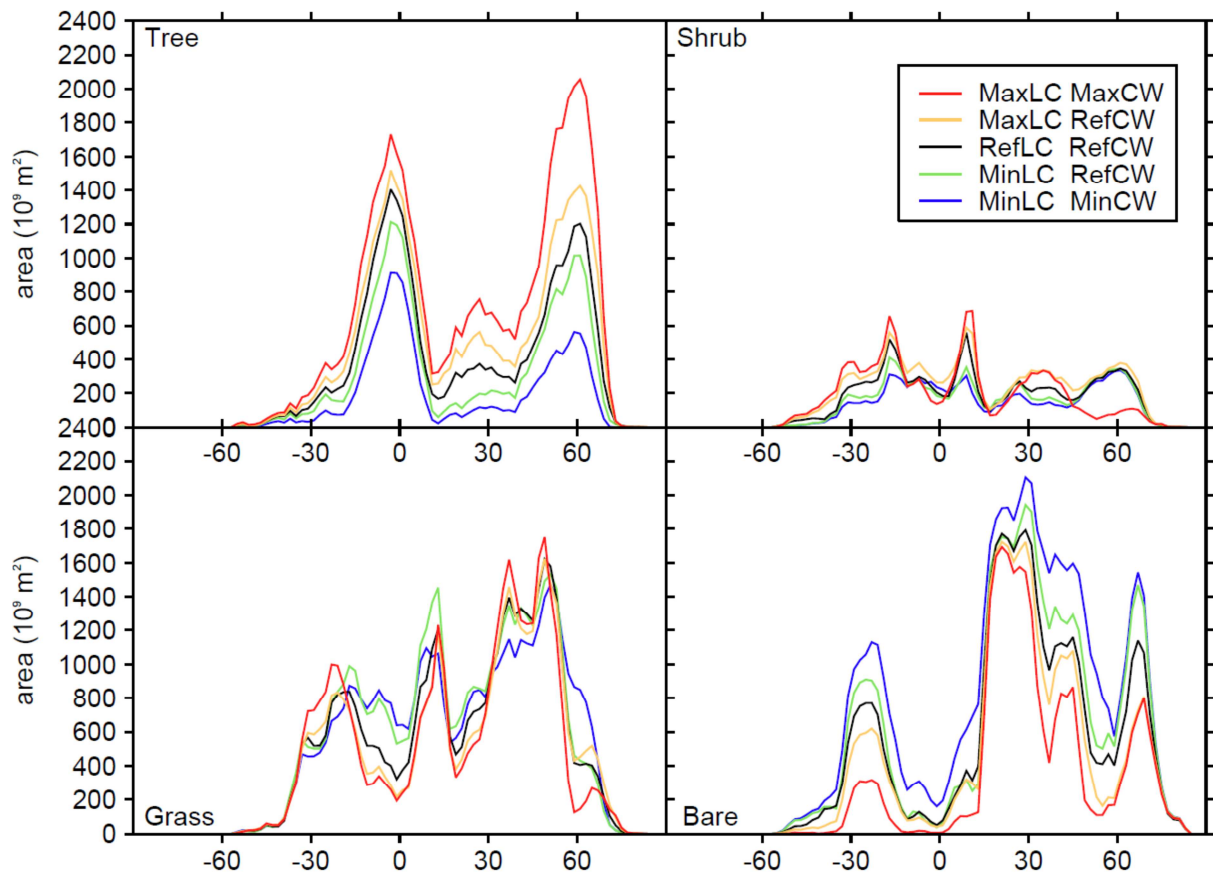


Figure 4-5. Zonal distribution of area covered by the bare soil and major vegetation types (tree, shrub and grass) according to 5 different combinations of LC maps and cross-walking procedure

#### 4.4 Discussion and Conclusions

This information has important implications for the regions and classes on which future LC mapping efforts are focused. We have shown that there is still considerable uncertainty in the methods used to convert LC into the PFTs used by land surface models. Furthermore, uncertainty in the labelling of LC classes has been shown to be of an equal magnitude to cross-walking uncertainty.

- Maximizing (minimizing) biomass in LC uncertainty and cross-walking uncertainty leads to the largest (smallest) tree cover fractions and the smallest (largest) bare soil fractions in all regions;
- Uncertainty in bare soil fraction in northern latitudes (north of 60°N) is all related to choice of LC class, not cross-walking uncertainty. Further South however, grass cover uncertainty is all related to cross-walking uncertainty rather than LC uncertainty
- In the tropics (15°S to 15°N), tree cover uncertainty is equally related to LC and cross-walking uncertainty, whereas in the other major forest belt (45°N to 65°N), uncertainty is more related to cross-walking uncertainty. This is also seen in northern Asia (NAS) and eastern North America (ENA) Giorgi regions;

	Ref	LC CCI Climate Assessment Report v1		
	Issue	Page	Date	
	1.0	91	13.07.2015	

- Uncertainty in grass and shrub fractions is more locally dependent. It appears this is due to regional differences in land cover uncertainty in grass classes, and cross-walking uncertainty affecting different classes in different ways. For example, in tropical regions, maximizing biomass in the cross-walking approach leads to a reduction in grass cover relative to the reference, whereas in temperate regions (30°N to 50°N and 25°S to 35°S), maximizing biomass leads to an increase in grass cover.

The maps are not very realistic for using in climate model simulations, but the aim here is not to try to use these maps to quantify the uncertainty in model simulations as a result of realistic LC uncertainties, but rather to highlight the contribution of different types of uncertainty in mapping from LC to PFTs. Certainly decisions that have to be made in this process are somewhat subjective, and therefore we should either drive the models with a vegetation distribution that can be more directly derived from satellite data, for example the notion of “optical functional types” (e.g. [RD.49]), which may correspond to the original classes defined from the unsupervised classification algorithm in the LC\_CCI project, one step before these groups are categorized into LC classes. In an ideal scenario, we would derive species maps from very high-resolution data and expert knowledge, but this is perhaps unrealistic on a global scale. The alternative is that we need to move away from prescribing discrete vegetation types but rather follow the plant traits (continuous) approach. For now, most climate modellers do derive the PFT vegetation maps used in climate simulations from LC maps. We show that this can lead to considerable uncertainty in the derived PFT fractions, and this can especially be true for complex “mixed” LC classes.

	Ref	LC CCI Climate Assessment Report v1		
	Issue	Page	Date	
	1.0	92	13.07.2015	

## 5 APPENDIX – DRAFT PAPER ON UNCERTAINTY ANALYSIS

### Impact of uncertainties in land cover maps and land cover to PFT conversion on simulated carbon, water and energy fluxes – a land surface model intercomparison

Authors: CCI LC Climate Users

[1]{ }

[2]{ }

[\*]{now at: }

Correspondence to:

#### Abstract

#### 1. Introduction

Current generation Land Surface Models (LSMs) use the concept of Plant Functional Types (PFTs) to group different vegetation types and species according to similar physiological, biochemical and structural characteristics. The model equations are largely the same for all PFTs, except for certain processes, but the parameters (fixed values) of the equations are mostly PFT-dependent. Thus it is crucial to have accurate information on the PFT fractions in each grid cell. However, PFTs cannot be mapped directly – instead the PFT fractions are derived from species or land cover (LC) maps that are obtained from other sources of information. The process of converting species or LC classes to PFTs (so-called “cross-walking” procedure) relies on various rules and/or other data sources such as a climate or biome classification, and thus is somewhat subjective (Poulter et al., 2011; Poulter et al., 2015). Firstly, the LC classification itself can be interpreted in different ways, for example, what fraction of a tree PFT should be assigned to the “closed to open forest” class, which is classified as >40% tree cover? Mixed LC classes pose a particular problem in this regard. Secondly, many LSMs further divide PFTs according to climatic biomes (e.g. into boreal, temperate or tropical biomes). This requires a climate classification, the most commonly used of which is the Köppen-Geiger (K-G) classification. The K-G system prescribes certain rules to divide the climate data “surfaces” into 31

	Ref	LC CCI Climate Assessment Report v1		
	Issue	Page	Date	
	1.0	93	13.07.2015	

classes within 5 main types: equatorial, arid, warm temperate, snow and polar. Several sources of uncertainty may arise in this step alone, one being that although various studies have followed this classification they have used different underlying climate datasets (e.g. Kottek et al., 2006; Peel et al., 2007). Also, the K-G system produces maps with different types of biomes than are used in LSMs, and therefore they themselves have to be grouped depending on how they fit within the LSM description. A third major source of uncertainty in the cross-walking procedure is how to split between C3 and C4 grasses. In the past, each LSM has followed certain rules based on temperature thresholds (e.g. Poulter et al., 2011) or using C3/C4 maps derived in other studies (e.g. Still et al., 2003).

The question of how PFT mapping uncertainty impacts model simulations has been addressed in the previous studies. Quaife et al. (2008) showed that inaccuracies in satellite-derived LC maps, the aggregation of satellite data to coarser resolution and uncertainty in the LC-to-PFT conversion gave rise to differences of up to ~15% in the gross annual carbon uptake (GPP) across the UK. However Jung et al. (2007) found that different meteorological driving data produced greater differences in modelled GPP than different land cover products.

In Phase 1 of the ESA CCI Land Cover Project, the Climate Users assessed the impact of driving the models using new PFT maps derived from state-of-the-art land cover maps provided by the ESA CCI Land Cover project. However, only one cross-walking procedure was followed – there was no assessment of the impact of the accuracy of the LC map itself, or of the subjective choices which are made in the LC-to-PFT cross walking procedure. In this study we attempt to address this issue with the aim of understanding the relative influence of the mapping and cross-walking uncertainty on the spatio-temporal patterns of carbon, water and energy fluxes. However, in order to properly account for all the possible sources of variability detailed above we would need to perform tens to hundreds of model simulations. Here, we simplify the problem by investigating scenarios of “extreme uncertainty” in the context of biomass. We achieve this by quantifying either “minimum” or “maximum” biomass maps for each source of uncertainty: cross-walking uncertainty and land cover uncertainty. We run 3 offline LSMs with both extremes of biomass derived from different sources, and examine their impact on carbon, water and energy fluxes. The key scientific questions we aim to answer are:

- iv) Which locations have the greatest amount of uncertainty in the fractional cover of PFTs?
- v) Do these locations differ according to the source of uncertainty?
- vi) How does the balance between PFTs change according to different sources of uncertainty?

	Ref	LC CCI Climate Assessment Report v1		
	Issue	Page	Date	
	1.0	94	13.07.2015	

The motivation for this work is to both advise the land cover mapping community about the accuracy requirements for land cover maps, and to provide insights to the earth system modelling community on the implications of decisions taken when converting from land cover to PFTs.

## 2. Data and methods

The aim of this experimental design is to quantify the effect of uncertainties in the land cover information used in climate models on key indicators of processes in the carbon, hydrological and energy cycles. In order to achieve this, we express uncertainty in the context of either minimising or maximising biomass. Using this framework, we quantify the sensitivity of land surface models to uncertainty deriving from the land cover classification approach, and from the cross-walking conversion of land cover classes to fractions of plant functional types (PFTs). In addition to PFT fractions produced with the reference map and cross walking table, 4 different perturbations of PFT fractions were generated, as follows:

3. Land cover uncertainty with alternative classes selected only when
  - a. biomass is minimised
  - b. biomass is maximised
  
4. Cross walking table uncertainty with fractions adjusted to
  - a. minimise biomass
  - b. maximise biomass

### 2.1. Land Cover Class Uncertainty

Land cover classification uncertainty (LCU) was assessed using plausible alternative land cover classes that were identified during the land cover classification procedure. An alternative land cover class was deemed to be available for a 300m pixel when the likelihood of it being correct was above 85%, according to the maximum likelihood classifier (CCI\_LC ATBD, 2013). The alternative class was chosen for the resulting minimum (maximum) biomass land cover map if it occurs below (above) the first choice class in the biomass hierarchy shown in table 1. If the alternative class was lower down (higher up) the hierarchy of biomass than the first choice class, then it was selected for the minimum (maximum) biomass map. Where no alternative class was available, or the biomass hierarchy criteria were not met, the land cover class remained unchanged from the original map.

The assignment of each land cover class to a class within a generalised biomass hierarchy is shown in table 1. No effort has been made to quantify specifically the biomass associated with each class – biomass classes are assigned purely with the aim of describing subjectively where a land cover class

	Ref	LC CCI Climate Assessment Report v1		
	Issue	Page	Date	
	1.0	95	13.07.2015	

fits within the vegetation succession from tree to shrub to grass cover. The biomass hierarchy is intended to be used to prioritise one land cover class over another, to help in the decision of whether to replace the 1st choice class with a 2nd choice class. For example, if a grid cell has first choice class 40 (grass), and the second choice class 12 (shrub) exceeds the minimum probability threshold, then, if we are making a 'maximum biomass' map, we would use class 12 in the 'max biomass' uncertainty map. If we are making a 'minimum biomass' map, then we don't change the class.

The 2 resulting land cover maps were converted to PFT fractions using the LC\_CCI user tool (version 3.7), and the resulting fractions were aggregated further to meet the needs of the JSBACH, JULES and ORCHIDEE land surface models. It is proposed that the final PFT fraction maps for minimum and maximum biomass represent the largest possible range of quantifiable land cover class uncertainty in the context of land surface models.

## **2.2. Cross-walking Uncertainty**

Uncertainty also arises from the translation of land cover classes to the PFTs used in land surface models. In this case, assumptions are made on the fraction of each PFT that occurs within a given land cover class. These assumptions are based on the fractional cover of major vegetation types derived from the Land Cover Classification System (LCCS; Di Gregorio & Jansen, 2000) that is the basis of the LC\_CCI legend (Poulter et al., 2015). The LCCS description defines a range of fractions of vegetation cover for each LC\_CCI class. This information is then used to guide expert judgement on the exact fractions of PFTs that occur in each land cover class, resulting in a cross-walking matrix that translates land cover classes into plant functional types.

In cross-walking procedure, uncertainty arises in the translation of a land cover class to the fractional cover of the PFTs used by LSMs. Uncertainty in the fraction of each PFT found within a given land cover class may arise from a number of factors, namely:

- Regional variations in the density of cover
- Variations in agreement between experts
- Coarse spatial resolution of satellite retrievals
- Lack of very high resolution calibration datasets

Each of the above factors may affect the values found in the reference LC\_CCI cross-walking table (Poulter et al., 2015). However, it is currently not known how sensitive LSMs are to plausible perturbations in this table.

	Ref	LC CCI Climate Assessment Report v1		
	Issue	Page	Date	
	1.0	96	13.07.2015	

In this experiment, cross-walking uncertainty was quantified in the context of either minimum or maximum biomass. Where possible, the Land Cover Classification Scheme (LCCS) class description was used to create a ‘minimum biomass’ and a ‘maximum biomass’ cross-walking matrix. For example, class 61 (Broadleaf deciduous tree cover, closed (>40%)) is converted to 70% broadleaf deciduous tree PFT in the reference dataset. In the ‘minimum biomass’ cross-walking, this value reduces to 40%, the minimum fractional cover permitted by the LCCS description. In the ‘maximum biomass’ cross-walking, 100% of the grid cell is converted to broadleaf deciduous tree PFT.

### **2.3. LSM Modelling Protocol**

In this study we compare the output of three land-surface models (LSMs). Our mini ensemble contains the following models: JSBACH, JULES and ORCHIDEE. In principle, a LSM provides the lower atmospheric boundary condition over land in the Earth system modelling framework. Thus, it represents the parametrizations of land surface-atmosphere exchange processes. It controls the partitioning of available energy at the surface between sensible and latent heat, and it controls the distribution of available water between evaporation and runoff (Pitman, 2003). Soil layer processes also control distributions of carbon and other trace gases in terrestrial reservoirs. Recently, Friend et al. (2013) compared seven global LSMs and showed that Carbon residence time dominates uncertainty in terrestrial vegetation responses to future climate and atmospheric CO<sub>2</sub>. Hence, it complements the importance of land-surface schemes within the Earth system modelling framework for understanding the range of uncertainty in reproducing the present-day climate simulations as well as anticipating the potential responses of the land-surface to future changes in climate and atmospheric chemistry.

Though, land-surface schemes have been developed to be coupled with the atmospheric component of the Earth-system Model (ESM) they can also be driven by climate forcing data. In this study, our focus is the uncertainty in the land cover maps derived from satellite observations and its impact on present day climate. Therefore, WFDEI (WATCH Forcing Data methodology applied to ERA-Interim data) meteorological forcing data developed by Weedon et al (2014, 2010) have been used to drive land surface schemes. It can be noted, that bias correction of precipitation, downward shortwave flux correction and extension over ERA-Interim period (1979-2010) make the WFDEI data a valuable contribution to the comparison of LSM output. Following this approach rather than using a coupled Earth system model, we avoid uncertainty coming from other model components (atmosphere, ocean). It is also easier to set up a standardized experimental protocol, identify problems and interpret results of the model inter comparison.

	Ref	LC CCI Climate Assessment Report v1		
	Issue	Page	Date	
	1.0	97	13.07.2015	

WFDEI data are available at 0.5 degree spatial resolution and with 3 hours temporal resolution. However, previous studies with JULES and ORCHIDEE (e.g. Compton and Best, 2011) and ad hoc comparison of JSBACH output at T63 (~1.875°) and 2° have shown that spatial resolution does not have substantial impact on the results, therefore, experiments are conducted at 2 degree resolution. A conservative remapping method (Jones, 1999) was used to aggregate the forcing fields (precipitation, temperature, wind, downwards shortwave and longwave radiation fluxes and pressure) at 2 degrees. Special care is taken for the treatment of specific humidity. Like Weedon et al (2010, 2014) we followed the methods of Cosgrove et al (2003) in order to conserve moisture in the air and avoid supersaturation. Relative humidity is calculated at the 0.5 degrees, and then aggregated at 2 degrees. Specific humidity at 2 degrees is then calculated from relative humidity. Both JULES and ORCHIDEE use the data in their original temporal resolution (3h), while JSBACH makes use of the data subsampled or accumulated to daily intervals.

LSMs are sensitive to the choice of initialization method. The fidelity of LSM simulations is limited by the accuracy of the meteorological forcing and initial conditions, which may not be in equilibrium (Rodell et al, 2005). For the present study, carbon pools and other LSM states need to be in equilibrium before the actual experiments are started. Thus, first a spin-up of the carbon pool is conducted using WFDEI forced LSM data for the years 1979-1983. Then, the LSMs are run repeatedly through a 1979-1983 spin-up period until the net ecosystem exchange equilibrium between forcing and initial state variables with 1979 CO<sub>2</sub> concentration is reached. With this approach we ensure that the state variables (such as soil layers moisture and heat content, carbon pools distribution) are in equilibrium with transient CO<sub>2</sub> concentrations. Simulations are performed for the period 1979-2010 and transient CO<sub>2</sub> concentrations are taken from CMIP5 forcing for the historical simulations.

### **3. Results**

#### **3.1. PFT distributions**

#### **3.2. Impacts on carbon stocks and fluxes**

#### **3.3. Impacts on energy and water balance**

### **4. Discussion and conclusions**

This information has important implications for the regions and classes on which future land cover mapping efforts are focussed. We have shown that there is still considerable uncertainty in the methods used to convert land cover to the plant functional types used by land surface models. Furthermore, uncertainty in the labelling of land cover classes has been shown to be of an equal magnitude to cross-walking uncertainty.

	Ref	LC CCI Climate Assessment Report v1		
	Issue	Page	Date	
	1.0	98	13.07.2015	

- Maximising (minimising) biomass in land cover uncertainty and cross-walking uncertainty leads to the largest (smallest) tree cover fractions and the smallest (largest) bare soil fractions in all regions.
- Uncertainty in bare soil fraction in northern latitudes (north of 60N) is all related to choice of land cover class, not cross-walking uncertainty. Further south however, grass cover uncertainty is all related to cross-walking uncertainty rather than land cover uncertainty
- In the tropics (15S to 15N), tree cover uncertainty is equally related to land cover and cross walking uncertainty, whereas in the other major forest belt (45N to 65N), uncertainty is more related to cross-walking uncertainty. This is also seen in northern Asia (NAS) and eastern North America (ENA) Giorgi regions.
- Uncertainty in grass and shrub fractions is more locally dependent. It appears this is due to regional differences in land cover uncertainty in grass classes, and cross-walking uncertainty affecting different classes in different ways. For example, in tropical regions, maximising biomass in the cross-walking approach leads to a reduction in grass cover relative to the reference, whereas in temperate regions (30N to 50N and 25S to 35S), maximising biomass leads to an increase in grass cover.

## Appendix A

### Acknowledgements

### References

### Tables

Table 5-1. Each land cover class within the Land Cover CCI legend is assigned a class within a biomass hierarchy for use in assessing classification uncertainty. The highest biomass is tree, followed by shrub, grass, moss and lichen and then bare.

LC class	Description	Biomass hierarchy
0	No data	n/a
10	Cropland, rainfed	Grass
11	Cropland, Herbaceous cover	Grass
12	Cropland, Tree or shrub cover	Shrub
20	Cropland, irrigated or post-flooding	Grass
30	Mosaic cropland (>50%) / natural vegetation (tree, shrub, herbaceous cover) (<50%)	Grass
40	Mosaic natural vegetation (tree, shrub, herbaceous cover) (>50%) / cropland	Grass

	Ref	LC CCI Climate Assessment Report v1		
	Issue	Page	Date	
	1.0	99	13.07.2015	

LC class	Description	Biomass hierarchy
	(<50%)	
50	Tree cover, broadleaved, evergreen, closed to open (>15%)	Tree
60	Tree cover, broadleaved, deciduous, closed to open (>15%)	Tree
61	Tree cover, broadleaved, deciduous, closed (>40%)	Tree
62	Tree cover, broadleaved, deciduous, open (15-40%)	Shrub
70	Tree cover, needleleaved, evergreen, closed to open (>15%)	Tree
71	Tree cover, needleleaved, evergreen, closed (>40%)	Tree
72	Tree cover, needleleaved, evergreen, open (15-40%)	Shrub
80	Tree cover, needleleaved, deciduous, closed to open (>15%)	Tree
81	Tree cover, needleleaved, deciduous, closed (>40%)	Tree
82	Tree cover, needleleaved, deciduous, open (15-40%)	Shrub
90	Tree cover, mixed leaf type (broadleaved and needleleaved)	Tree
100	Mosaic tree and shrub (>50%) / herbaceous cover (<50%)	Tree
110	Mosaic herbaceous cover (>50%) / tree and shrub (<50%)	Grass
120	Shrubland	Shrub
121	Shrubland evergreen	Shrub
122	Shrubland deciduous	Shrub
130	Grassland	Grass
140	Lichens and mosses	Moss/Lichens
150	Sparse vegetation (tree, shrub, herbaceous cover) (<15%)	Bare
151	Sparse tree (<15%)	Bare
152	Sparse shrub (<15%)	Bare
153	Sparse herbaceous cover (<15%)	Bare
160	Tree cover, flooded, fresh or brakish water	Tree
170	Tree cover, flooded, saline water	Tree
180	Shrub or herbaceous cover, flooded, fresh/saline/brakish water	Grass
190	Urban areas	Bare
200	Bare areas	Bare
201	Consolidated bare areas	Bare
202	Unconsolidated bare areas	Bare
210	Water bodies	n/a
220	Permanent snow and ice	n/a

Table 5-2. Perturbations of the cross walking table from Poulter et al (2015)

ID	Description	BLE Tree			BLD Tree			NLE Tree			NLD Tree			BLE Shrub			BLD Shrub			NLE Shrub			NLD Shrub			Natural Grass			Managed Grass			Bare Soil			Water	Snow / Ice
		Min Bm	Ref	Max Bm	Min Bm	Ref	Max Bm	Min Bm	Ref	Max Bm	Min Bm	Ref	Max Bm	Min Bm	Ref	Max Bm	Min Bm	Ref	Max Bm	Min Bm	Ref	Max Bm	Ref	Ref												
0	No data	0	0	0	0	0	0	0	0	0	0	0	0	0	0	0	0	0	0	0	0	0	0	0	0	0	0	0	0	0	0	0	0	0		
10	Cropland, rainfed	0	0	0	0	0	0	0	0	0	0	0	0	0	0	0	0	0	0	0	0	0	0	0	0	0	0	60	100	100	40	0	0	0	0	
11	Herbaceous cover	0	0	0	0	0	0	0	0	0	0	0	0	0	0	0	0	0	0	0	0	0	0	0	0	0	60	100	100	40	0	0	0	0		
12	Tree or shrub cover	0	0	0	0	0	0	0	0	0	0	0	0	0	0	30	50	50	0	0	0	0	0	0	0	0	30	50	50	40	0	0	0	0		
20	Cropland, irrigated or post-flooding	0	0	0	0	0	0	0	0	0	0	0	0	0	0	0	0	0	0	0	0	0	0	0	0	0	100	100	100	0	0	0	0	0		
30	Mosaic cropland (>50%) / natural vegetation (tree, shrub, herbaceous cover) (<50%)	0	5	10	0	5	10	0	0	0	0	0	0	3.3	5	5	3.3	5	5	3.4	5	5	0	0	0	15	15	15	75	60	50	0	0	0	0	
40	Mosaic natural vegetation (tree, shrub, herbaceous cover) (>50%) / cropland (<50%)	0	5	15	0	5	15	0	0	0	0	0	0	7.5	7.5	7.5	10	10	10	7.5	7.5	7.5	0	0	0	25	25	25	50	40	20	0	0	0	0	
50	Tree cover, broadleaved, evergreen, closed to open (>15%)	70	90	100	0	0	0	0	0	0	0	0	0	7.5	5	0	7.5	5	0	0	0	0	0	0	0	15	0	0	0	0	0	0	0	0		

ID	Description	BLE Tree			BLD Tree			NLE Tree			NLD Tree			BLE Shrub			BLD Shrub			NLE Shrub			NLD Shrub			Natural Grass			Managed Grass			Bare Soil			Water Ref	Snow / Ice Ref
		Min Bm	Ref	Max Bm	Min Bm	Ref	Max Bm	Min Bm	Ref	Max Bm	Min Bm	Ref	Max Bm	Min Bm	Ref	Max Bm	Min Bm	Ref	Max Bm	Min Bm	Ref	Max Bm														
60	Tree cover, broadleaved, deciduous, closed to open (>15%)	0	0	0	40	70	100	0	0	0	0	0	0	0	0	0	15	15	0	0	0	0	0	0	0	45	15	0	0	0	0	0	0	0	0	0
61	Tree cover, broadleaved, deciduous, closed (>40%)	0	0	0	40	70	100	0	0	0	0	0	0	0	0	0	15	15	0	0	0	0	0	0	0	45	15	0	0	0	0	0	0	0	0	0
62	Tree cover, broadleaved, deciduous, open (15-40%)	0	0	0	15	30	40	0	0	0	0	0	0	0	0	0	25	25	25	0	0	0	0	0	0	50	35	35	0	0	0	10	10	0	0	0
70	Tree cover, needleleaved, evergreen, closed to open (>15%)	0	0	0	0	0	0	40	70	100	0	0	0	5	5	0	5	5	0	5	5	0	0	0	0	45	15	0	0	0	0	0	0	0	0	0
71	Tree cover, needleleaved, evergreen, closed (>40%)	0	0	0	0	0	0	40	70	100	0	0	0	5	5	0	5	5	0	5	5	0	0	0	0	45	15	0	0	0	0	0	0	0	0	0
72	Tree cover, needleleaved, evergreen, open (15-40%)	0	0	0	0	0	0	15	30	40	0	0	0	0	0	0	5	5	5	5	5	5	0	0	0	45	30	30	0	0	0	30	30	20	0	0

ID	Description	BLE Tree			BLD Tree			NLE Tree			NLD Tree			BLE Shrub			BLD Shrub			NLE Shrub			NLD Shrub			Natural Grass			Managed Grass			Bare Soil			Water	Snow / Ice	
		Min Bm	Ref	Max Bm	Min Bm	Ref	Max Bm	Min Bm	Ref	Max Bm	Min Bm	Ref	Max Bm	Min Bm	Ref	Max Bm	Min Bm	Ref	Max Bm	Min Bm	Ref	Max Bm	Min Bm	Ref	Max Bm												
80	Tree cover, needleleaved, deciduous, closed to open (>15%)	0	0	0	0	0	0	0	0	0	40	70	100	5	5	0	5	5	0	5	5	0	0	0	0	45	15	0	0	0	0	0	0	0	0	0	0
81	Tree cover, needleleaved, deciduous, closed (>40%)	0	0	0	0	0	0	0	0	0	40	70	100	5	5	0	5	5	0	5	5	0	0	0	0	45	15	0	0	0	0	0	0	0	0	0	0
82	Tree cover, needleleaved, deciduous, open (15-40%)	0	0	0	0	0	0	0	0	0	15	30	40	0	0	0	5	5	5	5	5	5	0	0	0	45	30	30	0	0	0	30	30	20	0	0	0
90	Tree cover, mixed leaf type (broadleaved and needleleaved)	0	0	0	20	30	50	13.3	20	33.3	6.7	10	16.7	5	5	0	5	5	0	5	5	0	0	0	0	35	15	0	0	0	0	10	10	0	0	0	0
100	Mosaic tree and shrub (>50%) / herbaceous cover (<50%)	7.5	10	15	15	20	30	3.8	5	7.5	3.7	5	7.5	5	5	5	10	10	10	5	5	5	0	0	0	50	40	20	0	0	0	0	0	0	0	0	0
110	Mosaic herbaceous cover (>50%) / tree and shrub (<50%)	1.3	5	7.5	2.4	10	15	1.3	5	7.5	0	0	0	5	5	5	10	10	10	5	5	5	0	0	0	75	60	50	0	0	0	0	0	0	0	0	0
12	Shrubland	0	0	0	0	0	0	0	0	0	0	0	0	13.3	20	26.7	13.3	20	26.7	13.4	20	26.6	0	0	0	30	20	20	0	0	0	30	20	0	0	0	0

ID	Description	BLE Tree			BLD Tree			NLE Tree			NLD Tree			BLE Shrub			BLD Shrub			NLE Shrub			NLD Shrub			Natural Grass			Managed Grass			Bare Soil			Water	Snow / Ice
		Min Bm	Ref	Max Bm	Min Bm	Ref	Max Bm	Min Bm	Ref	Max Bm	Min Bm	Ref	Max Bm	Min Bm	Ref	Max Bm	Min Bm	Ref	Max Bm	Min Bm	Ref	Max Bm	Ref	Ref												
0																																				
121	Shrubland evergreen	0	0	0	0	0	0	0	0	0	0	0	20	30	40	0	0	0	20	30	40	0	0	0	30	20	20	0	0	0	30	20	0	0	0	
122	Shrubland deciduous	0	0	0	0	0	0	0	0	0	0	0	0	0	0	40	60	80	0	0	0	0	0	0	30	20	20	0	0	0	30	20	0	0	0	
130	Grassland	0	0	0	0	0	0	0	0	0	0	0	0	0	0	0	0	0	0	0	0	0	0	0	51	60	95	0	0	0	49	40	5	0	0	
140	Lichens and mosses	0	0	0	0	0	0	0	0	0	0	0	0	0	0	0	0	0	0	0	0	0	0	0	60	60	60	0	0	0	40	40	40	0	0	
150	Sparse vegetation (tree, shrub, herbaceous cover) (<15%)	0	1	1	0	3	3	0	1	1	0	0	0	1	1	1	3	3	3	1	1	1	0	0	0	5	5	5	0	0	0	90	85	85	0	0
151	Sparse tree (<15%)	1	2	3	3	6	9	1	2	3	0	0	0	0	0	0	0	0	0	0	0	0	0	0	5	5	0	0	0	0	90	85	85	0	0	
152	Sparse shrub (<15%)	0	0	0	0	0	0	0	0	0	0	0	1	2	3	3	6	9	1	2	3	0	0	0	5	5	0	0	0	0	90	85	85	0	0	
153	Sparse herbaceous cover (<15%)	0	0	0	0	0	0	0	0	0	0	0	0	0	0	0	0	0	0	0	0	0	0	10	15	15	0	0	0	90	85	85	0	0		
160	Tree cover, flooded, fresh or brakish water	20	30	37.5	20	30	37.5	0	0	0	0	0	0	0	0	0	0	0	0	0	0	0	0	0	0	0	0	0	0	0	0	0	0	20	0	

ID	Description	BLE Tree			BLD Tree			NLE Tree			NLD Tree			BLE Shrub			BLD Shrub			NLE Shrub			NLD Shrub			Natural Grass			Managed Grass			Bare Soil			Water		Snow / Ice	
		Min Bm	Ref	Max Bm	Min Bm	Ref	Max Bm	Min Bm	Ref	Max Bm	Min Bm	Ref	Max Bm	Min Bm	Ref	Max Bm	Min Bm	Ref	Max Bm	Min Bm	Ref	Max Bm	Ref	Ref	Ref													
170	Tree cover, flooded, saline water	40	60	75	0	0	0	0	0	0	0	0	30	20	12.5	0	0	0	0	0	0	0	0	0	0	0	0	0	0	0	0	0	20	0				
180	Shrub or herbaceous cover, flooded, fresh/saline/brackish water	0	0	0	0	5	5	0	10	10	0	0	0	0	0	12.7	10	10	6.4	5	5	0	0	0	50.9	40	40	0	0	0	0	0	0	30	0			
190	Urban areas	0	0	0	2.5	2.5	2.5	2.5	2.5	2.5	0	0	0	0	0	0	0	0	0	0	0	0	0	0	15	15	15	0	0	0	75	75	75	5	0			
200	Bare areas	0	0	0	0	0	0	0	0	0	0	0	0	0	0	0	0	0	0	0	0	0	0	0	0	0	0	0	0	0	100	100	100	0	0			
201	Consolidated bare area	0	0	0	0	0	0	0	0	0	0	0	0	0	0	0	0	0	0	0	0	0	0	0	0	0	0	0	0	0	100	100	100	0	0			
202	Unconsolidated bare areas	0	0	0	0	0	0	0	0	0	0	0	0	0	0	0	0	0	0	0	0	0	0	0	0	0	0	0	0	0	100	100	100	0	0			
210	Water bodies	0	0	0	0	0	0	0	0	0	0	0	0	0	0	0	0	0	0	0	0	0	0	0	0	0	0	0	0	0	0	0	0	100	0			
220	Permanent snow and ice	0	0	0	0	0	0	0	0	0	0	0	0	0	0	0	0	0	0	0	0	0	0	0	0	0	0	0	0	0	0	0	0	100	0			

Table 5-3. Aggregation of PFTs for analysis

PFT	Aggregated cover type
Broadleaf Evergreen Tree	Tree
Broadleaf Deciduous Tree	
Needleleaf Evergreen Tree	
Needleleaf Deciduous Tree	
Broadleaf Evergreen Shrub	Shrub
Broadleaf Deciduous Shrub	
Needleleaf Evergreen Shrub	
Needleleaf Deciduous Shrub	
Natural Grass	Grass
Managed Grass	
Bare Soil	Bare
Water	Not perturbed
Snow and Ice	Not perturbed

## Figures

Figure 1. Maps showing the *difference* (compared to the reference case) in fraction of vegetation for the Trees (1st row), Shrubs (2<sup>nd</sup> row), Natural and Managed Grasses (3rd row) and Bare soil (4th row) for each of the uncertainty simulations. The actual vegetation fraction for reference case is shown in the middle column (refLC ref CW). The difference in vegetation fraction for the minimum biomass vegetation distributions are shown to the left of the reference case, first with minimum LC maps and the reference cross-walking table (minLC refCW – 2<sup>nd</sup> column) and with both the minimum biomass LC maps and minimum cross-walking table (min LC min CW – 1<sup>st</sup> column). To the right of the reference map are the equivalent differences in vegetation fraction for the maximum biomass vegetation distributions (maxLC ref CW – 4<sup>th</sup> column, maxLC maxCW – 5<sup>th</sup> column).

